

Heat and Mass Transfer in Adsorption Columns

by

Chinmay Ravindra Baliga

A thesis submitted in partial fulfillment of the requirements for the degree of

Master of Science

in

Chemical Engineering

Department of Chemical and Materials Engineering

University of Alberta

© Chinmay Ravindra Baliga, 2023

Abstract

Fixed beds are widely used in the chemical and process industry due to their simple yet effective performance. They find applications in heterogeneous catalysis (e.g., dry reforming of methane, methanol synthesis, etc.) and in adsorption (hydrogen from steam methane reforming, post-combustion CO_2 capture, oxygen concentration, helium purification).

Determining heat transfer at the wall in a fixed bed is crucial to predict the performance of the column or reactor. Literature review concludes that most adsorption modeling studies followed a simplified one-dimensional (1D) approach. Multidimensional simulations could potentially unlock additional insights into temperature and flow profiles. Chapter 1 introduces the fundamentals of adsorption principles and provides a framework of the transport equations involved in the adsorption process. Developments in computational modeling and a 1D process modeling study of an adsorption cycle for CO_2 capture are briefly discussed.

The fluid-wall heat transfer coefficient is currently obtained experimentally and is fitted via optimization to match the thermal breakthrough profiles of the system. This limits the range of applicability. Chapter 2 investigates the fluid-wall heat transfer in fixed beds, primarily from the aspect of wall Nusselt number determination via particle-resolved computational fluid dynamics (PRCFD) simulations and comparing vis-à-vis various correlations in literature. A fixed bed comprising 374 particles is generated using gravity sedimentation-assisted discrete element modeling (DEM). Steady-state, three-dimensional coupled flow and heat CFD simulations are conducted to investigate fluid-wall heat transfer. Additionally, the effect of buoyancy-driven flows on the wall heat transfer number is studied.

The main objective of Chapter 3 is to validate boundary conditions for a hot object cooled down in a cold environment due to natural convection. The cooling of hot water in a cup is modeled via 2D and 3D CFD and conduct lab-scale experiments for validation purposes. User-Defined Functions, or UDFs, are developed and compiled within Fluent to expand the solver’s capabilities. Thus, a UDF module capable of simulating the combined effects of natural convection, radiation, and evaporative cooling has been developed. To date, CFD solvers do not yet possess natively the option to apply the natural convection or evaporative boundary conditions. This validated UDF may be ported for fixed beds and adsorption columns for improved prediction of thermal profiles in both lab-scale and industrial units.

Chapter 4 deals with 2D transient CFD-based adsorption Dynamic Column Breakthrough simulations. The convective and radiative heat transfer coefficients are determined via physics-based modeling, eliminating the need to fit these coefficients to a particular system. The development of temperature profiles along the bed is analyzed. Our CFD model is validated against published experimental results for a small-scale pilot unit). The success of these simulations would form the framework for column-ambient heat transfer modeling in cyclic pressure vacuum swing adsorption (PVSA) CFD simulations.

Chapter 5 summarizes the CFD angle to adsorption in fixed beds, laying down conclusions and future work. Through the undertaken “serial by simplification” multi-scale modeling approach, correlations developed on multidimensional (2D & 3D) representative geometries may be employed in 1D adsorber models. The novelty of our work is implementing adsorption equilibria data for various adsorbents rigorously obtained by experiments in conjunction with CFD modeling in an attempt to identify and optimize the most critical design and operating factors, such as column geometry/flow distribution asymmetries/ scale-up, etc.

Keywords: Adsorption, Computational fluid dynamics, Conjugate heat transfer modeling, Large eddy simulations, Natural convection, Particle-resolved CFD, Porous media, Pressure swing adsorption, Thermal boundary conditions, User-defined functions

Preface

The content presented in Chapter 2 is reproduced from my research article accepted to the Canadian Journal of Chemical Engineering published by Wiley. The article, titled "Convective heat transfer coefficient for the side-wall in a fixed bed", may be accessed here: C. Baliga, P. Nikrityuk, Can. J. Chem. Eng. **2023**. I composed the initial draft, sequentially polished and refined under the valuable guidance of Prof. Petr Nikrityuk.

The content in Chapter 3 is based on an original manuscript currently submitted to the International Communications in Heat and Mass Transfer journal published by Elsevier. The UDF source code development, experimental procedure, data curation, and analysis were conducted by me. My research group colleague and co-author in this work, Doston Shayunusov, provided support with the post-processing of CFD results. Prof. Arvind Rajendran and Dr. James A. Sawada from the Lab of Advanced Separation Processes at the University of Alberta provided the experimental setup and data acquisition system for model validation.

Prof. Petr Nikrityuk, as the supervising author, made significant contributions to the conceptualization of the research topic, provided valuable supervision and steering throughout its development, and contributed to the review and editing of both manuscripts.

Some sections of literature review (my original work) in Chapter 1 were adapted for inclusion in my co-authored paper titled "CFD-based model of adsorption columns: validation" currently under review with Chemical Engineering Science published by Elsevier.

The content in Chapter 4 is partially based on and an extension of the work by my colleague Henry Fabian Ramos, author of the above paper submitted to the CES journal. The supplementary UDF source code implementation, data analysis, and post-processing were conducted by me. The findings within this chapter are intended to be published in the future.

All equations and materials used in this work are appropriately referenced in the text.

*To my mom
whose boundless love and unwavering support made this journey possible.*

Acknowledgements

First and foremost, I extend my heartfelt appreciation to my esteemed thesis advisor and supervisor, Prof. Petr Nikrityuk. Your guidance, expertise, and patience were instrumental in shaping this research. Your continuous encouragement, insightful feedback, and willingness to engage in discussions were invaluable. I am genuinely grateful for the knowledge and skills I have gained under your mentorship. Thank you for believing in me and reassuring me with academic writing, Prof. Nik.

I am sincerely grateful to Prof. Arvind Rajendran, my co-supervisor, for introducing me to and engaging me in the domain of adsorption. Thank you for including me at your group meetings and providing me with the opportunity to be apprised of the developments in experimental adsorption research. Special thanks to Dr. Jim Sawada for the help with the experimental setup for my research. Thank you, Jim, for your witty anecdotes and the Speechcraft program.

I acknowledge the financial support from *Benchmark International*, Edmonton, Alberta, along with the *Natural Science and Engineering Research Council of Canada* (NSERC) under Alliance Grant, and from *Alberta Innovates* through the Campus Alberta Small Business Engagement (CASBE) grant. I greatly appreciate the *Digital Research Alliance of Canada* for providing computational resources.

I acknowledge the contributions of the faculty and staff in the Chemical and Materials Engineering Department at the University of Alberta, who provided me with an enriching academic environment and prompt administrative support.

I am eternally indebted to the rigorous technical program at IIT Bombay, my alma mater. I fondly recall the constructive discussions with Prof. Jhumpa Adhikari, Prof. Ravindra Gudi, and Prof. Sanjay Mahajani during my undergraduate years. Thank you for inspiring

me and instilling a sense of purpose in pursuing a career in chemical engineering.

I immensely thank my dear friends, Andrés, Devavrat, Doston, Henry, and Ravi. Andrés, Doston, and Henry, you were amazing research group members, and our fruitful deliberations significantly advanced our technical expertise. Devavrat, thanks for always being up for a challenge, event, sport, or hike. Ravi, thank you for facilitating a seamless transition to Edmonton and for engaging in valuable discussions on some demanding coursework. Thank you all for standing by me during the highs and lows of this thesis. Thank you for being my sounding board and celebrating the milestones together. Shout out to my wallyball buddies Jash, Kevin, Shahdab, Shanmuk, Tanay, and Yash for fostering the cathartic outlet of sport.

Finally, I sincerely thank my mom and brother, Abhijeet, for their unwavering support and encouragement. Abhijeet, thanks for pushing me out of my comfort zone. Your belief in me has been a constant source of motivation. Your presence in my life made the challenging moments bearable and the joyous moments more delightful.

Sincerely,

Chinmay Baliga

Edmonton 2023

Table of Contents

Abstract	ii
Preface	iv
Acknowledgements	vi
List of Tables	x
List of Figures	xii
List of Symbols	xvi
1 Introduction to Adsorption	1
1.1 Benchmarking and Key Performance Indicators of an adsorption process . . .	4
1.2 Adsorption process modeling	5
1.2.1 Adsorption equilibrium	6
1.2.2 Adsorption mass transfer kinetics	8
1.2.3 Material balance	10
1.2.4 Energy balance	11
1.2.5 Momentum balance	12
1.3 Developments in numerical methods and computational modeling of fixed bed columns for adsorption	13
1.3.1 A case study in carbon dioxide adsorption modeling	15
1.4 CFD modeling of heat transfer and adsorption processes in fixed beds	19
1.5 Objectives and Project Scope	27

2	Convective heat transfer coefficient for the side-wall in a fixed bed	29
2.1	Introduction	30
2.2	Problem description	35
2.3	Computational model	37
2.3.1	Boundary conditions	40
2.4	Results and discussion	42
2.5	Conclusion	56
3	Implementation and validation of boundary conditions between a chemical reactor and ambient air	57
3.1	Introduction	58
3.2	Problem and Model Formulation	60
3.2.1	Boundary conditions	64
3.2.2	Experiment	67
3.3	Numerics	68
3.4	Results	74
3.5	Conclusion	82
3.6	Addendum: LES modeling	84
4	Implementation and validation of boundary conditions between adsorption columns and ambient air	90
4.1	Introduction	90
4.2	Thermal – Electric Analogy	93
4.3	Natural Convection in Adsorption Columns — Heat transfer formulation	94
4.4	Results of 2D DCB simulations	97
5	Conclusion	111
5.1	Summary	111
5.2	Outlook	115
	Bibliography	117

List of Tables

1.1	Boundary conditions for the steps in PSA cycle	17
1.2	Flow transition regimes in packed beds ^[77]	26
2.1	Wall Nusselt number, Nu_w , versus particle Reynolds number, Re_p , correlations available across literature.	32
2.2	Packed bed characteristics.	36
2.3	3D CFD system material properties.	37
2.4	List of models and schemes ^[127] used in the CFD model.	38
2.5	Reynolds numbers and corresponding flow models used in simulations.	38
2.6	Turbulent viscosity ratio (TVR) versus Re_p	38
2.7	Steady-state laminar flow model for the fixed bed. ^[129]	39
2.8	Steady-state RANS model: the shear-stress transport (SST) $k-\omega$ model. ^[128,130]	39
2.9	Characteristics and control volume count for the three meshes with hollow particles.	40
2.10	Characteristics and control volume count for the two meshes with solid CVs meshed.	40
2.11	Feed temperature heat transfer sensitivity for buoyancy-driven flows.	55
3.1	Transient laminar flow model PDEs for water in the coffee cup	62
3.2	Paper cup characteristics	68
3.3	List of models and schemes ^[151] used in the 2D axisymmetric Laminar CFD model	69

3.4	Description of all user-defined functions (UDFs) in the hot cavity–cold ambient CFD model	73
3.5	List of models and schemes ^[151] used in the 3D LES CFD model	86
4.1	Thermal-Electric Analogy	93
4.2	Laboratory rig column characteristics	99
4.3	Parameters used for CFD-based adsorption framework developed by Fabian et al. ^[155]	99
4.4	Free stream (ambient air) properties used in the natural convection driven heat transfer UDF	100

List of Figures

1.1	Schematic of a typical 4-step PSA cycle	3
1.2	Overview of the elements of modeling the physical phenomena involved in an adsorption process	6
1.3	Typical constituent steps in a cyclic adsorption process	18
1.4	Radial porosity profile of a densely packed fixed bed ^[59]	20
1.5	Focus of the thesis	27
2.1	Schematic and CFD geometry: (A) Simplified schematic of the fixed bed simulation; (B) Slice of a fixed bed packed with monodisperse particles containing hollow solid mesh elements; and (C) Slice of a fixed bed packed with monodisperse particles containing internal solid mesh elements.	36
2.2	Grid studies demonstrating mesh independence: (A) Grid study comparing Nu_w from various BCs (Dirichlet, Neumann, and Robin) applied on hollow particle meshes; (B) Grid study comparing Nu_w between the hollow and meshed particle meshes for the case of insulated particles, and between two qualities of the meshed particle meshes for $k_s/k_f = 1$	44
2.3	Correlations for Nu_w versus Re_p available across literature	45
2.4	Particle surface temperature (T, K) contours subject to Neumann BC	47
2.5	Particle surface temperature (T, K) contours subject to Robin BC	48
2.6	Model fitting and comparison with correlations for Nu_w versus Re_p available across literature	49
2.7	Particle surface temperature (T, K) contours for various k_s/k_f ratios: (A) $k_s/k_f \rightarrow 0$; (B) $k_s/k_f = 0.1$; (C) $k_s/k_f = 1$; (C) $k_s/k_f = 10$; (E) $k_s/k_f = 100$	50

2.8	Non-dimensional centreline temperature along non-dimensional bed length for various k_s/k_f ratios: (A) $k_s/k_f \rightarrow 0$; (B) $k_s/k_f = 0.1$; (C) $k_s/k_f = 1$; (D) $k_s/k_f = 10$; (E) $k_s/k_f = 100$	52
2.9	Non-dimensional centreline temperature along non-dimensional bed length for various Re_p : (A) $Re_p = 10$; (B) $Re_p = 50$; (C) $Re_p = 150$; (D) $Re_p = 500$	53
2.10	$\langle T_{gas} \rangle - \langle T_{solid} \rangle$ for various k_s/k_f ratios	54
2.11	2D slice depicting non-dimensional gas temperature (T^* , [-]) contours and velocity streamlines compared (a) without and (b), (c) with buoyancy-driven flow consideration at $Re_p = 1$ for two feed temperatures and two k_s/k_f ratios. Here, 1) $k_s/k_f = 1$; 2) $k_s/k_f = 100$, (b) $T_{feed} - T_w = 50K$; (c) $T_{feed} - T_w = 300K$	55
3.1	Schematic representation of computational domains for two ways of modeling: (a) conjugate domain (b) short domain	59
3.2	Coffee cup setup. (a) Schematic indicating the computational domain, heat transfer mechanisms, and the locations of the thermoelements T_i (b) Experimental setup indicating the thermoelements (c) Non-uniform, structured grid of the 104 000 cell mesh	61
3.3	Thermophysical properties of water. (a) Density, ρ (b) Specific heat capacity, C_p (c) Thermal conductivity, k (d) Viscosity, μ	63
3.4	Set of grid studies. (a) Volume-averaged temperature vs. time (b) Middle ring line-averaged temperature vis-à-vis middle thermoelement, T_2 , vs. time	70
3.5	Temperature dependence of heat fluxes at the (a) side wall and (b) top surface	72
3.6	Time histories of the temperature and volume-averaged velocity. (a) T_1 , T_2 , and T_3 temperature profiles and validation with experiment (b) Volume-averaged velocity, $\langle \vec{U} \rangle$, profile	75
3.7	Time history of the integral quantities, $\langle T \rangle_{top}$, $\langle T \rangle_{side}$, $\langle T \rangle_{bulk}$ for chosen mesh (104k cells). (a) Considering evaporation (b) Neglecting evaporation	77
3.8	Temperature contours at different times	79
3.9	Velocity magnitude and vector contours at different times	81
3.10	3D mesh with three levels of local refinement	86

3.11	LES Validation: Time histories of T_1 , T_2 , and T_3 considering all pertinent heat transfer mechanisms and validation with experiment	87
3.12	y^+ profile and sensitivity to thermal boundary conditions employed	88
3.13	Snapshot of the isometric view of the temperature contours at $t = 180s$	89
4.1	Schematic of heat transfer across the wall and free stream in an adsorption column	94
4.2	Thermal resistance network in a fixed bed	95
4.3	Simplified schematic of the adsorption column for DCB simulations wherein the natural convection boundary condition is applied	97
4.4	2D axisymmetric computational domain of the adsorption column	97
4.5	Wall-fluid heat transfer coefficient, h_i , determined from the porous media model (PMM) and the PRCFD analysis in Chapter 2, compared with Yagi and Wakao ^[92] . All data points refer to the case $(\frac{k_s}{k_f}) = 1$	98
4.6	N_2 composition and temperature breakthrough curves predicted numerically for the 85 mol.% N_2 – 15 mol.% He system. (a) Composition breakthrough. (b) Centerline temperature front at $z = 0.8L$	101
4.7	CO_2 composition and temperature breakthrough curves predicted numerically for the 100% CO_2 – trace He system. (a) Composition breakthrough. (b) Centerline temperature front at $z = 0.8L$	103
4.8	2D contour snapshots of N_2 molar fraction (y_{N_2}) across the bed for the 85/15% N_2 /He case	104
4.9	2D contour snapshots of temperature (T, K) across the bed for the 85/15% N_2 /He case	105
4.10	2D contour snapshots of CO_2 molar fraction (y_{CO_2}) across the bed for the 100% CO_2 / trace He case	106
4.11	2D contour snapshots of temperature (T, K) across the bed for the 100% CO_2 / trace He case	107

4.12	CO ₂ temperature fronts predicted numerically for the 100% CO ₂ – trace He system. (a) Centerline, $T_{(r=0,z=0.8L)}$. (b) Wall, $T_{(r=R_w,z=0.8L)}$. (c) Radial Area Average, $\langle T_{(z=0.8L)} \rangle = \frac{\int_0^{R_w} r \cdot T_{(r,z=0.8L)} dr}{\int r dr}$	108
4.13	Case 1: Transient heat transfer coefficient and flux profiles corresponding to the exit wall face, $(r = R_w, z = L)$	110
4.14	Case 2: Transient heat transfer coefficient and flux profiles corresponding to the exit wall face, $(r = R_w, z = L)$	110

List of Symbols

Chapter 1 Nomenclature

Latin letters

b	Adsorption equilibrium constant for site 1
c	Fluid phase concentration
C_p	Specific heat capacity
d	Adsorption equilibrium constant for site 2
D_m	Molecular diffusivity
D_{eff}	Effective diffusivity
D_F	Fickian diffusivity of adsorbate within adsorbent particle
D_L	Dispersion coefficient
d_p	Particle diameter
d_t	Tube diameter
g	Gravitational acceleration
h	Heat transfer coefficient
H	Enthalpy
K	Permeability coefficient
k	Mass transfer coefficient, thermal conductivity

L	Domain length
M	Molar mass
n_{comp}	Number of components
p	Partial pressure
P	Fluid phase pressure
q	Solid phase loading
q^*	Equilibrium solid phase loading
Q	Volumetric flow rate
R_g	Universal gas constant
R_{in}	Column inner radius
R_{out}	Column outer radius
R_p	Radius of particle
T	Fluid and solid phase temperature
t	Physical time
ΔU	Internal Energy of adsorption
V	Volume
\vec{v}	Interstitial velocity
x	Species solid phase fraction
y	Species mole fraction
Y	Species mass fraction
z	z-coordinate

Greek letters

α	competitive selectivity
----------	-------------------------

ρ	density
ε	porosity or void fraction
μ	viscosity
Σ_v	diffusion volume
τ	tortuosity

Subscripts

b	bed
f	film
g	fluid phase
i	species i
iso	isosteric
m	mixture phase
p	adsorbent particle
t	tube

Chapter 2 Nomenclature

Latin letters

C_p	specific heat capacity
D	diameter
h	heat transfer coefficient
k	thermal conductivity
k_t	turbulent thermal conductivity
k_{eff}	effective thermal conductivity
$k - \omega$	k-omega SST turbulence model
L	length
N_p	number of particles
Nu	Nusselt number
p	fluid phase pressure
Pe	Peclet number
Pr	Prandtl number
q''	heat flux
R	radius
Re_p	particle Reynolds number based on superficial velocity
S	surface area
S	modulus of the mean rate-of-strain tensor
T	temperature
u_∞	inlet superficial velocity
\vec{v}	interstitial (local) velocity
V	volume

z z-coordinate

Greek letters

ρ density

ε porosity or void fraction

μ viscosity

τ_{ij} stress tensor

θ azimuthal angle in cylindrical coordinates

Subscripts

b bed/bulk

f fluid

p particle

t tube

w wall

Chapter 3 Nomenclature

Latin letters

C_p	Specific heat capacity
D	Diameter
g	Gravity
h	Heat transfer coefficient
H	Height
k	Thermal conductivity
L_c	Characteristic length
\hat{n}	Normal unit vector
Nu	Nusselt number
p	Fluid phase pressure
R	Radius
R^2	Coefficient of determination
Ra	Rayleigh number
t	Time
\vec{v}	Local velocity
Y	Water mass fraction
z	z-coordinate

Greek letters

α	Fluid thermal diffusivity
β	Fluid thermal expansion coefficient
δ	Cup thickness

δ_t	Thermal boundary layer
ε	Emissivity
ρ	Density
μ	Molecular (dynamic) viscosity
ν	Kinematic viscosity
σ	Stefan-Boltzmann constant
τ_{ij}	Stress tensor
θ	Azimuthal angle in cylindrical coordinates
ϕ	Relative humidity
φ	Angle of cup inclination

Subscripts

<i>conv</i>	convective
<i>evap</i>	evaporative
<i>f</i>	fluid
<i>i</i>	inner
<i>o</i>	outer
<i>rad</i>	radiative
<i>s</i>	surface
Σ	sum
<i>w</i>	wall
∞	ambient

Abbreviations

BC	Boundary Condition
CFD	Computational Fluid Dynamics
CHT	Conjugate Heat Transfer
CSS	Cyclic Steady State
DCB	Dynamic Column Breakthrough
DEM	Discrete Element Method
DNS	Direct Numerical Simulations
DSL	Dual Site Langmuir
FEM	Finite Element Method
FVM	Finite Volume Method
KPI	Key Performance Indicator
LDF	Linear Driving Force
LES	Large Eddy Simulations
RANS	Reynolds Averaged Navier Stokes
PDE	Partial Differential Equation
PMM	Porous Media Model
PRCFD	Particle-resolved CFD
P(V)SA	Pressure (Vacuum) Swing Adsorption
SIMPLE	Semi-Implicit Method for Pressure Linked Equations
SST	Shear Stress Transport
TSA	Temperature Swing Adsorption
UDF	User-Defined Function

Chapter 1

Introduction to Adsorption

Mixing is spontaneous. It is the separation of gases in a mixture that requires energy to be expended. Such technologies as cryogenic distillation, membrane separation, and adsorption have been used extensively based on the purity specification and amount of feed to be processed. Cryogenic distillation relies on the difference in boiling points of gases for separation. Membrane gas separation works on the principle of chemical affinity and diffusion: atoms with larger kinetic diameters (and thus correspondingly smaller diffusion coefficients) would encounter more collisions with other atoms and thus permeate slower across a membrane. Adsorption is based on the principle of differential chemical affinity of the components to the solid surface.

Adsorption is a separation process wherein molecules physically or chemically bind to the surface of solids or at active sites within porous solids. Eventually, equilibrium is attained between the bulk fluid concentration and the amount of solid adsorbed (called adsorbate) at the surface (known as adsorbent). Adsorption equilibrium has been quantified using isotherms, isobars, and isoterres (pressure vs temperature at constant coverage). Adsorption is almost always exothermic; however, it has been reported by [De Boer](#) that the dissociative chemisorption of molecular hydrogen on uncontaminated glass required considerable activation energy of the order $-15 \text{ kcal mol}^{-1}$ ^[1,2].

Gas adsorption finds application in various fields including but not limited to oxygen concentration from air^[3-5], hydrogen purification from steam methane reforming^[6-8], Helium purification from Natural gas^[9,10], volatile organic compounds removal^[11-13] and isotope separa-

tion^[14]. The prominent role of anthropological CO₂ emissions accelerating climate change^[15] has prompted several adsorption studies on carbon capture and sequestration^[16-21]. This has facilitated developments in adsorbent candidate materials and pellet structure design, experimental investigations into adsorption cycle optimization, and advances in numerical methods and computational modeling.

The two overarching steps involved in adsorptive gas separation are (i) preferential adsorption of a particular gas component from the fluid phase to the solid phase as the gas travels along the bed packed with catalyst pellets producing a product gas enriched in the component less adsorbed (light product) along the bed; and (ii) desorption of the more heavily adsorbed (heavy product) component by varying, or ‘swinging’, the condition(s) in the bed. The catalyst pellet materials are typically zeolites, activated carbon, mesoporous silica, or Metal-organic frameworks (MOFs)^[22,23]. Factors that determine material selection^[24] include: (i) cost; (ii) kinetics; (iii) adsorption capacity; (iv) component selectivity; (v) heat of adsorption; and (vi) thermal and chemical stability over several cycles of operation.

There are three primary bed regeneration techniques in line with Le Chatelier’s principle:

- Pressure Swing Adsorption (PSA) wherein desorption occurs by reducing the pressure and purging the bed. The adsorption step in PSA is typically conducted above atmospheric pressure with desorption at atmospheric pressure. Improved variants such as vacuum swing adsorption (VSA) and pressure vacuum swing adsorption (PVSA) employ vacuum pumps in the desorption stage for higher working capacities.
- Temperature Swing Adsorption (TSA) wherein desorption occurs as the bed is heated using hot air or steam to expunge the remaining gases trapped in the pellets and evacuate the bed. This is followed by re-cooling the bed for the next cycle. The time required for TSA bed regeneration is typically higher than that for a PSA process. Hence the PSA process is better suited for rapid cycling^[25].
=> Electric swing adsorption (ESA), a more recent development, employs Joule heating by conducting electricity through adsorbent^[26]. This allows for faster heating and improved desorption kinetics and dynamics vis-à-vis traditional TSA^[27].
- Purge gas stripping wherein an inert gas passed through the bed reduces the partial pressure of the adsorbate and causes it to desorb.

A typical gas adsorption PSA cycle, shown in Fig.(1.1), involves the following steps^[28]:

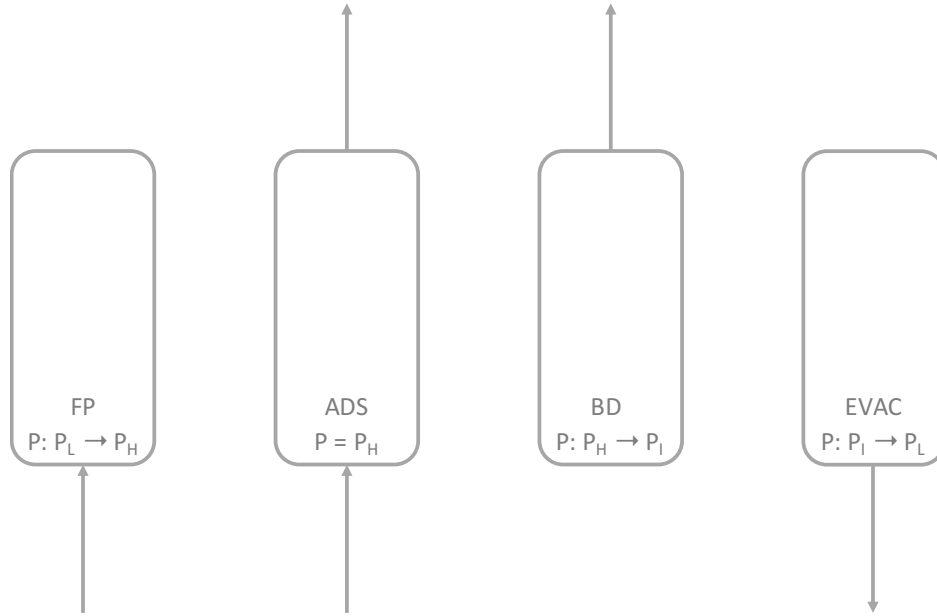


Figure 1.1: Schematic of a typical 4-step PSA cycle. (P: pressure, H: high, I: intermediate, L: low; FP: feed pressurization, ADS: adsorption, BD: blowdown, EVAC: evacuation)

- i) Feed Pressurization (FP): The feed valve is open, whereas the valve at the raffinate end is closed, also called the Open-Closed step. Feed is sent to the bed to build up pressure up to the desired adsorption pressure, called P_H .
- ii) Adsorption (ADS): With both feed and product valves open, the product gas rich in the light product is obtained. This is representative of the Open-Open step.
- iii) Blowdown (BD): The feed valve is closed once the bed is saturated with the heavy component. The adsorbate is evacuated from the bed by decreasing the bed pressure to a pressure intermediate to the adsorption and desorption pressures, called P_I . The blowdown process broadly removes any traces of the light component from the bed. This gas is reused in the system if the feed contains any vital components or is simply vented to the atmosphere. This is the Closed-Open step.
- iv) Evacuation (EVAC): By now, the bed is rich in the heavy product. The bed pressure is further reduced to the set desorption pressure, P_L , and the heavy product is recovered. Typically, the EVAC step is performed in the reverse direction, with the adsorbate

being removed from the bed via the feed valve. A slipstream of the light product from storage may be introduced in the bed from the raffinate valve to further purge any in situ remnants.

Owing to the semi-batch-like operation of the cyclic process, adsorption is an inherently unsteady state process. At least 2 (but often 3-4) or more beds operate synchronously to ensure continuous product output.

1.1 Benchmarking and Key Performance Indicators of an adsorption process

To benchmark an adsorption process cycle, four primary KPIs are evaluated^[28] once cyclic steady state (CSS) is reached.

1. Purity

Purity is defined as the mole fraction of the desired species in the outlet stream. Depending on whether the desired species is the light or heavy product, purity can be determined during the adsorption and desorption stages, respectively. Mathematically, purity is expressed as follows^[28]:

$$Purity[\%] = \left[\frac{\text{Moles of desired species in the product stream}}{\text{Total moles in the product stream}} \right] \times 100 \quad (1.1)$$

2. Recovery

Recovery is defined as the ratio of the amount of desired species that could be separated from the feed to the total amount of the desired component in the feed. Mathematically, recovery is expressed as follows^[28]:

$$Recovery[\%] = \left[\frac{\text{Moles of desired species in the product stream}}{\text{Moles of desired species in the feed}} \right] \times 100 \quad (1.2)$$

3. Productivity

Productivity is defined as the amount of desired species that could be separated per

unit amount of adsorbent per cycle and is expressed as follows^[28]:

$$Productivity \left[\frac{mol}{m^3 \text{ adsorbent} \cdot s} \right] = \frac{\text{Moles of desired species at outlet}}{(\text{Amount of adsorbent}) \cdot (\text{Cycle time})} \quad (1.3)$$

4. Energy consumption

Energy consumption is defined by the total energy expended in the cyclical process to separate unit mass of desired species per cycle and is expressed as follows^[28]:

$$\text{Energy consumed} \left[\frac{kWh}{ton} \right] = \frac{\text{Total energy expended per cycle}}{\text{Mass of desired component produced per cycle}} \quad (1.4)$$

The competitive **selectivity** of preferential adsorption of desired species i over species j , $\alpha_{i,j}$, in a binary mixture is defined as follows^[28]:

$$\alpha_{i,j} = \frac{q_i^*(y_i) y_j}{q_j^*(y_j) y_i} \quad (1.5)$$

where q_i is the adsorbed amount of species i and y_i is the gas phase species mole fraction.

Working capacity, also known as delta loading Δq_i [$mol \text{ kg}^{-1}$], is defined as the difference between adsorbed amounts of desired species i during the production and regeneration steps in an adsorption cycle. It is worthwhile to note that while working capacity and selectivity are essential parameters during adsorbent selection, they are not direct indicators of an adsorption cycle's performance but instead may be varied by tweaking operating parameters.

1.2 Adsorption process modeling

Due to the inherently transient nature of an adsorption process, it is crucial to understand process dynamics within the adsorption column. One must consider coupled transport phenomena (material, momentum, and energy balances), thermodynamics, adsorption equilibrium isotherms, adsorption kinetics, and adsorber design to model column dynamics [Fig.(1.2)].

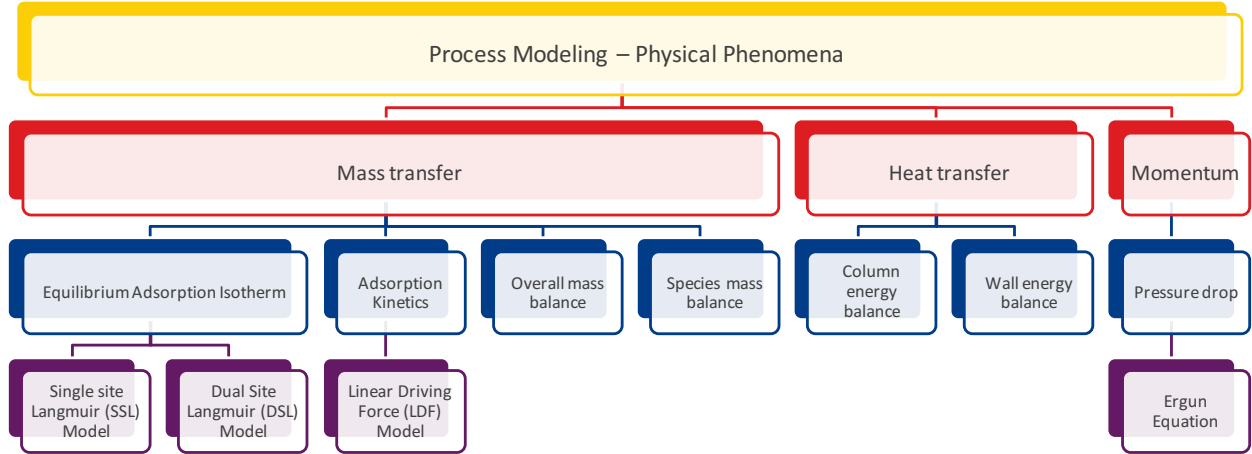


Figure 1.2: Overview of the elements of modeling the physical phenomena involved in an adsorption process

1.2.1 Adsorption equilibrium

A key aspect of process modeling is establishing equilibrium between the fluid and adsorbent. Several isotherms have been proposed and refined over the decades. Parameters are empirically fitted for a given system using laboratory techniques of gravimetry (mass-based) and volumetry (volume-based) at different operating conditions of pressures and temperatures.

The most trivial isotherm is the Single Site Langmuir (SSL)^[29], which assumes there exists a finite amount of homogeneously-distributed active sites of a single type, each site having the same enthalpy of adsorption. Each site can accommodate a single adsorbent molecule, and adsorbed molecules do not interact with each other.

A single component system would have the following equilibrium isotherm^[29]:

$$q^* = \frac{q^{sat} \cdot bp}{1 + bp} \quad (1.6)$$

where q^* is the equilibrium solid phase concentration, q^{sat} is the saturated solid phase concentration, p is the partial pressure, b is the temperature-dependent adsorption equilibrium constant described by the Arrhenius equation^[30]:

$$b = b_0 \exp\left(\frac{-\Delta U}{R_g T}\right) \quad (1.7)$$

Here, ΔU is the internal energy of adsorption. It is related to the isosteric heat of adsorption, H_{iso} as follows^[31]:

$$\Delta U = \Delta H_{iso} + R_g T \quad (1.8)$$

H_{iso} can be calculated using experimentally obtained pressure and temperature readings from the Clausius-Clapeyron equation as follows^[31]:

$$\left[\frac{\partial \ln(p_i)}{\partial \left(\frac{1}{T} \right)} \right]_{q_i^*} = - \frac{\Delta H_{iso}}{R_g} \quad (1.9)$$

Competition among different species at the adsorption sites is common, and it is essential to account for competitive equilibria. In extension, the equilibrium isotherm for species i in a multi-component system is as follows^[29]:

$$q_i^* = \frac{q_i^{sat} \cdot b_i p_i}{1 + \sum_{j=1}^{n_{comp}} b_j p_j} \quad (1.10)$$

It is important to note that the loading of the lighter product due to the heavy product is more sensitive than vice-versa. This calls for scrutiny of light product loading.

Due to relative variance in the characteristics of adsorption of various fluid phase species at the solid surface, the SSL model is sometimes insufficient to fit thermodynamic equilibrium. Therefore a dual-site Langmuir (DSL) model has been proposed. The DSL model recognizes that adsorption need not necessarily be structurally and energetically homogeneous.

Mathematically, the DSL model for an n_{comp} system with two types of active sites, say the strong ‘ b ’ and the weak ‘ d ’ type sites, would be formulated as follows^[29,30]:

$$q_i^* = \frac{q_{b,i}^{sat} \cdot b_i p_i}{1 + \sum_{j=1}^{n_{comp}} b_j p_j} + \frac{q_{d,i}^{sat} \cdot d_i p_i}{1 + \sum_{j=1}^{n_{comp}} d_j p_j} \quad (1.11)$$

$$b_i = b_{0,i} \exp \left(\frac{-\Delta U_{b,i}}{R_g T} \right) \quad (1.12)$$

$$d_i = d_{0,i} \exp\left(\frac{-\Delta U_{d,i}}{R_g T}\right) \quad (1.13)$$

where $q_{b,i}^{sat}$ and $q_{d,i}^{sat}$ are solid phase saturation loading of sites b and d respectively. The total saturation capacity of species i is given as follows:

$$q_i^{sat} = q_{b,i}^{sat} + q_{d,i}^{sat} \quad (1.14)$$

The Toth isotherm has also been considered in certain adsorption studies^[32]. The Toth isotherm for a pure component system is a three-parameter model given as follows^[32]:

$$q^* = \frac{q^{sat} \cdot bp}{(1 + (bp)^t)^{1/t}} \quad (1.15)$$

where t is the Toth isotherm exponent related to surface heterogeneity. Typically, $t \leq 1.0$ ^[33] and is temperature-independent. The further away t is from unity, the more heterogeneity in the system. When $t = 1$, Eq.(1.15) reduces to the single site Langmuir isotherm given by Eq.(1.6).

There are a few other adsorption isotherm models, such as the Freundlich model (1906), the Sips model (1948), the Temkin model (1940), and the Brunauer, Emmett, and Teller (BET) model (1938). The reader is referred to the review article by Wang and Guo^[34] outlining 13 isotherm models, including empirical models, semi-empirical models based on Polanyi's potential theory, and chemical, physical, and ion exchange isotherm models.

1.2.2 Adsorption mass transfer kinetics

Understanding and characterizing the diffusion from the bulk to the solid phase is critical. The mathematical formulation for the Fickian Diffusion model for isothermal mass transfer in a spherical particle for species i in terms of the Fickian Diffusivity, D_F , is as follows^[35]:

$$\frac{\partial q_i}{\partial t} = \frac{1}{r^2} \frac{\partial}{\partial r} \left[r^2 \left(\varepsilon_p D_F \frac{\partial q_i}{\partial r} \right) \right] \quad (1.16)$$

The Linear Driving Force model (LDF), proposed originally by Glueckauf and Coates^[36],

is widely employed in numerical modeling of the rate of mass transfer due to its simplicity and reliability. [Sircar and Hufton](#)^[35] validated the practicality of the LDF model over the more rigorous Fickian Diffusion (FD) model for cyclical gas adsorption. It was found that the variance in kinetics, determined by the adsorption uptake curves, is diminished over the cyclic steady-state process. The LDF model thus reduces the dimensional cost of calculating mass transfer kinetics by doing away with the particle spatial coordinate dependency.

The LDF model assumes that the rate of internal diffusion of particles is much faster than the external convective mass transfer rate. It postulates that the rate of uptake of species i into the solid adsorbent is directly proportional to the difference between the equilibrium concentration of the species at the surface, q_i^* , and the average species concentration within the particle, q_i . The mathematical formulation of the LDF model for species i is as follows^[37]:

$$\frac{\partial q_i}{\partial t} = k_i (q_i^* - q_i) \quad (1.17)$$

where, $q_i^* = q_i^*(y, P, T)$ is the solid phase equilibrium concentration for the component ‘ i ’ that could be determined from the appropriate adsorption isotherm discussed in Sec.(1.2.1). k_i is the lumped mass transfer coefficient obtained by accounting for external film, macropore, and micropore resistances as follows^[38]:

$$\frac{1}{k_i} = \underbrace{\frac{d_p}{6k_{f,i}} \left(\frac{q_i^*}{c_i} \right)}_{\equiv \text{external film resistance}} + \underbrace{\frac{d_p^2}{60\varepsilon_p D_{p,i}} \left(\frac{q_i^*}{c_i} \right)}_{\equiv \text{macropore resistance}} + \underbrace{\frac{d_c^2}{60D_{c,i}}}_{\equiv \text{micropore resistance}} \quad (1.18)$$

where, ε_p is the pellet porosity. d_p is the adsorbent pellet diameter whereas d_c is the adsorbent crystal/micropore diameter. c_i [mol/m³] is the fluid phase concentration of species i .

$k_{f,i}$, $D_{p,i}$, and $D_{c,i}$ are the species-specific film mass transfer coefficient, macroporous diffusion coefficient, and microporous diffusion coefficient, respectively. For the cases when molecular diffusion in the macropores is the dominant mechanism of mass transfer, particularly in

zeolite-based air separation processes^[3,28,38], Eq.(1.18) reduces to:

$$k_i = \frac{60 \cdot D_{eff} c_i}{d_p^2 q_i^*} \quad (1.19a)$$

$$D_{eff} = \frac{\varepsilon_p D_m}{\tau} \quad (1.19b)$$

D_{eff} is the effective diffusivity dependent on the gas phase molecular diffusivity D_m , particle porosity ε_p , adsorbent tortuosity τ . D_m can be calculated from the kinetic theory of gases via the Chapman-Enskog formulation^[39,40] or Fuller^[41] correlation, as shown below.

$$D_{m,Fuller} = \frac{1.013 \times 10^{-2} T^{1.75} (1/M_1 + 1/M_2)}{P \left((\Sigma v)_1^{1/3} + (\Sigma v)_2^{1/3} \right)^2} \quad (1.20)$$

Note that Eq.(1.20) is only valid for a binary mixture (species 1 and 2).

1.2.3 Material balance

Considering a fixed bed of length L packed with adsorbent particles, the fluid phase component mass balance is given by:

$$\varepsilon \frac{\partial (\rho_g Y_i)}{\partial t} + \nabla \cdot (\varepsilon \rho_g \vec{v} Y_i) = \nabla \cdot (\varepsilon \rho_g D_L \nabla Y_i) - \underbrace{(1 - \varepsilon) \rho_p \left(M_i \frac{\partial q_i}{\partial t} \right)}_{S_{m,i}} \quad (1.21)$$

where Y_i is the mass fraction of species i , q_i is in mol/kg, $M_i[kg/mol]$ is the molar mass of the species i adsorbed, ρ_p is the density of the adsorbent particles. $S_{m,i}$ denotes the mass source/sink term of species i .

The turbulent mixing arising out of turbulence in the void spaces of the packed bed necessitates a reformulation of the diffusion coefficient. The effect of this flow-dependent convective term and flow-independent molecular diffusion D_m may be consolidated into a single coefficient known as the axial dispersion coefficient, D_L . D_L could be calculated in

the following ways:

$$D_L = 0.7D_m + 0.5\frac{u_\infty d_p}{\varepsilon} \quad (1.22a)$$

$$D_L = \frac{u_\infty d_p}{0.508 Re_p^{0.02}} \quad (1.22b)$$

a \equiv Wakao and Funazkri^[42], b \equiv Ben-Mansour et al.^[43]

The overall mass balance equation is obtained by adding the component mass balance equations for all the components. The dispersive term, (D_L), vanishes since $\sum_{i=1}^{n_{comp}} Y_i = 1$.

$$\varepsilon \frac{\partial \rho_g}{\partial t} + \nabla \cdot (\varepsilon \rho_g \vec{v}) = S_m = -(1 - \varepsilon) \rho_p \sum_{i=1}^{n_{comp}} \left(M_i \frac{\partial q_i}{\partial t} \right) \quad (1.23)$$

S_m denotes the overall mass source/sink term and is typically non-zero due to mass transfer between the fluid and the solid phases.

$$S_m = \sum_{i=1}^{n_{comp}} S_{m,i}$$

1.2.4 Energy balance

The thermal effects of an adsorption process are accounted for by an energy source term, the second term on the right-hand side (RHS) of Eq.(1.24). The amount of heat released is directly related to the rates at which each species is adsorbed, and it is determined by their respective enthalpies of adsorption, denoted as ΔH_i . The last two terms on the RHS of Eq.(1.24) are heat sink terms, accounting for the increased thermal mass of the solid bed due to the adsorption of species. This increase in thermal inertia (resistance to change in temperature gradients) is in accordance with the cumulative sum of the respective amounts and heat capacities of each adsorbed species.

$$\begin{aligned}
\frac{\partial}{\partial t} (\varepsilon \rho_g C_{p,g} T + (1 - \varepsilon) \rho_p C_{p,p} T) + \underbrace{\nabla \cdot (\varepsilon \rho_g \vec{v} C_{p,g} T)}_{\text{convection}} &= \underbrace{\nabla \cdot (\varepsilon k_{eff} \nabla T)}_{\text{diffusion}} \\
+ (1 - \varepsilon) \rho_p \sum_{i=1}^{n_{comp}} \left((-\Delta H_i) \frac{\partial q_i}{\partial t} \right) - (1 - \varepsilon) \rho_p \sum_{i=1}^{n_{comp}} \left(C_{p,i} M_i T \frac{\partial q_i}{\partial t} \right) & \\
- (1 - \varepsilon) \rho_p \sum_{i=1}^{n_{comp}} \left(C_{p,i} M_i q_i \frac{\partial T}{\partial t} \right) & \quad (1.24)
\end{aligned}$$

where $C_{p,g}$, $C_{p,p}$ and $C_{p,i}[J/kg/K]$ are the specific heat capacities of the fluid, adsorbent, and adsorbed species i , respectively. $\Delta H_i[J/mol]$ is the heat of adsorption of species i . k_{eff} is the effective thermal conductivity of the mixture, calculated within the solver as the porosity-weighted average between the gas-phase and solid-phase thermal conductivities, k_g and k_s , respectively.

$$k_{eff} = \varepsilon \cdot k_g + (1 - \varepsilon) \cdot k_s \quad (1.25)$$

1.2.5 Momentum balance

The general Navier-Stokes momentum conservation equation is as follows:

$$\begin{aligned}
\underbrace{\frac{\partial(\rho_g \vec{v})}{\partial t} + \nabla \cdot (\rho_g \vec{v} \vec{v})}_{\equiv \text{Inertial forces}} &= \underbrace{-\nabla P}_{\text{Pressure forces}} + \underbrace{\nabla \cdot (\mu_g (\nabla \vec{v} + \nabla \vec{v}^T))}_{\text{Viscous forces}} - \underbrace{\frac{\varepsilon \mu_g \vec{v}}{K}}_{\text{Porous media source term}} \quad (1.26)
\end{aligned}$$

where ε represents the bed voidage, ρ_g is the fluid density, and μ_g denotes the dynamic (molecular) viscosity of the bulk fluid. \vec{v} is the local (interstitial) velocity.

The momentum conservation equation does not involve any source term related to adsorption but contains viscous and inertial resistance terms. The term $\frac{1}{K}$ is known as the inverse permeability and is obtained from the Carman-Kozeny equation^[44]:

$$\frac{1}{K} = \frac{150 (1 - \varepsilon)^2}{d_p^2 \varepsilon^3} \quad (1.27)$$

The momentum loss caused by the resistance when gas flows through porous media translates to a pressure drop in the fixed bed. For a 1D steady-state model $P = P(z)$,

the pressure along the length of the column may be represented in terms of the superficial velocity, u , and modeled using the Ergun equation^[45] as follows.

$$-\frac{\partial P}{\partial z} = \frac{150}{d_p^2} \frac{(1-\varepsilon)^2}{\varepsilon^3} \mu_g u + \frac{1.75(1-\varepsilon)}{d_p \varepsilon^3} \rho_g u^2 \quad (1.28)$$

It should be emphasized that instead of the Ergun equation, the Einfeld-Schnitzelin equation^[46] may be considered to account for the wall channeling effect on the pressure drop. However, [Kuncharam and Dixon](#) have demonstrated that both models produce almost the same results in terms of the heat and mass transfer predictions^[47].

1.3 Developments in numerical methods and computational modeling of fixed bed columns for adsorption

The reader is referred to the review articles by [Shafeeyan et al.](#)^[48], [Ben-Mansour et al.](#)^[43] and [Akinola et al.](#)^[49] that focus on prior mathematical modeling studies related to CO₂ adsorption from such various mixtures as air, coke oven gas, cracked gas, flue gas, etc.

[Ben-Mansour et al.](#) reflect on a plethora of CO₂ adsorption modeling studies. Of the 26 studies reviewed, all were 1D transient models, assumed ideal gas behavior, and considered the LDF model for adsorption kinetics. While a majority incorporated some variant of the non-linear Langmuir isotherm for adsorption equilibrium, a couple of studies used the Toth isotherm^[32]. While earlier studies neglected pressure drop along the bed, later studies employed the Ergun equation in an axial dispersed plug flow model to account for pressure and velocity profiles. With advances in computing power, we observe a shift in the numerical methods from the finite difference method to the finite element method (e.g., COMSOL) and the finite volume method (e.g., FLUENT).

Framing shell balances gives rise to a system of coupled partial differential equations (PDEs) distributed over time and space, along with transport rates and equilibrium equations. Such systems often do not possess analytical solutions and, thus, need to be solved numerically. The Finite Volume Method (FVM) has been widely employed across various adsorption simulations^[50–55]. The FVM is more robust vis-à-vis Finite Difference, Finite

Element Method (FEM), or orthogonal collocation^[54–56] since integral equations allow for better closure of mass, momentum, and energy balances over differential equations. Dynamic Column Breakthrough (DCB), cyclic PSA, and pulse injection simulations employed various numerical schemes, including adaptive QUICK, adaptive multi-resolution, SMART, HR, and WENO, for rigorous solution optimization. Due to the nature of the heat and mass conservation equations involved and the sharp propagation of the concentration along the bed, it is crucial to implement numerical schemes adept at stiff problems for accuracy and stability. Systems with highly non-linear isotherms considerably benefit from refined numerical schemes.

The prominent choice for modeling transport phenomena has been 1D models. Equations are often coded and solved on programming platforms such as MATLAB, Fortran, PDECOL, DGEAR, ODEPACK, etc. 1D models can efficiently predict the behavior of temperature and composition along the axial direction of the adsorption column. These, however, do not wholly account for hydrodynamic phenomena, including the wall-channeling effects and flow & heat transfer asymmetries. These inherent limitations of 1D models have led to Computational Fluid Dynamics (CFD) gaining popularity in multidimensional adsorption simulations. Continuous improvement for increased throughput, scalability, and techno-economic feasibility necessitates the application of multidimensional modeling of adsorption processes. CFD allows for a detailed resolution of each transport equation involved down to a differential or ‘cell’ scale. Although commercial CFD packages include a module for porous media, they lack certain models to adequately simulate adsorption in packed beds, such as a rate equation for solid-gas mass transfer kinetics. Thus, significant effort shall be devoted to programming the transport equations involved in an adsorption process in packed beds. Source code documentation of the user-defined functions (UDFs, compiled in C) is essential for continuity and knowledge transfer purposes. Finally, it should be noted that any CFD-based adsorption model must be validated against experimental data before implementation to upscaling simulations of actual industrial-scaled separation columns.

Further studies have been undertaken to improve process design and cycle performance. [Wilkins and Rajendran](#) measured competitive adsorption of CO₂ and N₂ on Zeolite 13X and underscored the need for proper characterization of competitive adsorption^[57]. With

experimental validation and integral balances, they concluded that the key KPIs - purity, recovery, energy, and productivity - were affected by the choice of the competitive adsorption isotherm.

1.3.1 A case study in carbon dioxide adsorption modeling

Aiming to investigate CO_2 capture and concentration, [Haghpanah et al.](#) consider a mixture of CO_2 and N_2 , the primary components in flue gas^[19]. The zeolite of choice is Zeolite 13X since it is insensitive to moisture; CO_2 is the heavy product that adsorbs strongly to 13X. [Haghpanah et al.](#) develop a generalized PVSA model of a one-dimensional fixed bed, accounting for axial dispersion, heat effects, pressure drop along the bed, and velocity effects during cyclic operation.

The experimental setup is a small-scale lab reactor, enabling the outer wall to be maintained isothermally. The adsorption equilibrium data is determined experimentally using the gravimetry technique and are fitted to a dual-site Langmuir (DSL) model. The ideal gas approximation is applied to the gas phase. The linear driving force (LDF) model establishes mass transfer kinetics in the solid phase. Thermal equilibrium between the fluid and solid phases is established instantaneously, or in other words, a homogeneous continuum model is considered. Radial heat and mass effects are ignored. Macropore diffusion dominates over micropore or Knudsen diffusion. The adsorbent properties and bed voidage are assumed to be uniform across the column.

Considering the ideal gas assumption as the equation of state to relate measurable parameters, P and T to the mixture density ρ , the 1D material and energy balance equations discussed in section (1.2.3) and (1.2.4) reduce to the following:

$$\rho(z, t) = \frac{P(z, t)}{R_g T(z, t)} \quad (1.29)$$

1D species balance:

$$\frac{\partial y_i}{\partial t} + \frac{y_i}{P} \frac{\partial P}{\partial t} - \frac{y_i}{T} \frac{\partial T}{\partial t} = D_L \frac{T}{P} \frac{\partial}{\partial z} \left(\frac{P}{T} \frac{\partial y_i}{\partial z} \right) - \frac{T}{P} \left(\frac{\partial}{\partial z} \left(\frac{y_i P}{T} v \right) \right) - \frac{RT}{P} \left(\frac{1 - \varepsilon}{\varepsilon} \right) \frac{\partial q_i}{\partial t} \quad (1.30)$$

1D overall material balance:

$$\frac{1}{P} \frac{\partial P}{\partial t} - \frac{1}{T} \frac{\partial P}{\partial t} = -\frac{T}{P} \frac{\partial}{\partial z} \left(\frac{P}{T} v \right) - \frac{RT}{p} \frac{1-\varepsilon}{\varepsilon} \sum_{i=1}^{n_{comp}} \frac{\partial q_i}{\partial t} \quad (1.31)$$

where D_L is the axial dispersion coefficient, y_i is the mole fraction of the fluid phase component 'i', c_i and q_i are the fluid and solid phase concentrations of component 'i' respectively, v is the interstitial velocity in the axial direction, z is the axial distance, P is the pressure, T is the temperature and t is the time.

Due to temperature gradients within the bed and heat transfer between the bed and the surroundings, two parameters must be resolved - the temperature of the bed, T , and the temperature of the wall, T_w .

1D column energy balance:

$$\left[\left(\frac{1-\varepsilon}{\varepsilon} \right) \left(\rho_s C_{p,s} + C_{p,a} \sum_{i=1}^{n_{comp}} q_i \right) \right] \frac{\partial T}{\partial t} = \frac{K_z}{\varepsilon} \frac{\partial^2 T}{\partial z^2} - \frac{C_{p,g}}{R} \frac{\partial}{\partial z} (vp) - \frac{C_{p,g}}{R} \frac{\partial P}{\partial T} - \left(\frac{1-\varepsilon}{\varepsilon} \right) C_{p,a} T \sum_{i=1}^{n_{comp}} \frac{\partial q_i}{\partial t} + \left(\frac{1-\varepsilon}{\varepsilon} \right) \sum_{i=1}^{n_{comp}} \left[(-\Delta H_i) \frac{\partial q_i}{\partial t} \right] - \frac{2h_{in}}{\varepsilon r_{in}} (T - T_w) \quad (1.32)$$

1D wall energy balance:

$$\rho_w C_{p,w} \frac{\partial T_w}{\partial t} = K_w \frac{\partial^2 T_w}{\partial z^2} + \frac{2r_{in} h_{in}}{r_{out}^2 - r_{in}^2} (T - T_w) - \frac{2r_{out} h_{out}}{r_{out}^2 - r_{in}^2} (T_w - T_{amb}) \quad (1.33)$$

where T_w is wall temperature, T_{amb} is ambient temperature, ρ_s and ρ_g denotes the density of solids and gas phase, $C_{p,g}$, $C_{p,s}$ and $C_{p,a}$ represents heat capacities of the gas phase, solid phase, and adsorbed phase respectively, ΔH_i is the heat of adsorption of component i, K_z is the thermal conductivity of the bed in the axial direction, r_{in} is the column inner radius, r_{out} is the column outer radius, h_{in} and h_{out} are inside and outside heat transfer coefficient respectively.

This leads to a system of partial differential equations in 2 independent variables (z, t) with $(n_{comp} - 1) + 3$ dependent variables:

- Species balance: $y_1(z, t), y_2(z, t), y_3(z, t), \dots, y_{n_{comp}-1}(z, t)$

$y_{n_{comp}}(z, t)$ is determined directly as $y_{n_{comp}} = 1 - \sum_{i=1}^{n_{comp}-1} y_i(z, t)$

- Column temperature, $T(z, t)$
- Wall temperature, $T_w(z, t)$
- Column Pressure, $P(z, t)$

As per the steps outlined in a cyclical PSA process, the boundary conditions vary during the feed pressurization, adsorption, blowdown, and evacuation processes. Boundary conditions for the dependent variables, T , T_w , y_i from $i = 1 \dots (n_{comp} - 1)$ and Pressure P or velocity v must be specified, as shown in Table 1.1.

Table 1.1: Boundary conditions for the steps in PSA cycle

Step	z=0	z=L
Open-Open	$D_L \frac{\partial y_i}{\partial z} \Big _{z=0} = -v \Big _{z=0} (y_{i,feed} - y_i \Big _{z=0})$	$\frac{\partial y_i}{\partial z} \Big _{z=L} = 0$
	$K_z \frac{\partial T}{\partial z} \Big _{z=0} = -\varepsilon \rho_g C_{p,g} v \Big _{z=0} (T_{feed} - T \Big _{z=0})$	$\frac{\partial T}{\partial z} \Big _{z=L} = 0$
	$T_w \Big _{z=0} = T_a$	$T_w \Big _{z=L} = T_a$
	$v \Big _{z=0} = v_{feed}$	$P \Big _{z=L} = P_H$
Open-Closed	$D_L \frac{\partial y_i}{\partial z} \Big _{z=0} = -v \Big _{z=0} (y_{i,feed} - y_i \Big _{z=0})$	$\frac{\partial y_i}{\partial z} \Big _{z=L} = 0$
	$K_z \frac{\partial T}{\partial z} \Big _{z=0} = -\varepsilon \rho_g C_{p,g} v \Big _{z=0} (T_{feed} - T \Big _{z=0})$	$\frac{\partial T}{\partial z} \Big _{z=L} = 0$
	$T_w \Big _{z=0} = T_a$	$T_w \Big _{z=L} = T_a$
	$P \Big _{z=0} = P_2 + (P_1 - P_2)e^{-\alpha_p t}$	$v \Big _{z=L} = 0$
Closed-Open	$\frac{\partial y_i}{\partial z} \Big _{z=0} = 0$	$\frac{\partial y_i}{\partial z} \Big _{z=L} = 0$
	$\frac{\partial T}{\partial z} \Big _{z=0} = 0$	$\frac{\partial T}{\partial z} \Big _{z=L} = 0$
	$T_w \Big _{z=0} = T_a$	$T_w \Big _{z=L} = T_a$
	$v \Big _{z=0} = 0$	$P \Big _{z=L} = P_1 + (P_2 - P_1)e^{-\alpha_p t}$

As a first case study, dynamic column breakthrough simulation is performed. DCB is essentially the adsorption stage with both the feed and product lines open. The profile at

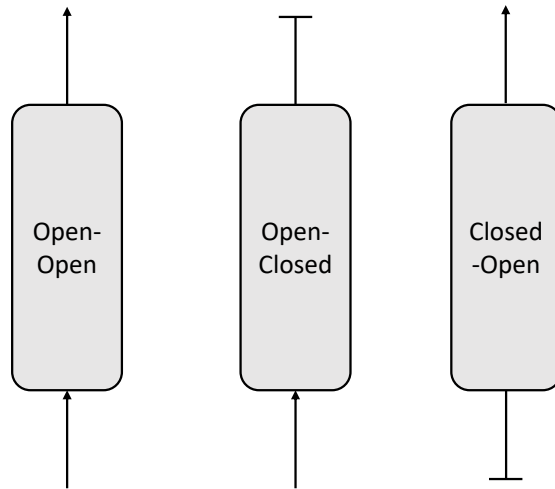


Figure 1.3: Typical constituent steps in a cyclic adsorption process

the exit is monitored for the presence of CO_2 , it being the heavier product and would break through the bed only when the bed is fully saturated with CO_2 . There are two transitions to be expected. The first when CO_2 is first observed at the exit and the second when the heat front departs from the column. Cyclic steady state (CCS) is declared to have been attained when the mass balance error for five consecutive cycles is $\leq 0.5\%$. Comparison among different numerical schemes concluded that a combination of the WENO and HR schemes implemented along with flux limiters would be best suited, touting a balance among accuracy, stability, and computational cost.

For the next phase of the study, a four-step PVSA cycle (Feed pressurization \rightarrow Adsorption \rightarrow Forward blowdown \rightarrow Reverse evacuation) was optimized. The objectives were to maximize CO_2 purity (mandated $\geq 90\%$ ^[58]) and recovery while simultaneously maximizing productivity and minimizing the ‘parasitic energy’ (the energy penalty for carbon capture and concentration). This involved global optimization of the following operating parameters: duration of the cycles, operating pressures, and feed inlet velocity. Pareto curves aided in concluding that a VSA system ($P_H = 1$ bar) would be highly strained to achieve a simultaneous 90% purity and 90% recovery. The minimum energy penalty incurred in the optimized VSA cycle was about 11%. Pressurizing the feed above atmospheric pressure would be further energetically unfavorable. However, it could meet the purity-recovery target without deep vacuum while reducing the plant unit operation size and capital expenditure.

1.4 CFD modeling of heat transfer and adsorption processes in fixed beds

Fixed bed CFD modeling is broadly categorized into the porous medium model (PMM) approach and the particle-resolved CFD (PRCFD) approach. Most CFD solvers (ANSYS Fluent, OpenFOAM, StarCCM+, etc.) and COMSOL Multiphysics offer a module for porous media simulations. The porous medium model considers the fixed bed as a continuum system and includes the impact of particles on fluid flow through source terms that account for momentum loss rather than explicitly modeling the particles themselves. These source terms, containing resistance due to viscous and inertial losses, are incorporated into the Navier–Stokes equations for an incompressible Newtonian fluid. However, the PMM cannot fully capture the radial variation in axial flow, which is important in reactor modeling. The radial variation of porosity distribution $\varepsilon(r, z)$ is often neglected and simplified to either an averaged ‘bed’ porosity, ε_b , to simulate the densely packed geometry or an exponential profile that only captures the near-wall voidage surge. Particle-resolved CFD inherently circumvents this simplification.

Variation in porosity near the wall has been known to affect flow characteristics in the fixed bed. The residence time distribution, fluid holdup, and pressure drop are sensitive to the near-wall porosity profile. [De Klerk](#) derived the following correlation, valid for a fixed bed randomly packed with mono-disperse spheres with $d_t/d_p > 2$, to express oscillatory voidage variation in the near wall region^[59].

$$\varepsilon(r) = \begin{cases} z^2 - 2.53z + 1 & z \leq 0.637 \\ \varepsilon_b + 0.29\exp(-0.6z) \cdot [\cos(2.3\pi(z - 0.16))] + 0.15\exp(-0.9z) & z > 0.637 \end{cases} \quad (1.34)$$

where, ε_b is the bed porosity in the absence of wall effects and z is the non-dimensionless distance from the wall given as $z = \frac{(R - r)}{d}$. For dense random packing, obtained by shaking down or vibrating the packed bed, $\varepsilon_b \approx 0.36$.

[Wu et al.](#) investigated the thermal-hydraulic characteristics in a pebble bed reactor (PBR) predicted by the Reynolds-averaged Navier–Stokes (RANS) CFD model via the PMM and

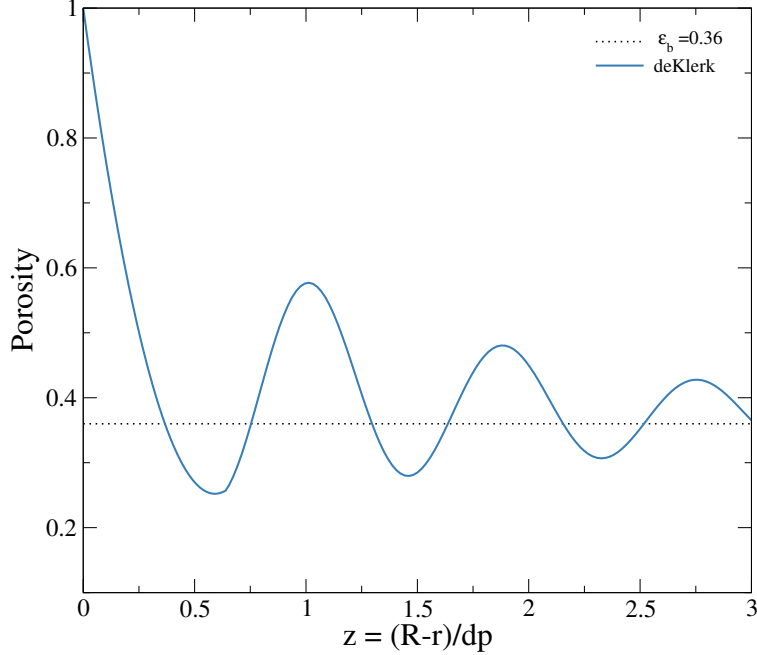


Figure 1.4: Radial porosity profile of a densely packed fixed bed^[59]

the PRCFD approaches^[60]. A key observation was that while the PMM model could reasonably predict the pressure gradient and spatial-averaged temperature increase, it failed to capture secondary flows and flow anisotropies, such as separation, oscillation, and vortex formation. The mesh for the PRCFD approach required ~ 75 times the control volumes and ~ 2400 times the computational time compared to the PMM approach. A simplification in their study was that they used only a cubical segment of the PBR consisting of 28 pebbles in a structured staggered configuration. The assumption of periodic packing and the use of the symmetry boundary condition on the sides of the segment is not the most accurate characterization of the entire bed.

Guardo et al. performed PRCFD calculations to investigate flow and heat transfer in low d_t/d_p non-regularly packed fixed beds^[61]. The authors extended their investigations evaluating the Spalart–Allmaras, standard $k-\varepsilon$, RNG $k-\varepsilon$, realizable $k-\varepsilon$ and the standard $k-\omega$ models^[62]. It was found that the former was preferable based on pressure drop computations vis-à-vis the Ergun equation and the Nu_w vs. Re_p trend validated against empirical correlations in literature. This was attributed to the former incorporating coupling between wall functions and damping functions for near-wall treatment and neglecting additional diffusion

or dissipation terms in its formulation. Also, the Spalart Allmaras, unlike the two-equation $k - \varepsilon$ RANS models, does not present the stagnation point anomaly.

Since then, the $k - \omega$ - SST (Shear Stress Transport) model has gained popularity over the standard $k - \omega$ model due to being less sensitive to freestream turbulence. It blends $k - \omega$ near the wall with a transformed $k - \varepsilon$ model. The $k - \omega$ - SST model provides a better prediction of flow separation than most RANS models, even in adverse pressure gradients.

More recently, [Tabib et al.](#) applied the CFD–DEM technique to assist in the design of industrial reactors packed with various pellet shapes^[63]. The realizable $k - \varepsilon$ turbulence model with standard wall function treatment was used. The computationally-prohibitive nature of simulating industrial scale reactors ($d_t/d_p > 40$) due to meshing constraints is recognized.

[Das et al.](#) conducted a fully resolved direct numerical simulation (DNS) study for slender packed bed reactors^[64]. A few prior CFD modeling studies on hydrodynamics and heat transfer in fixed beds have been reviewed. A shortcoming of those studies was the use of the RANS turbulence models without adequate resolution of the boundary layers at the particle surfaces. [Das et al.](#) employed the conjugate heat transfer (CHT) model wherein the energy equations are solved simultaneously for the solid and fluid phases while satisfying the continuity of temperature and heat flux at the fluid-solid interface.

The number of control volumes (CVs) increases exponentially with increasing d_t/d_p , and linearly with increasing bed length. Increasing the number of particles in a given geometry rapidly increases the computational complexity of the geometry, particularly around the contact points between solids and particle-wall contact. [Nijemeisland and Dixon](#) estimated that an industrial steam reforming bed about 13m long with $d_t/d_p = 4$ would contain ~ 7200 particles^[65]. Reactor CFD modeling of the reactor would require a mesh containing a cumbersome 600 million CVs, impractical even for today’s high performance computing systems.

Advances in CFD modeling of adsorption processes

[Augier et al.](#) carried out CFD simulations to explore hydrodynamic effects in both laboratory and industrial adsorbent columns^[66]. The near-wall channeling phenomenon, its effect on re-

ducing plug flow-like behavior, and consequently, adverse impact on separation efficiency was observed. Lab-scale breakthrough curves were analyzed by comparing the height equivalent to a theoretical plate (HETP). Regardless of the type of the adsorption isotherm, it was found that the HETP for a given simulation achieved a maximum for a particular column diameter, which could be attributed to the counter-balancing of near-wall channeling (which induces axial-dispersion) and radial dispersion effects. Industrial scale simulations shed light on axial dispersion and flow perturbation inside the columns owing to the presence of trays, distributors, pipes, and beams. They demonstrated that industrial-scale column hydrodynamics significantly impacted the adsorption yield, buttressing the relevance of CFD-based research for the optimal design of internals in large-scale adsorption systems and high Reynolds number fluid flow scenarios. A potential area of improvement to [Augier et al.](#)'s model could be to implement a non-isothermal process condition and implement temperature-dependent heat transfer coefficients in the solid-fluid mass transfer rate model. Adsorption is inherently non-isothermal (often exothermic), and local temperatures and pressures must be accounted for throughout the domain.

[Tomas and Karel](#) performed TSA-based Carbon dioxide adsorption on activated carbon pellets^[67]. The Dubinin-Astakhov (D-A) isotherm model and the linear driving force (LDF) kinetic model were implemented in the work. The results were obtained numerically via CFD simulations on OpenFOAM and were in good agreement with experiments.

[Breault et al.](#) used Barracuda, an Euler-Lagrangian CFD simulation tool to study CO_2 adsorption in a circulating fluidized bed^[68]. The authors could reproduce breakthrough composition curves with reasonable accuracy, and the fluid-particle model allowed to observe channeling and segregation. However, this approach was bottlenecked by slow computational rates, with only about 30s of real-time data simulated per day, translating into weeks per single run.

[Subraveti et al.](#) formulated a 2D axisymmetric CFD model on the commercial solver ANSYS Fluent v16.2 to study solute propagation in supercritical fluid chromatographic (SFC) columns^[69]. The model, supplemented with UDFs, investigated the effects of viscous fingering and plug effect on pulse injection. The CFD model could predict critical phenomena not captured by classical equilibrium-dispersive models, such as delay in elution times due to

inlet pressure increase, peak fronting, and peak distortions. However, the model’s postulate of incompressible flow is a slight oversimplification and needs to be investigated for better modeling of solute dynamics in SFC.

Verbruggen *et al.* applied a CFD approach to determine the adsorption parameters of acetaldehyde, a volatile organic compound, to abate indoor air pollution^[70]. The Langmuir adsorption isotherm was enhanced by incorporating a chemical reaction mechanism, according to the Langmuir-Hinshelwood-Hougen-Watson (LHHW) framework. This allowed transient phenomena to be accounted for and for the intrinsic adsorption parameters to be extracted. Simulations were performed on the COMSOL Multiphysics[®] v4.4 commercial software package. The computational grid consisted of about 80,000 tetrahedral cells with local refinement near the walls. Laminar flow regime treatment proved to suffice and was coupled with the Darcy–Forchheimer equation to model velocity and pressure fields. The adsorption/desorption parameters were obtained through an optimization performed by minimizing the mean-square error in time-varying CFD outlet concentration and experimental data. CFD results and validation could thus provide acetaldehyde adsorption parameters with high accuracy for further photocatalytic kinetic analysis. This technique may then be applied more widely to reactive adsorption systems.

Esposito *et al.* modeled and simulated an ammonia adsorption process with CFD via COMSOL Multiphysics[®] v5.6^[71]. The study investigated ammonia adsorption on a doped activated carbon in an industrial air purification box. In-house experiments were undertaken to validate the intricate modeling of the hydrodynamic and adsorption processes occurring in the system. The radial intra-particle mass transfer was attributed to Fickian diffusion to predict the experimental data efficiently. The Toth adsorption equilibrium isotherm and linear driving force kinetics were considered for mass balance closure. The symmetry in the geometry of the ventilator was exploited to reduce domain size and, therefore, computational times. Grid independency was established by comparing results using meshes of two different qualities, each having more than a million elements. Model prediction performance was assessed via mean-square error and the Pearson correlation coefficient statistical criteria available in the COMSOL optimization tool. A particular suggestion for future model improvement called for a comprehensive feed flow rate and inlet concentration sensitivity

study.

Qasem and Ben-Mansour developed a rigorous Pressure-Vacuum Swing Adsorption (PVSA) CFD framework to study CO_2 separation from a flue gas mixture using Mg-MOF-74^[72]. Four User-defined functions (UDFs) and seven User-defined scalars (UDSs) were integrated with transport equations for the species concentrations, gas temperature, bed temperature, and mass transfer to the adsorbent. A five-step PVSA cycle was developed in 2 and 3 dimensions using the FLUENT CFD package compiled with user-defined functions and validated against peer-reviewed PSA experimental works^[73]. They tuned the blowdown and evacuation times in attempts to improve the PVSA process and published the KPIs of an adsorption process, namely CO_2 purity and recovery, bed productivity, and cycle energy consumption. 3D simulation results were almost similar to that from 2D simulations, and it was therefore postulated that 2D modeling could be sufficient for most scenarios (i.e., chosen geometries). They could demonstrate achieving the DOE CO_2 capture design standard targets of 95% recovery and 90% purity at a corresponding operating carbon capture cost of \$6.87 per ton_{CO_2} for a 500-MW post-combustion power plant. The calculated performance metrics seemed to be a significant enhancement in adsorption-based CO_2 separation compared to existing literature benchmarks. It was found that cycle power consumption rose on decreasing the adsorbent particle size, while PVSA performance dropped on increasing the column diameter. Similar to the work by Augier et al., constant values for the LDF mass transfer coefficient were taken, neglecting temperature dependence of considerable consequence (significant in cases of pronounced exothermic adsorption of the heavy product).

To date, the physics of the adsorption cycle technologies is an active area of research, only complemented by refinements in CFD modules and developments in high-performance computing. Gautier et al. carried out a series of consequent studies^[74,75], the prior focusing on 3D CFD PSA model development and validation, and the latter delving into numerical sensitivity study of PSA cycle in an isotropic porous medium. Although studies have been simulating fluid flows and heat transfer in porous media, the dearth of existing literature on PSA separation process modeling undertaken at the microscopic scale is acknowledged. During model development, a 4-step PVSA cycle was considered for CO_2/CH_4 separation using carbon molecular sieves (CMS). They used a macroscopic scale approach, neglecting

intra-particle porosity, as a compromise between CFD–DEM approaches and incumbent 1D models. Experimental data was well-fitted to the Toth isotherm citing thermodynamic consistency, whereas the Langmuir isotherm proved to suffice in the 3-5 bar high-pressure range. The adsorption step of the PVSA cycle was deemed to terminate when the mol. fraction of the preferentially adsorbed product, CO₂, crossed 25 vol% at the outlet. 3D CFD simulations were performed on the CFD commercial software Star-CCM+[®]. The reader is referred to their work for detail on boundary conditions imposed during different stages of the PVSA cycle^[74]. Four mesh qualities ranging from about 7000 to 54,000 cells were tested, each with five thin prismatic layers at the wall-fluid interface for near-wall resolution. The pressure drop was expressed by the Darcy-Forchheimer equation and included in the penalizing source term of the 3D Navier-Stokes equation. The initial condition of the adsorbed phase in the current cycle is assumed to equal the gas-adsorbate equilibrium loading at the end of a previous PSA cycle. The influence of the effective thermal conductivity, column dead volume, and choice of adsorption equilibrium model on simulation robustness and overall cycle performance is discussed in their sensitivity analysis work. The authors do acknowledge a shortcoming in their approach in the way the mass transfer kinetics is modeled by the use of constant mass transfer coefficients. Either temperature-dependent LDF coefficients or a non-linear driving force (NLDF) model is suggested as a plausible improvement. Also, low-pressure isotherm measurements are recommended to ascertain the validity of the gas-adsorbate equilibrium assumption between cycles.

Flow transition

In CFD simulations, it is imperative to recognize the flow regime while applying a viscosity (i.e., laminar or turbulent) model. In numerous flow conditions, the transition from laminar to turbulent flow as the flow rate increases is abrupt, such as when the Reynolds number, based on the tube diameter, is 2100 in an empty tube. However, the transition from laminar to turbulent flow in a fixed bed is convoluted, progressing over a range of Reynolds numbers depending on the packing shape and configuration.

Through flow visualization and mass transfer experiments, Jolls and Hanratty^[76] observed flow transition from steady to unsteady for particle Reynolds number, $Re_p \in (110, 150)$.

Dybbs and Edwards^[77] performed laser Doppler velocimetry and flow visualization experiments of the flow of water and oils in beds packed with plexiglass spheres. They concluded that there existed four distinct regimes, shown below:

Table 1.2: Flow transition regimes in packed beds^[77]

Re_p	Flow Regime
$Re_p < 1$	Viscous or creeping flow
$5 < Re_p < 60$	Steady Laminar
$60 < Re_p < 120$	Unsteady Laminar
$Re_p > 120$	Turbulent

Dye tracing is simple to perform and does not require intricate setups. While it allows for the identification and qualitative examination of different flow regimes, the deduction of the transition Re_p between regimes may not be precise and are subjective to the observer.

Latifi et al.^[78] pioneered the micro-electrode technique to investigate the hydrodynamics and momentum transfer at the wall of a packed bed reactor. The fluctuation of the mass transfer coefficient as a function of flow was observed. The $-5/3$ slope (Kolmogorov’s law) obtained for current fluctuation spectra for $Re_p > 330$ characterized the onset of a turbulent flow regime. In conjunction with observing the evolution of frictional stress, a subsequent signal analysis allowed the authors to conclude that flow becomes fully turbulent at $Re_p \approx 400$. Rode et al.^[79] conducted a similar experiment with electrochemical probes to measure the local velocity gradients and, consequently, the local shear rates. They found that the flow was highly non-homogeneous in space and that a manifestation of turbulence occurs in the range $Re_p \in (110, 150)$, characterized by chaotic, time-dependent flow. Several other authors believe this transition to occur between $Re_p \in (150, 300)$ ^[80]. Seguin et al.^[81] conducted electrochemical studies and have suggested that turbulence may not appear until $Re_p > 600$.

The use of the term ‘turbulent’ is open to further scrutiny. It is understood by some to mean unsteady flow that may still be laminar, whereas it is interpreted as classical turbulent flow by others, as stated by Bear^[80]. Hence, there is a dearth of agreement on the flow regimes and corresponding critical Reynolds numbers beyond the Darcy or the creeping flow regime. Several factors, including but not limited to pore-size distribution and internal surface roughness, are believed to influence this transition. This warrants a fresh look.

1.5 Objectives and Project Scope

The air separation industry is competitive, where clients would opt to deal with suppliers offering the most energy-efficient solutions for the desired product tonnage. This thesis aims to apply computational tools to comprehend better heat and mass transfer phenomena involved during cyclic air adsorption for oxygen concentration. The project is in collaboration with Professor Arvind Rajendran’s experimental group at the University of Alberta and an Alberta-based firm that fabricates PSA units catering to oxygen production for wastewater treatment, agriculture, and aquaculture sectors.

Chapter 1 introduced the reader to the fundamentals of adsorption principles and the transport equations involved. Developments in numerical methods and computational modeling, brought about by the race to capture atmospheric CO_2 , were briefly discussed. A case study in mathematical modeling of a CO_2 capture PVSA process was investigated to understand advancements in computational solvers and gain insights from optimized results. These insights should enable adaptation to other binary systems of mixtures, such as oxygen concentration from air or helium enrichment from depleted natural gas reserves.

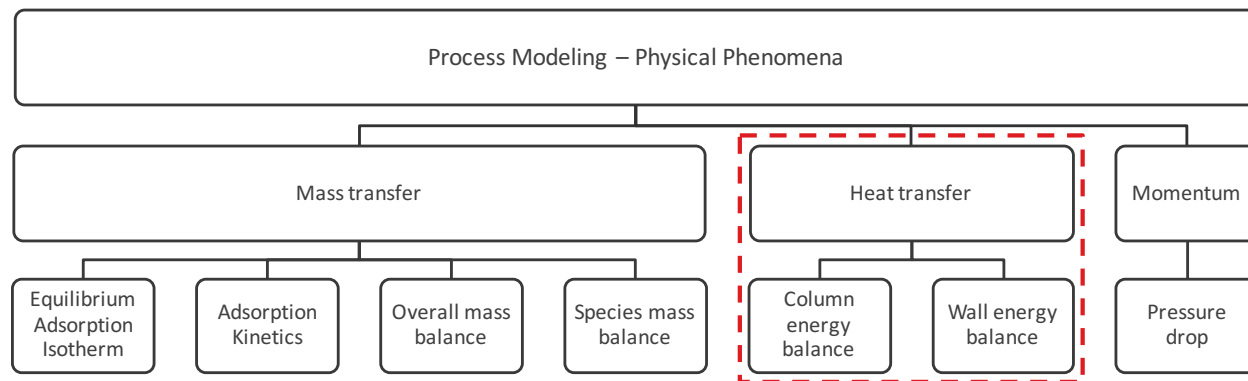


Figure 1.5: Focus of the thesis

The fluid-wall heat transfer coefficient is currently obtained experimentally and is fitted via optimization to match the thermal breakthrough profiles of the system (Ward and Pini^[82], Wilkins et al.^[38]). This limits the range of applicability. Chapter 2 shall investigate the fluid-wall heat transfer in fixed beds, primarily from the aspect of wall Nusselt number determination via particle-resolved CFD (PRCFD) simulations and comparing vis-à-vis various

correlations in literature. A fixed bed is generated using the gravity sedimentation-assisted discrete element method (DEM). Steady-state, three-dimensional coupled flow and heat CFD simulations are conducted to investigate fluid-wall heat transfer. Additionally, the effect of buoyancy-driven flows on the wall heat transfer number is explored. This CFD–DEM investigation is touted as a "serial by simplification" multi-scale modeling approach, whereby the correlations developed on a 3D representative geometry may be employed in 1D adsorber models. Finally, mathematical models to predict the adsorption system may thus be employed in a complementary fashion to experimental investigations as screening tools.

The main objective of Chapter 3 is to validate boundary conditions for a hot object cooled down in a cold environment due to natural convection. We model the cooling of hot water in a cup via CFD simulations and conduct lab-scale experiments for validation purposes. User-Defined Functions, or UDFs, are developed and compiled within Fluent to expand the solver's capabilities. Additionally, three-dimensional Large Eddy Simulations shall be briefly explored. Thus, a UDF module capable of simulating the combined effects of natural convection, radiation, and evaporative cooling has been developed. To date, CFD solvers do not yet possess natively the option to apply the natural convection or evaporative boundary conditions. This validated UDF may be ported for fixed beds and adsorption columns for improved prediction of thermal profiles in both lab-scale and industrial units.

Chapter 4 deals with 2D transient CFD-based adsorption Dynamic Column Breakthrough simulations. The concept of thermal resistance is incorporated to determine the convective and radiative heat transfer coefficients via physics-based modeling, thereby eliminating the need to fit these coefficients to a particular system. The development of temperature profiles along the bed is analyzed. Our CFD model is validated against published experimental results for a small-scale pilot unit (Wilkins and Rajendran^[57]). Spatial insights unlocked by multidimensional simulations such as field temperature and composition contour visualization, radial temperature distribution analyses, and wall-ambient heat transfer coefficient prediction shall be discussed. The success of this simulation would form the framework for cyclic PSA CFD simulations.

Chapter 5 summarizes the CFD angle to adsorption in fixed beds, laying down conclusions and possible future work.

Chapter 2

Convective heat transfer coefficient for the side-wall in a fixed bed^{*}

Fixed beds are widely used in the chemical and process industry due to their relatively simple yet effective performance. Determining the radial heat transfer at the wall in a fixed bed is crucial to predict the performance of columns. Heat transfer parameters often need to be obtained experimentally. Various Nusselt Nu_w versus Reynolds Re_p correlations in literature show considerable scatter and discrepancies. The tube-to-particle diameter ratio $\frac{D_t}{D_p}$ and boundary conditions on the particle surface have been understood to affect heat transfer near the wall by virtue of influence on the near-wall porosity and mixing. In this work, a fixed bed consisting of mono-disperse particles is generated via gravity-forced sedimentation modelling utilizing the discrete element method for a $\frac{D_t}{D_p}$ ratio of 3.3. The system is meshed and imported in a computational fluid dynamics (CFD) solver. Fluid inlet velocity is varied to get $Re_p \in [1, 1500]$ corresponding to the laminar and turbulent flow regimes. The particles are treated as boundaries with Dirichlet, Neumann, and Robin boundary conditions applied for the closure of energy balance. Another set of simulations is run with particles modelled as solids with varying thermal conductivities (k_s/k_f). The heat flux and volume-averaged fluid temperature calculated during post-processing are used to determine the wall heat transfer coefficient and, subsequently, the wall Nu number. Fifteen Nu_w versus Re_p correlations are

^{*}This chapter is a facsimile of the research article published in the Canadian Journal of Chemical Engineering [C. Baliga, P. Nikrityuk, Can. J. Chem. Eng. 2023](#)

compiled and analyzed. A new semi-empirical correlation for the wall Nusselt number has been developed for a fixed bed packed with monodisperse spheres for $\frac{D_t}{D_p} = 3.3$ and results compared with data published in literature. Additionally, the impact of buoyancy effect on the wall Nusselt number has been studied.

Keywords: fixed bed, fluid–wall heat transfer, Nusselt number, adsorption, CFD, particle-resolved CFD

2.1 Introduction

Fixed beds are widely used in the chemical and process industry due to their simple yet effective performance. They find applications in heterogeneous catalysis (e.g., dry reforming of methane, methanol synthesis, etc.) and in adsorption (CO₂ capture, oxygen separation, helium purification).^[83] However, some drawbacks of fixed beds include but are not limited to intricacies in temperature control and the occurrence of temperature gradients. It has been widely acknowledged that the accurate prediction of temperature profiles within the fixed bed and at the wall is crucial to estimate conversion in a reactor or cyclic performance of an adsorption column.^[84]

Referring to industrial pressure-swing adsorption (PSA) systems as multi-bed configurations where gas components are continuously separated in fixed beds, the radial thermal gradients are crucial parameters defining the efficiency of the whole system. PSA cycle productivity is curtailed on account of in situ temperature spikes induced during the exothermic adsorption step.^[85,86] The randomness of the adsorbent material packing and the inlet flow distributor cause further agitation of the feed, leading to flow asymmetries within the bed. Preventing hotspots and thermal runaways is imperative to augment bed thermal performance. High-performance computing-driven multi-dimensional computational fluid dynamics (CFD) simulations enable the exploration of the hydrodynamics of the system. Additionally, insights from thermal imaging may aid in the design of bed configurations adept at rapid fluid–wall heat exchange that can be modelled using the so-called wall Nusselt number.

The wall Nusselt number, Nu_w , is often expressed in terms of the particle Reynolds number, Re_p , to relate system heat transfer properties with system flow characteristics.

Typically, Re_p is based on the superficial velocity, that is, the velocity of the fluid (air) at the inlet of the bed.^[64]

$$Re_p = \frac{\rho_f u_\infty D_p}{\mu_f}; \quad Nu_w = \frac{h_w D_p}{k_f} \quad (2.1)$$

Often, Nu_w versus Re_p correlations have been reported in any of the following forms:

$$Nu_w = A \cdot Re_p^B; \quad Nu_w = C + A \cdot Re_p; \quad Nu_w = C + A \cdot Re_p^B \quad (2.2)$$

While numerous experimental studies report wall Nu_w solely as a function Re_p , other correlations have been developed along the years incorporating other parameters such as D_t/D_p , the tube's aspect ratio, L_t/D_t particle, or fluid conductivities. Most experiments were conducted with air as the fluid.^[87,88] Thus, the fluid Prandtl number, Pr , may be accounted for within the coefficient A . (The reader is referred to Table 2.1.)

The tube-to-particle diameter ratio, D_t/D_p , has been understood to affect heat transfer near the wall by virtue of influence on the near-wall porosity and mixing.^[64] Close to the wall, the *local* void fraction approaches unity. The surge in fluid velocity increases the resistance to heat transfer, which must be accounted for by employing a lumped heat transfer coefficient.

The effect of low D_t/D_p ratios on both heat and mass transfer has been observed not only in the laboratory setting but also in multitubular fixed bed heterogeneous catalytic reactors undergoing significant thermal gradients.^[65,103] A lower limit on the catalyst/adsorbent size to mitigate pressure drop (and thereby compression costs) counterbalances with the upper limit on the tubular diameter to ensure effective heat transfer, presenting low D_t/D_p systems. The tube wall plays a crucial role in heat transfer, reaction rates, conversion, and selectivity in these reactor tubes, making them challenging to model accurately. Dixon et al. reviewed several modelling works with low D_t/D_p geometries and the challenges involved in the application of CFD modelling to such systems.^[103] Prior works^[104–107] have demonstrated that the forced convection wall–fluid heat transfer rate in a packed tube with a low D_t/D_p ratio ranged from 3 – 10 times higher than that of an empty duct. Dixon has demonstrated that the wall effects tend to become irrelevant for $D_t/D_p > 15$.^[108,109]

Conducting mass transfer experiments eliminates the contribution of the solid phase to overall mass transfer in the fixed bed. Storck and Coeuret reviewed and summarized results

Table 2.1: Wall Nusselt number, Nu_w , versus particle Reynolds number, Re_p , correlations available across literature.

Number	Author(s)	Year	Nu_w Correlation	Re_p Validity	D_t/D_p Validity	Ref
1	Leva	1947	$0.813 \cdot \frac{D_p}{D_t} \cdot \exp\left(-6\frac{D_p}{D_t}\right) \cdot Re_p^{0.9}$	$250 < Re_p < 3000$	$3.3 < \frac{D_t}{D_p} < 20$	[89]
2	Leva et al.	1948	$3.5 \cdot \frac{D_p}{D_t} \cdot \exp\left(-4.6\frac{D_p}{D_t}\right) \cdot Re_p^{0.7}$	$250 < Re_p < 3000$	$3.7 < \frac{D_t}{D_p} < 12.5$	[90]
3	Chu and Storrow	1952	$0.134 \cdot \left(\frac{D_p}{D_t}\right)^{-0.13} \left(\frac{L_t}{D_t}\right)^{-0.9} Re_p^{1.17}$	$Re_p < 1600$	$3.9 < \frac{D_t}{D_p} < 25.7$	[91]
4	Yagi and Wakao	1959	$\begin{cases} 0.6 \cdot Re_p^{0.5}, & \text{for } Re_p < 40 \\ 0.2 \cdot Re_p^{0.8}, & \text{for } Re_p > 40 \end{cases}$	$20 < Re_p < 2000$	$6 < \frac{D_t}{D_p} < 47$	[92]
5	Kunii et al.	1968	$0.24 \cdot Pr^{\frac{1}{3}} \cdot Re_p^{0.75}$	$Re_p > 100$	$3.3 < \frac{D_t}{D_p} < 5$	[93]
6	Olbrich and Potter	1972	$8.9 \cdot Pr^{\frac{1}{3}} \cdot Re_p^{0.34}$	$100 < Re_p < 3000$	$4.06 < \frac{D_t}{D_p} < 26.6$	[94]
7	Li and Finlayson	1977	$0.17 \cdot Re_p^{0.79}$	$20 < Re_p < 7600$	$3.3 < \frac{D_t}{D_p} < 20$	[95]
8	Specchia et al.	1980	$2\varepsilon_w + 0.0835 \cdot Re_p^{0.91}$	$10 < Re_p < 1200$	$3.5 < \frac{D_t}{D_p} < 8.4$	[96]
9	Colledge and Paterson	1984	$0.523 \cdot \left(1 - \frac{D_p}{D_t}\right) \cdot Pr^{\frac{1}{3}} \cdot Re_p^{0.738}$	N/A	N/A	[97]
10	Dixon et al.	1984	$\left(1 - 1.5\left(\frac{D_p}{D_t}\right)^{1.5}\right) \cdot Pr^{\frac{1}{3}} \cdot Re_p^{0.59}$	$50 < Re_p < 500$	$3 < \frac{D_t}{D_p} < 12$	[98]
11	Peters et al.	1988	$4.9 \cdot \left(\frac{D_p}{D_t}\right)^{0.26} \cdot Pr^{\frac{1}{3}} \cdot Re_p^{0.45}$	$200 < Re_p < 8000$	$3 < \frac{D_t}{D_p} < 11$	[99]
12	Martin and Nilles	1993	$\left(1.3 + 5\frac{D_p}{D_t}\right) \frac{k_{e,r}}{k_f} + 0.19Pr^{\frac{1}{3}} \cdot Re_p^{0.75}$	$35 < Re_p < 500$	$5 < \frac{D_t}{D_p} < 12$	[100]
13	Demirel et al.	2000	$0.047 \cdot Re_p^{0.927}$	$200 < Re_p < 1450$	$4.5 < \frac{D_t}{D_p} < 7.5$	[101]
14	Laguerre et al.	2006	$1.56 \cdot Pr^{\frac{1}{3}} \cdot Re_p^{0.42}$	$100 < Re_p < 400$	$\frac{D_t}{D_p} = 5$	[102]
15	Das et al.	2017	$1.351 + 0.1124 \cdot Pr^{\frac{1}{3}} \cdot Re_p^{0.878}$	$1 < Re_p < 500$	$4 < \frac{D_t}{D_p} < 8$	[64]

from several electrochemical studies conducted to study mass transfer in fixed beds.^[110] Dixon et al.^[98] theorized that the heat-mass analogies could be advantageously utilized to determine heat transfer parameters.

Yet, there has widely been no consensus on the order of magnitude of wall–fluid heat transfer coefficient, h_w , specifically at low to moderate Reynolds number flows.^[88,111–114] Experimental data by Hennecke and Schlünder were compiled with 14 other works and showed a significant scatter in Nu_w determination at $Re_p < 400$.^[111] Large molecular Peclet number, Pe , (and, correspondingly, high Re_p [$Pe = Re_p \cdot Pr$]) flows, however, show a relatively good agreement among experiments.

One of the ways to define the heat transfer coefficient between fixed bed wall and the gas flow inside the bed is the so-called particle-resolved CFD (PRCFD) numerical simulations, which can be made using the finite volume method^[64,115] or finite element method.^[116] For the review of different CFD modelling approaches and applications referring to PRCFD applications in chemical engineering, we refer to the reviews of Deen et al. and Golshan et al.^[117,118] There have been numerous studies, both experimental^[89,90,92,101,112,119] and computational^[63–65], conducted to determine and validate the wall heat transfer coefficient for fixed beds with spherical particles. Table 2.1 shows existing Nu_w relations obtained experimentally and numerically. This table will be analyzed in the results section.

For example, Tabib et al.^[63] applied the CFD–DEM technique to assist in the design of industrial reactors packed with various pellet shapes. The computationally-prohibitive nature of simulating industrial scale reactors ($D_t/D_p > 40$) due to meshing constraints is recognized. A cylindrical cut segment and a wall segment of a DEM-generated packed bed were considered to represent the central and near-wall regions of the bed, respectively. The realizable $k - \varepsilon$ turbulence model with standard wall function treatment was used. The procedure to calculate the wall heat transfer coefficient is similar to our approach (Equations 2.16 and 2.17). However, the cut segment representing the reactor core overpredicted the wall heat transfer coefficient, h_w , by roughly 60%. This was attributed to the slip boundary conditions applied on the segment walls.

A summary of previous CFD modelling studies of hydrodynamics and heat transfer in packed beds for different values of the column-to-particle diameter ratios (in the range from

4 to 12) and Re_p (in the range from 1 to 500) has been introduced in the work of Das et al.^[64] In particular, Prof. Kuipers's group^[64] conducted a fully resolved direct numerical simulation (DNS) study for slender packed bed reactors with varying numbers of particles (in the range from 220 to 3700). The local wall-to-bed heat transfer coefficient was calculated at each cross-section of the column using $\Delta T = T_w - T_{cup-aver}$, where $T_{cup-aver}$ is the flow-averaged temperature of the fluid at each section of the fixed bed. The overall wall-to-bed convective heat transfer coefficient was calculated using the logarithmic mean temperature difference ΔT_{LMTD} , widely used in the heat exchanger theory. It was shown that the wall Nusselt number, $Nu_w = 1.351 + 0.1124Re_p^{0.878}Pr^{1/3}$, obtained numerically is close to the empirical correlation by Yagi and Wakao^[92] with $\pm 10\%$ discrepancy.

To investigate the heat transfer between gas flow and side wall in fixed beds for higher values of the particle Reynolds numbers ($Re_p > 500$), researchers used RANS turbulence models. A full review of existing work is out of the scope of this work. Next, we introduce only a few of them.

For example, Guardo et al.^[61,62] performed PRCFD calculations to investigate flow and heat transfer in low D_t/D_p non-regularly packed fixed beds and benchmarked turbulence models in an extended study, respectively. Contemporarily, the $k - \omega$ -shear stress transport (SST) model has gained popularity over other turbulence models due to its robustness and good agreement with experimental data in a wide range of applications.

Recently, Prof. Wehinger's group^[120] studied experimentally and numerically (PRCFD) the radial heat transport in a fixed bed reactor made of metallic foam pellets. In particular, the authors calculated the effective radial thermal conductivity of the bed and the apparent wall-fluid heat transfer coefficient. However, it should be noted that the authors used the analytical solution of a 2D pseudo-homogenous plug-flow reactor model in the form of a 2D, steady-state heat transport partial differential equation (PDE) with the Robin boundary condition formulated for the mixture (solid-fluid) to define heat transfer parameters. Thus, this Nu_w can be used only for the so-called mixture-based or continuum models and not for particle-unresolved Euler-Lagrange based models.^[121]

Based on the analysis of works published, investigations devoted to studies of the impact of different boundary conditions on the particle surface on the wall Nusselt number are

rare. Moreover, to the best of our knowledge, the influence of buoyancy effects has not been reported so far. Motivated by this fact, our work investigates the complete domain of the packed bed employing different boundary conditions on the particle surface and comparing results with simulations using the conjugate heat transfer model. The present work is organized as follows. Section 2.2 provides an overview of the problem of research. In Section 2.3, a detailed description of the computational model is provided. Results are discussed in 2.4, supported with experimental data for validation purposes. Finally, the conclusions from this work are summarized in Section 2.5.

2.2 Problem description

In this work, the computational domain consists of 374 spherical particles whose coordinates have been calculated using open-source DEM software YADE^[122]. The validation of this software and the mechanical properties of particles used in DEM simulations can be found in the work of Lu and Nikrityuk.^[123] It should be noted that, to simplify the mesh generation, we used the so-called gaps.^[124,125] Gaps were obtained by shrinking the spheres, producing gap size between spheres below $0.01D_p$. The choice of $D_t/D_p = 3.3$ is explained by a compromise between computational costs and accuracy of results. The problem is that increase of D_t/D_p leads to a significant increase in the number of particles in the bed. The primary motivation of the geometry chosen is to illustrate the influence of different boundary conditions on the particle surface and to show the deviation from the conjugate heat transfer case when solid particles are incorporated into the mesh.

Figure 2.1A shows a schematic presentation of the whole domain, divided into 3 cell zones. In particular, an outflow zone is added in order to get a steady-state and stable converged solution. It should be noted that without the outflow zone, it was impossible to get a converged solution. An inflow zone is added in order to get a more realistic inflow condition in the inlet zone of the fixed bed. Along the inflow and outflow zones, the side wall is kept insulated. The outflow zone is about 2.5 times as long as the inlet zone, in line with best practices. The middle section contains the packed bed with the spheres, and the wall is kept isothermal. Here, the fluid bulk temperature and the wall heat flux are recorded.

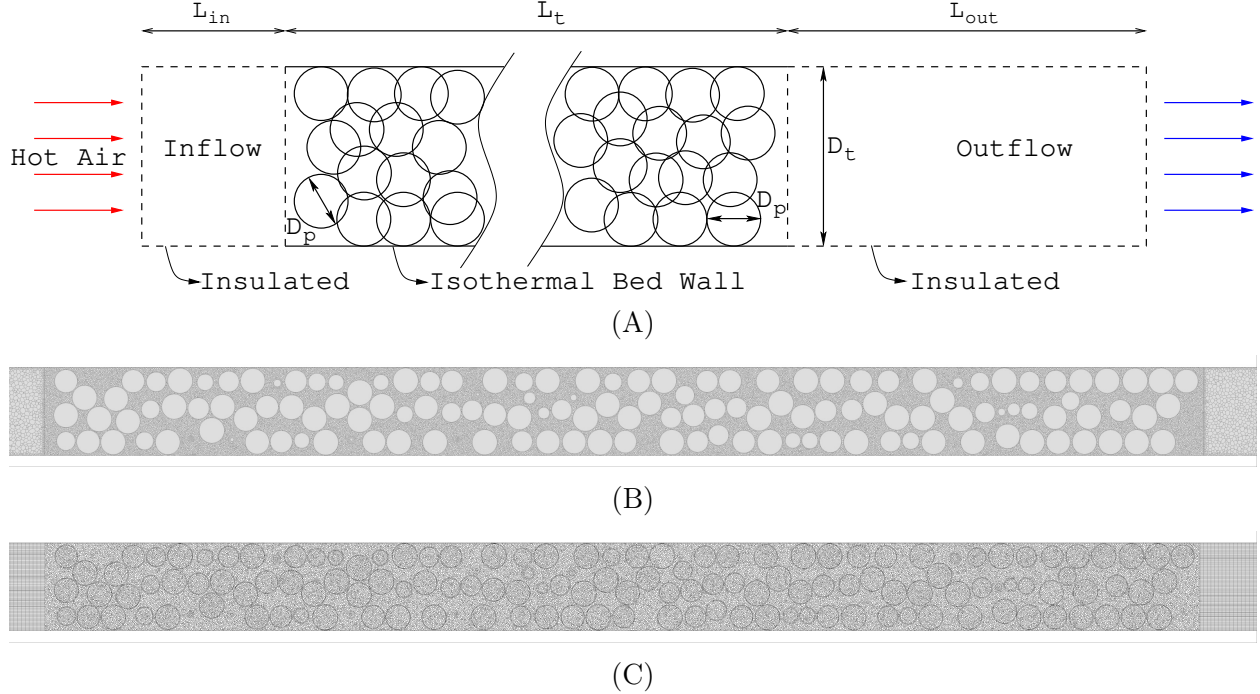


Figure 2.1: Schematic and CFD geometry: (A) Simplified schematic of the fixed bed simulation; (B) Slice of a fixed bed packed with monodisperse particles containing hollow solid mesh elements; and (C) Slice of a fixed bed packed with monodisperse particles containing internal solid mesh elements.

The characteristics of the system, including the bed geometry, number of particles, and the calculated bulk porosity, are mentioned in Table 2.2.

Table 2.2: Packed bed characteristics.

Parameter	Symbol	Value
Fixed bed (tube) length	L_t	132 mm
Inflow length	L_{in}	20 mm
Outflow length	L_{out}	50 mm
Tube diameter	D_t	10 mm
Particle diameter	D_p	3 mm
Number of particles	N_p	374
Bed porosity	ε_b	0.49

The bulk bed porosity, ε_b , is calculated as follows:

$$\varepsilon_b = 1 - \frac{N_p \cdot \frac{1}{6}\pi D_p^3}{\frac{1}{4}\pi D_t^2 L_t} \quad (2.3)$$

The values of the thermodynamic properties—density, specific heat, thermal conductivity,

and viscosity—are considered constant and are given in Table 2.3.

Table 2.3: 3D CFD system material properties.

Parameter	Air	Aluminum
Density ρ , $\frac{kg}{m^3}$	1.225	2719
Specific heat C_p , $\frac{J}{kg \cdot K}$	1006.43	871
Thermal conductivity k , $\frac{W}{m \cdot K}$	0.0242	202.4
Viscosity μ , $\frac{kg}{m \cdot s}$	1.7894×10^{-5}	-

2.3 Computational model

Before we present the mathematical model, the following assumptions are introduced:

1. All transport properties of the gas and particles are constant.
2. The gas flow is treated as incompressible.
3. Buoyancy effects are neglected.
4. Radiative heat transfer is neglected.
5. Roughness of particles is neglected.

Table 2.4 lists the models used in the simulation along with the numerical discretization schemes. We perform steady-state simulations with the pressure-based solver since the density of the gas is not considered temperature-dependent. The Semi-Implicit Method for Pressure Linked Equations (SIMPLE)^[126] scheme is used for pressure-velocity coupling.

Table 2.4: List of models and schemes^[127] used in the CFD model.

<i>Name</i>	<i>Model/Scheme name</i>
Solver	Steady state, pressure-based
Flow model(s)	Laminar & $k-\omega$ SST
Pressure-velocity coupling	SIMPLE ^[126]
Spatial discretization-gradient	Least squares cell-based
Spatial discretization-pressure	Second-order
Spatial discretization-all equations	Second-order upwind

Table 2.5 shows the Re_p range considered in this work and corresponding flow models. Where the laminar flow viscosity model is unable to achieve solution convergence, the Reynolds averaged Navier-Stokes (RANS) $k-\omega$ SST model is used in lieu.

Table 2.5: Reynolds numbers and corresponding flow models used in simulations.

Label	a)	b)	c)	d)	e)	f)	g)	h)	i)	j)
Re	1	10	20	50	100	150	200	500	1000	1500
Flow model	Laminar					RANS $k-\omega$ SST				

Justification of the use of RANS is shown in Table 2.6, which presents the values of the volume-averaged and maximum values of the turbulent viscosity ratio $\frac{\mu_t}{\mu}$. It can be seen that $Re_p = 150$ RANS produces $\frac{\mu_t^{max}}{\mu} \approx 1$.

Table 2.6: Turbulent viscosity ratio (TVR) versus Re_p .

‘Meshed’ solids $k_s/k_f = 1$		
	(μ_t/μ)	
Re_p	Vol. Avg	Max
150	0.001104	0.606163
200	0.002691	1.509141
500	0.133391	6.900930
1000	1.061219	16.236720
1500	2.078072	25.568640

Note: Vol. avg. and max correspond to fluid in the packed bed zone only

In this work, we utilize the default wall function condition that automatically blends between low-Re formulation and high-Re wall functions.^[128] Thus, our RANS simulations do not require Y^+ close to unity. Values of the side wall averaged Y^+ and particle surface averaged Y^+ calculated for $Re_p = 1500$ are 4.8 and 6.4, respectively.

Transport equations for the laminar flow and flow regime solved with the $k - \omega$ SST are given in Tables 2.7 and 2.8 respectively.

Table 2.7: Steady-state laminar flow model for the fixed bed.^[129]

<i>Name</i>	<i>Equation</i>
Continuity equation	$\nabla \cdot \vec{v} = 0$
Momentum equation	$\rho (\vec{v} \cdot \nabla) \vec{v} = -\nabla p + \nabla \cdot [\mu (\nabla \vec{v} + \nabla \vec{v}^T)]$
Energy equation	$\rho \nabla \cdot (C_p T \vec{v}) = \nabla \cdot (k_f \nabla T)$

Table 2.8: Steady-state RANS model: the shear-stress transport (SST) $k - \omega$ model.^[128,130] Here, the cross-diffusion term D_ω , constants, and blending functions for the SST model are not provided; they may be found in the work of Menter and from ANSYS.^[128,130]

<i>Name</i>	<i>Equation</i>
Continuity equation	$\nabla \cdot (\vec{v}) = 0$
Momentum equation	$\rho (\vec{v} \cdot \nabla) \vec{v} = -\nabla p + \nabla \cdot [\mu_{ef} (\nabla \vec{v} + \nabla \vec{v}^T)]$
Energy equation	$\rho \nabla \cdot (C_p T \vec{v}) = \nabla \cdot (k_{ef} \nabla T)$
The SST $k - \omega$ model equations	$\rho \nabla \cdot (k \vec{v}) = \nabla \cdot \left(\left(\mu + \frac{\mu_t}{\sigma_k} \right) \nabla k \right) + \mu_t \mathbf{S}^2 - \rho \beta^* k \omega$ $\rho \nabla \cdot (\omega \vec{v}) = \nabla \cdot \left(\left(\mu + \frac{\mu_t}{\sigma_\omega} \right) \nabla \omega \right) + \alpha \alpha^* \rho \mathbf{S}^2 - \rho \beta^* \omega^2 + D_\omega$ <p>where, $k_{ef} = k_f + \frac{C_p}{Pr_t} \mu_t$, $\mu_{ef} = \mu + \mu_t$</p> $\mu_t = \rho \frac{k}{\omega} \frac{1}{\max \left[\frac{1}{\alpha^*}, \frac{\mathbf{S} F_2}{\alpha_1 \omega} \right]}$

\mathbf{S} is the strain rate magnitude

The mesh size of the full bed was initially reduced by excluding the solid parts (the particle internals) from the mesh. This mesh may be referred to as the mesh with the particles modelled as walls. Mesh files of different quality levels were designed: (i) Coarse: 0.3 MM, (ii) Medium: 1.0 MM, and (iii) Fine 2.6 MM polyhedral cells. Details are shown in Table 2.9.

Table 2.9: Characteristics and control volume count for the three meshes with hollow particles.

Mesh	Quality	Tetrahedral CV count	Polyhedral CV count
Mesh 1	Coarse	717718	223244
Mesh 2	Medium	4621952	973166
Mesh 3	Fine	13437930	2662266

The full bed mesh generated, including all bed internals, may be referred to as the mesh with the particles modeled as solids. Two qualities of meshes were generated, namely (i) Fine: 2.1 MM and (ii) Fine 3.8 MM polyhedral cells, elaborated in Table 2.10.

Table 2.10: Characteristics and control volume count for the two meshes with solid CVs meshed.

Mesh	Tetrahedral CV count	Polyhedral CV count
Mesh S1	9,333,568	2,099,829
Mesh S2	17,945,029	3,830,255

The mesh files created initially contained tetrahedral cells that were later converted to polyhedral cells to reduce overall cell count by a factor of 4 – 5 times. The 2D slices of the meshes containing polyhedral CVs are shown in Figures 2.1B and 2.1C. Only the momentum profile may be eligible for comparison since the mesh with particles modelled as walls could not give comparable energy solutions, except for the limiting case of no heat transfer between the fluid (air) and the solids (equivalent boundary condition [BC] for Mesh I \rightarrow insulated wall \iff for Mesh II \rightarrow particles with negligible thermal conductivity $k_s \rightarrow 0$).

2.3.1 Boundary conditions

For the momentum conservation equation, the boundary condition at the inlet is directly defined as the feed velocity, whilst the outlet boundary condition is defined by type outflow:

$$v \Big|_{z=0} = v_{feed} = u_{\infty} \quad (2.4)$$

$$T \Big|_{z=0} = T_{feed} = 350 \text{ K} \quad (2.5)$$

As for the outlet, outflow boundary conditions apply.

At $r = R_t$, the no-slip condition is used for the momentum equation, and the isothermal wall boundary condition is set up to account for external heat transfer.

$$v \Big|_{r=R_t} = 0 \quad (2.6)$$

$$T \Big|_{r=R_t} = T_w = 300 \text{ K} \quad (2.7)$$

In order to investigate the influence of different boundary conditions on the heat transfer between gas in the side wall, we test the following boundary conditions on the particle surface:

1. Thermally insulated particles (Neumann BC):

$$-k_f \frac{\partial T}{\partial n} \Big|_{\text{particle surface}} = 0 \quad (2.8)$$

2. Convective heat transfer between the particle surface and gas flow (Robin BC):

$$-k_f \frac{\partial T}{\partial n} \Big|_{\text{particle surface}} = h_p (T_s - \langle T_{gas} \rangle); \quad h_p = \frac{Nu_p \cdot k_f}{D_p} \quad (2.9)$$

$$Nu_p = (7 - 10\varepsilon_b + 5\varepsilon_b^2)(1 + 0.7Re^{0.2}Pr^{1/3}) + (1.33 - 2.4\varepsilon_b + 1.2\varepsilon_b^2)Re_p^{0.7}Pr^{1/3} \quad (2.10)$$

Here, Nu_p refers to the Gunn correlation,^[131] and ε_b is calculated as per Equation 2.3. The free stream temperature for convection is defined as the volume-averaged fluid temperature $\langle T_{gas} \rangle$ in the packed bed zone, as per Equation (2.17).

3. Constant particle surface temperature (Dirichlet):

$$T_s = const = T_{feed} \quad (2.11)$$

The investigation of the influence of boundary conditions on Nu_w can be explained by different applications from engineering. For example, the Dirichlet boundary condition is

valid for heat storage fixed beds. It is well acknowledged that during phase change processes, the interface temperature of each capsule with phase change material (PCM) equals the melting temperature of PCM. The application of the Neumann boundary condition may be justified by cases when the thermal conductivity of solid particles is significantly less than fluid/gas thermal conductivity. For example, it can be the case in solid–liquid metal systems.

In the next phase of simulations, a new mesh was generated wherein the particles are now treated as solid elements within the Fluent solver. We vary the solid thermal conductivity, k_s , as a multiple of the fluid thermal conductivity, k_f . Five scenarios are considered: $\frac{k_s}{k_f} \in \{ \rightarrow 0, 0.1, 1, 10, 100 \}$. In either of the mesh types, a no-slip momentum boundary condition is applicable to the particles.

2.4 Results and discussion

Before we initiated CFD simulations with the conjugated heat transfer model, we carried out simulations without heat transfer inside particles using boundary conditions explained in Section 2.3.1. Finally, a comprehensive mesh was employed, treating the particles as 'true' solids. This enabled doing away with the need for a boundary condition on the particles but needed specifying a solid thermal conductivity parameter k_s . Five different k_s/k_f ratios were taken, and the wall Nusselt number Nu_w was obtained for a range of flow corresponding to $Re_p \in (1, 1500)$.

Hot air at 350 K is fed through the 'inlet' face. The temperature of the wall, T_w , encapsulating the packed bed is maintained at 300 K. The air inlet velocity was varied to modulate the Re_p as defined by Equation (2.1). The wall Nusselt number, Nu_w , for a given particle Reynolds number, Re_p , is then calculated once steady state has been reached as follows:

$$q''_w = h_w \cdot \Delta T \quad (2.12)$$

$$Nu_w = \frac{h_w \cdot D_p}{k_f} \quad (2.13)$$

$$Nu_w = \frac{q''_w \cdot D_p}{k_f \cdot \Delta T} \quad (2.14)$$

where

$$\Delta T = (T_b - T_w) \quad (2.15)$$

The wall heat flux, q_w'' , around the packed bed is measured using surface area averaging.

$$q_w'' = \frac{\int_S q_w'' dS}{\int_S dS} = \frac{\sum_{N_w} q_i'' \Delta S_i}{\sum_{N_w} \Delta S_i} \quad (2.16)$$

The bulk fluid temperature in the packed bed zone, T_b , is calculated using cell volume averaging similarly to the work of Tabib et al.^[63]

$$T_b = \frac{\int_V T dV}{\int_V dV} = \frac{\sum_{N_f} T_i \Delta V_i}{\sum_{N_f} \Delta V_i} = \langle T_{gas} \rangle \quad (2.17)$$

In this work, we did not use the logarithmic mean temperature difference ΔT_{LMTD} that was utilized in the work of Das et al.^[64] Das et al.^[64] used the following equations to calculate Nu_w as follows:

$$h_w = \frac{q_w''}{\Delta T_{LMTD}}; \quad Nu_w = \frac{h_w D_p}{k_f} \quad (2.18)$$

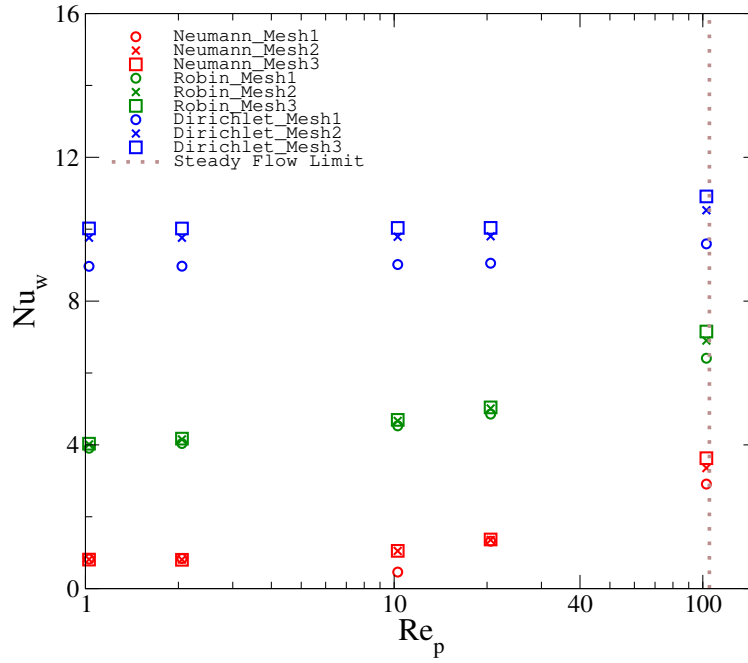
$$\Delta T_{LMTD} = \frac{\Delta T_{in} - \Delta T_{out}}{\ln\left(\frac{\Delta T_{in}}{\Delta T_{out}}\right)} \quad (2.19)$$

$$\Delta T_{in} = T_w - T_{in}; \quad \Delta T_{out} = T_w - T_{out} \quad (2.20)$$

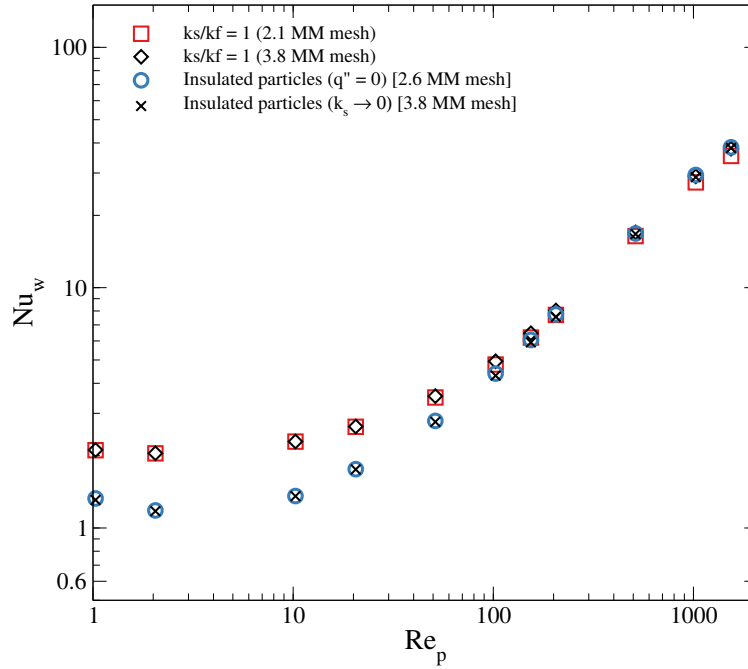
where T_w is the side-wall temperature and T_{in} and T_{out} are the inlet and outlet bulk temperatures referring to the fixed bed zone only. From the analysis of Equation (2.19), it may be seen that if $T_w \approx T_{out}$, which can happen if Re_p is small, the calculation of ΔT_{LMTD} can cause numerical problems. Thus, we use Equation (2.17) in this work.

Grid studies were performed for the hollow particle mesh. Three different BCs, namely, Neumann, Robin, and Dirichlet, were applied on the particle walls for three mesh qualities as per Table 2.9. The simulations were performed for various inlet velocities up to the laminar flow limit. Based on the grid study results, shown in Figure 2.2A, the highest quality hollow particle mesh (Mesh 3) was considered for further simulations.

Two mesh qualities were compared for the case when particles were modelled as solids with k_s/k_f ratio of 1. On the same plot, Figure 2.2B, the hollow and solid particle mesh types



(A)



(B)

Figure 2.2: Grid studies demonstrating mesh independence: (A) Grid study comparing Nu_w from various BCs (Dirichlet, Neumann, and Robin) applied on hollow particle meshes (Mesh1 - 0.3 MM, Mesh2 - 1.0 MM, Mesh3 - 2.6 MM); (B) Grid study comparing Nu_w between the hollow and meshed particle meshes for the case of insulated particles, and between two qualities of the meshed particle meshes for $k_s/k_f = 1$.

were compared for the case of insulated particles (Mesh 3 versus Mesh S2). Post-processing of the 3D contours and 2D slice visuals reinforced the results of the grid study.

Table 2.1 lists 15 correlations relating the Nu_w to the Re_p , tube geometry ($D_t/D_p, L_t/D_t$), near-wall porosity, ε_w , the fluid conductivity, k_f , and radial effective thermal conductivity $k_{e,r}$. Figure 2.3 depicts 7 correlations that could be represented by the form $Nu_w = f(Re_p, D_t/D_p)$. Correlations that incorporate porosity and conductivity are excluded from the plot due to system unknowns. From the plot, we may clearly notice that experimentally-obtained correlations are primarily valid for medium to high Re_p flows.

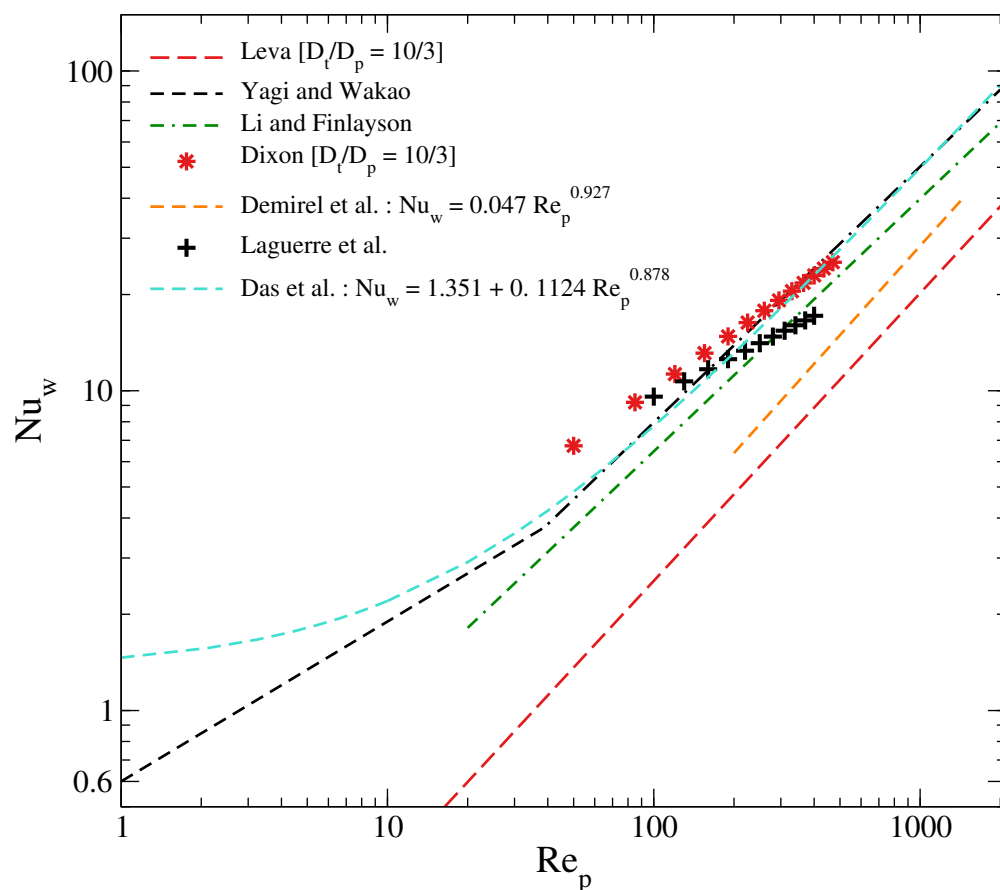


Figure 2.3: Correlations for Nu_w versus Re_p available across literature [$Nu_w = f(Re_p, D_t/D_p)$] (Legend refers to: Leva^[89], Yagi and Wakao^[92], Li and Finlayson^[95], Dixon et al.^[98], Demirel et al.^[101], Laguerre et al.^[102], and Das et al.^[64]).

3D particle temperature contours are visualized in Figures 2.4 and 2.5 for the Neumann and Robin boundary conditions, respectively. For the simulations performed with the Neu-

mann BC, we observe that the temperature propagates through the inner core of particles more predominantly as opposed to the near-wall particles. This is indicative of a $T(z, r, \theta)$ dependence. For creep flow, $Re_p \approx 1$, the particles surface temperature is not increased significantly, with most heat dissipation very close to the entrance. As Re_p increases to 50, about half the bed particles surface temperatures from the inlet are increased. At high Re_p flow, the particles surface temperature at the bed inlet reach inlet fluid temperature while the particles near the bed exit are heated up to 40% of the max temperature gradient, $(T_{feed} - T_w)$.

The evolution of the temperature contours for the Robin BC is, on the other hand, less susceptible to radial variance, indicative of a $T(z, \theta)$ dependence. This could be attributed to the nature of how the free stream temperature is defined as the bulk fluid temperature $\langle T_{gas} \rangle$. We see a gentle axial temperature gradient along the bed that increases with flow rate. None of the particles attain a temperature that is even close to that of the feed, and thus, thermal runaway is not expected to occur.

It is commonly acknowledged that heat transfer in the fixed bed occurs through two mechanisms: conduction, which involves the transfer of heat through the solid and fluid phases, and convective mixing. ^[64,88,96]

$$Nu_w = Nu_w^0 + Nu_w^f \quad (2.21)$$

where Nu_w^0 is the flow-independent (stagnant) contribution and Nu_w^f is the flow-dependent (mixing) contribution to heat transfer; the latter is more dominant at higher fluid velocities. In the creep flow regime, heat transfer is primarily through conduction, wherein Nu_w is independent of Re_p . However, it is tedious to quantify this stagnant contribution experimentally, leading this term to be generally neglected. This is an area where CFD may be employed advantageously to study heat transfer at low flow regimes. Correlation of the form 2.2c is considered to be more comprehensive of the three types listed above, accommodating both the stagnant and non-linear mixing contributions.

Figure 2.6 depicts results from our CFD simulations for various cases considering various boundary conditions on the particles when modelled as wall along with tweaking the k_s/k_f

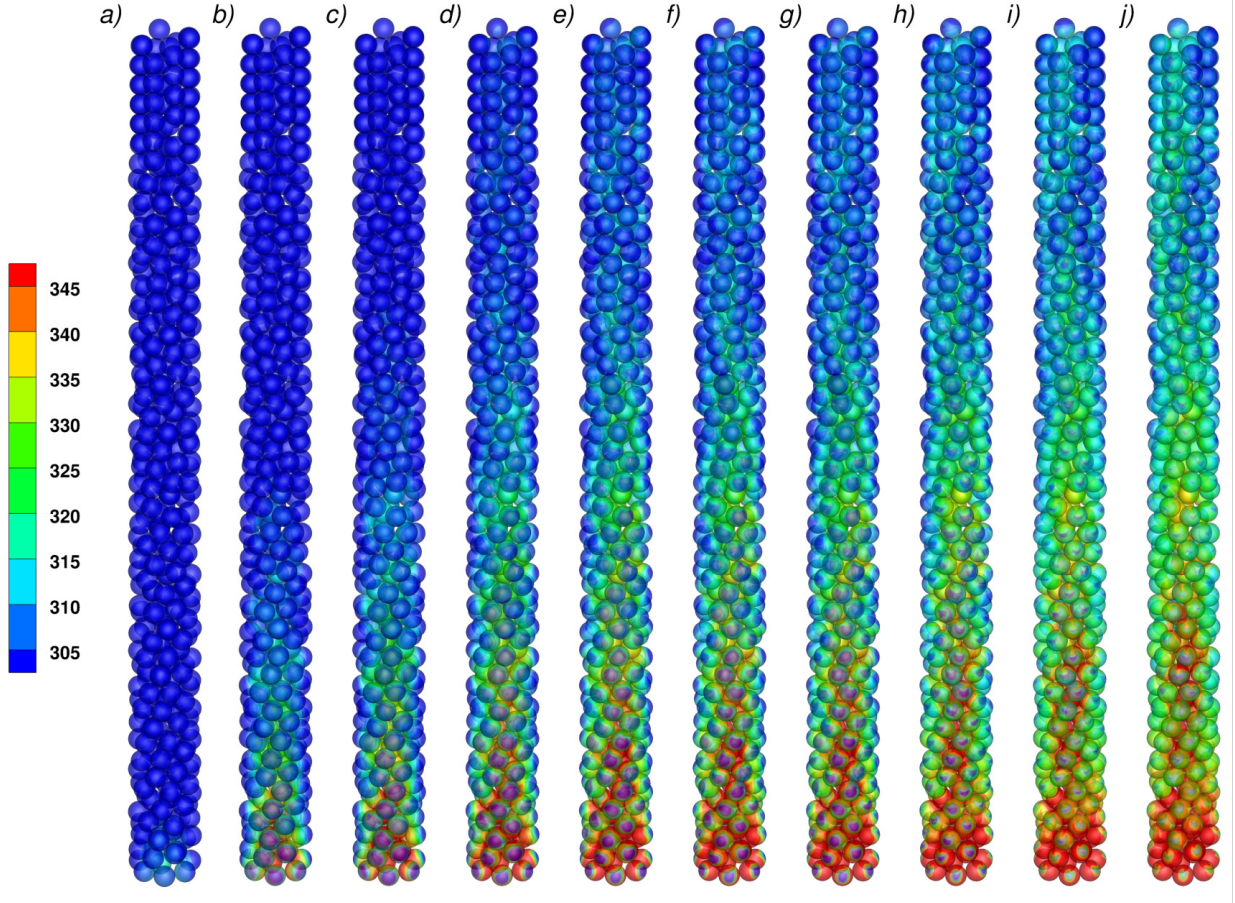


Figure 2.4: Particle surface temperature (T , K) contours subject to Neumann BC [a–j] correspond to Re_p following Table 2.5]

ratio for the mesh with ‘true’ solid particles. We observed that Nu_w vs Re_p dependency was certainly influenced by the solid thermal conductivity. Higher solid thermal conductivity led to increased heat transfer at the wall. Nu_w versus Re_p for various k_s/k_f were most dispersed for very low flow rates, were seen to converge with increasing flow rates, and even overlapped at high flow rates $Re_p \sim 1500$. This trend corroborates the behaviour of data compiled by Tsotsas and Schlünder.^[88] This effect is explained by the increasing the role of turbulence. Namely, for $Re_p \sim 1500$, the volume averaged (fixed bed zone) turbulent viscosity ratio is close to 2 and the maximum value is of about 26.

For insulated particles, the following correlation for fluid–wall heat transfer is proposed:

$$Nu_w = 1 + 0.054Re_p^{0.9} \quad (2.22)$$

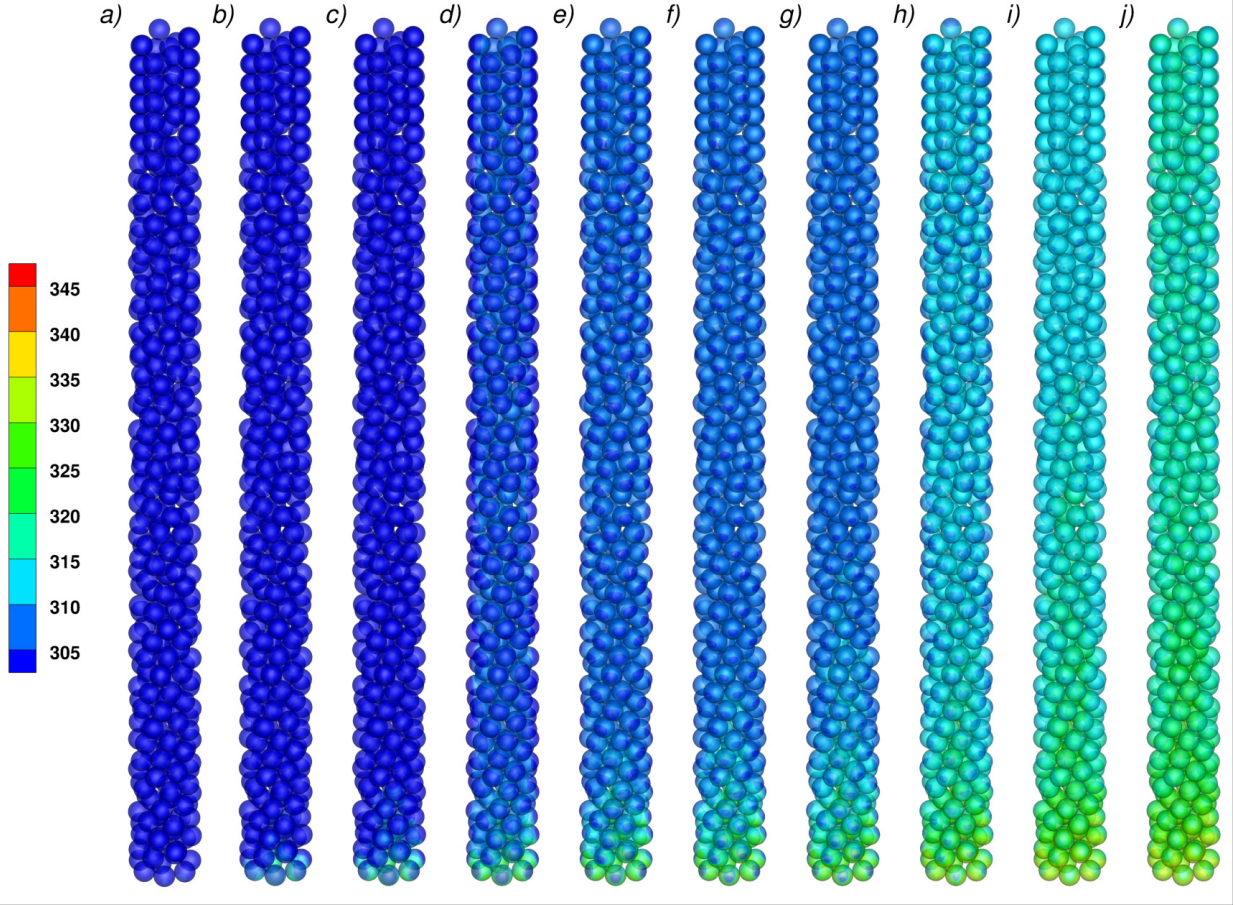


Figure 2.5: Particle surface temperature (T, K) contours subject to Robin BC [a–j correspond to Re_p following Table 2.5]

The Re_p exponent $B = 0.9$ agrees with the experimentally obtained range $B \in [0.75, 0.9]$ for moderate to high Re_p flows, and the constant 1 signifies the stagnant (conduction) contribution of the fluid phase to the overall fluid–wall heat transfer. Equation (2.22) is also plotted in Figure 2.6. At sufficiently high flows, Equation 2.22 is in excellent agreement with experimental data reported by Demirel et al.^[101]

It was seen that the laminar flow viscous model converged only up to Re_p of 100. This is in line with experimental observations^[76–79,81] that broadly predict the onset of fluctuations around $Re_p \in (110, 150)$.

Figure 2.7 outlays the 3D temperature contours of the solid particles for the five sets of simulations of k_s/k_f ratios $\in \{\rightarrow 0, 0.1, 1, 10, 100\}$. For a given solid conductivity, with increase in Re_p , we note the further propagation of the temperature front. For a given flow

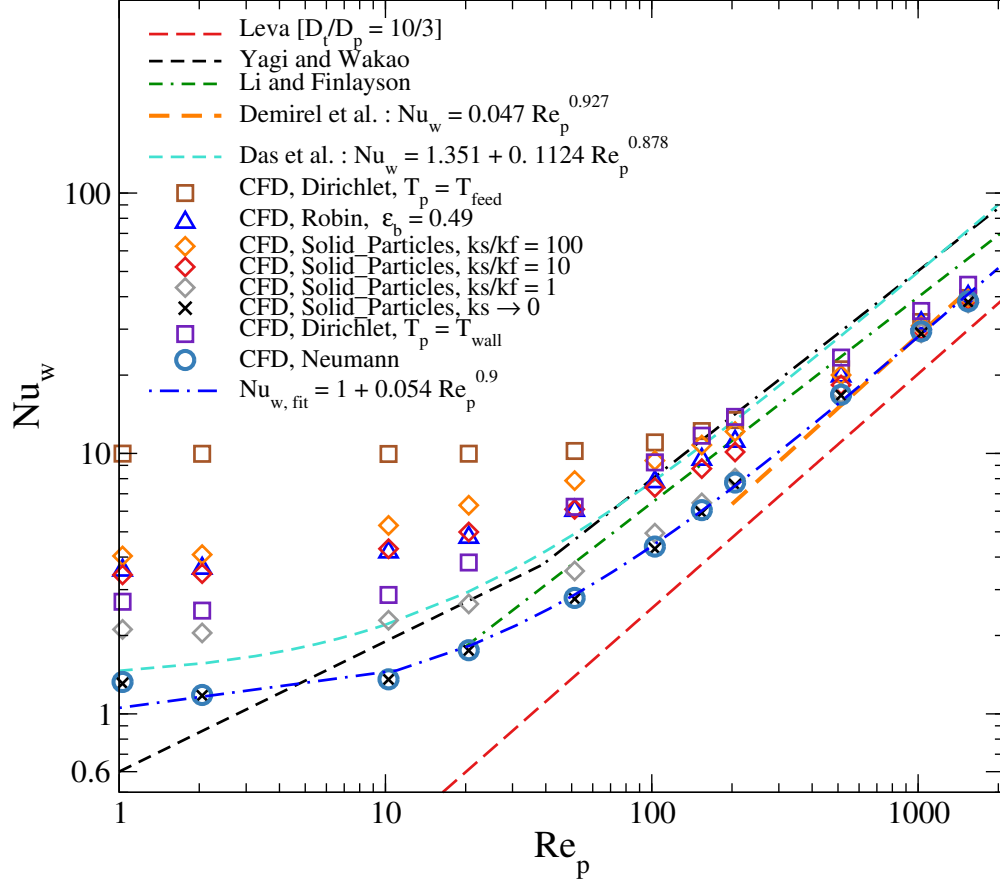


Figure 2.6: Model fitting and comparison with correlations for Nu_w versus Re_p available across literature (Legend refers to: Leva^[89], Yagi and Wakao^[92], Li and Finlayson^[95], Demirel et al.^[101], and Das et al.^[64]).

rate, as the k_s/k_f ratio increases, the temperature is quickly dissipated through the particles to the isothermally-maintained wall, and radial dependency diminishes. For the limiting solid thermal conductivity set of simulations (Figure 2.7A), we observe high-temperature gradients in the core particles near the entrance of the fixed bed even for low flow rates. In this system, it is imperative to consider the plausibility of thermal runaway for reactor design.

An interesting observation worth noting is that Nu_w obtained from the Robin BC using Gunn's correlation given by Equation (2.10) is very close to that obtained for $k_s/k_f = 10$. While it could be tempting to equate Nu_w results from the Gunn correlation to the case $k_s/k_f = 10$, insights from the 3D particle contours must simultaneously be considered.

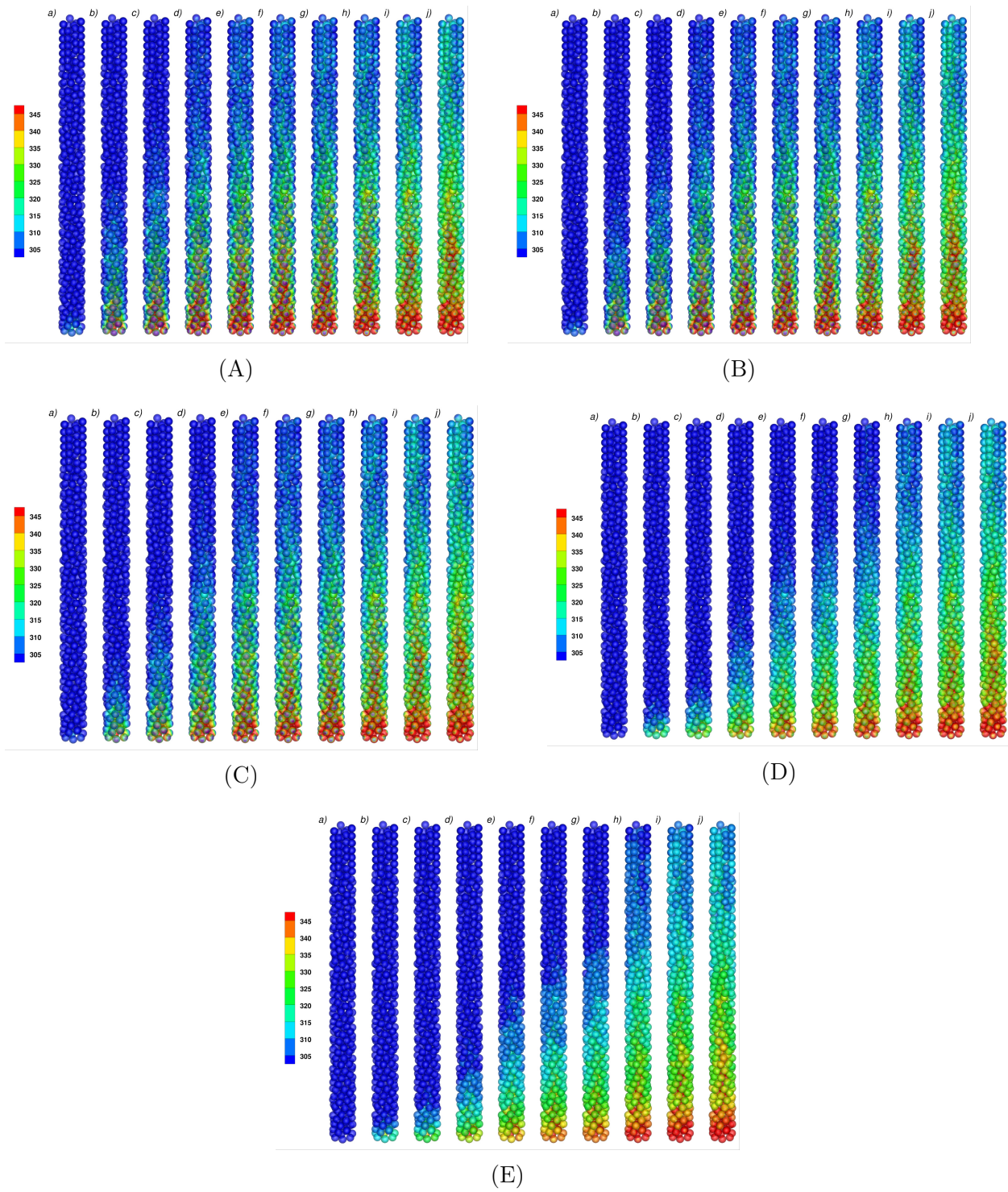


Figure 2.7: Particle surface temperature (T , K) contours for various k_s/k_f ratios: (A) $k_s/k_f \rightarrow 0$; (B) $k_s/k_f = 0.1$; (C) $k_s/k_f = 1$; (D) $k_s/k_f = 10$; (E) $k_s/k_f = 100$. [a–j] correspond to Re_p following Table 2.5]

Contours from Figure 2.5 are very distinct from those of Figure 2.7C.

To better interpret and compare results, the centreline temperature of the packed bed was extracted and plotted. The centreline is the furthest away from the cold bed wall, and the gas temperature is expected to be the highest along this line. Figure 2.8 illustrates the non-dimensional centreline temperature T^* vs the non-dimensional length z/L . T^* is given by the following:

$$T^* = \frac{T_{gas} - T_w}{T_{feed} - T_w} \quad (2.23)$$

We see that T^* along the bed quickly approaches 0 as the k_s/k_f ratio increases. These analyses may yield additional insights into the bed length requirements for heat removal. From Figures 2.8C, 2.8D, and 2.8E, T^* fades away within half the bed length for flow rate corresponding to $Re_p = 10$. Likewise, after analysis of Figures 2.8A and 2.8B, we note that the T^* for flow rates corresponding to Re_p 150 and 500 lie within proximity.

Results from these steady-state heat transfer simulations may be reorganized to delineate the influence of the solid thermal conductivity on the centreline temperature for a given flow rate. Figure 2.9 shows that as $Re_p \uparrow$, T^* shifts towards the origin. The T^* profile curves are most compressed for the $Re_p = 500$, indicating that the solid conductivity does not matter as much for high flow rates. This reinforces the observation that the reduction parameter Nu_w for various k_s/k_f sensitivity simulations converges as $Re_p \uparrow$, shown in Figure 2.6. Lastly, the differential in the bulk gas and solid temperatures, ΔT , was determined for various solid conductivities. ΔT is plotted on Figure 2.10 and is calculated from the volume-averaged bulk gas and solid temperatures as follows:

$$\Delta T = \langle T_{gas} \rangle - \langle T_{solid} \rangle \quad (2.24)$$

We observe a very peculiar behaviour. For creep flow, ΔT is invariable to the thermal conductivity. On increasing flow rate, there is a negligible increase in ΔT . As Re_p increases, it is postulated that there is a higher degree of wall channelling and, therefore, increased fluid–wall heat exchange with the wall. This leads to the gas leaving the bed at a lower bulk temperature than the solid ($\Delta T < 0$).

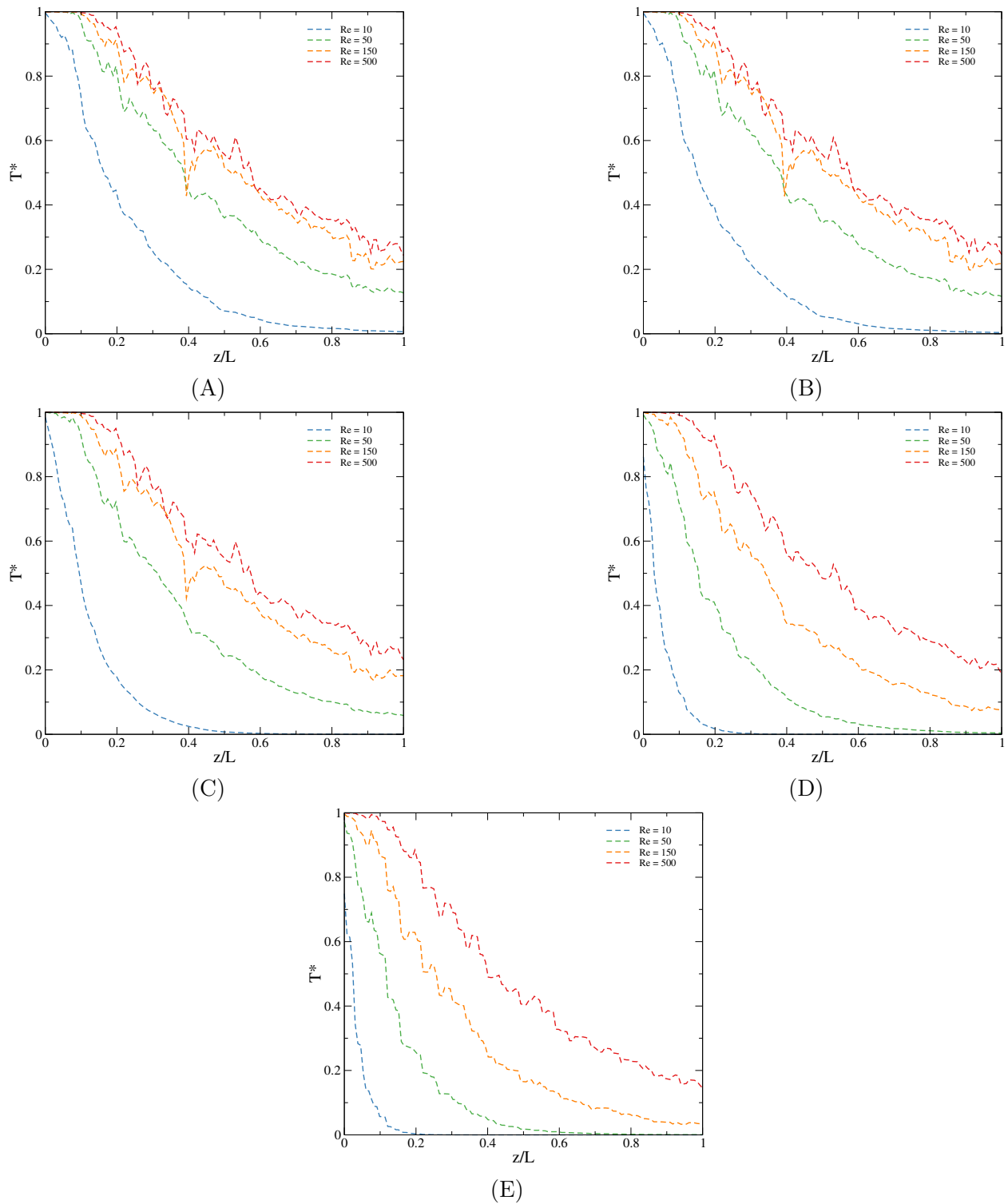


Figure 2.8: Non-dimensional centrelines temperature along non-dimensional bed length for various k_s/k_f ratios: (A) $k_s/k_f \rightarrow 0$; (B) $k_s/k_f = 0.1$; (C) $k_s/k_f = 1$; (D) $k_s/k_f = 10$; (E) $k_s/k_f = 100$.

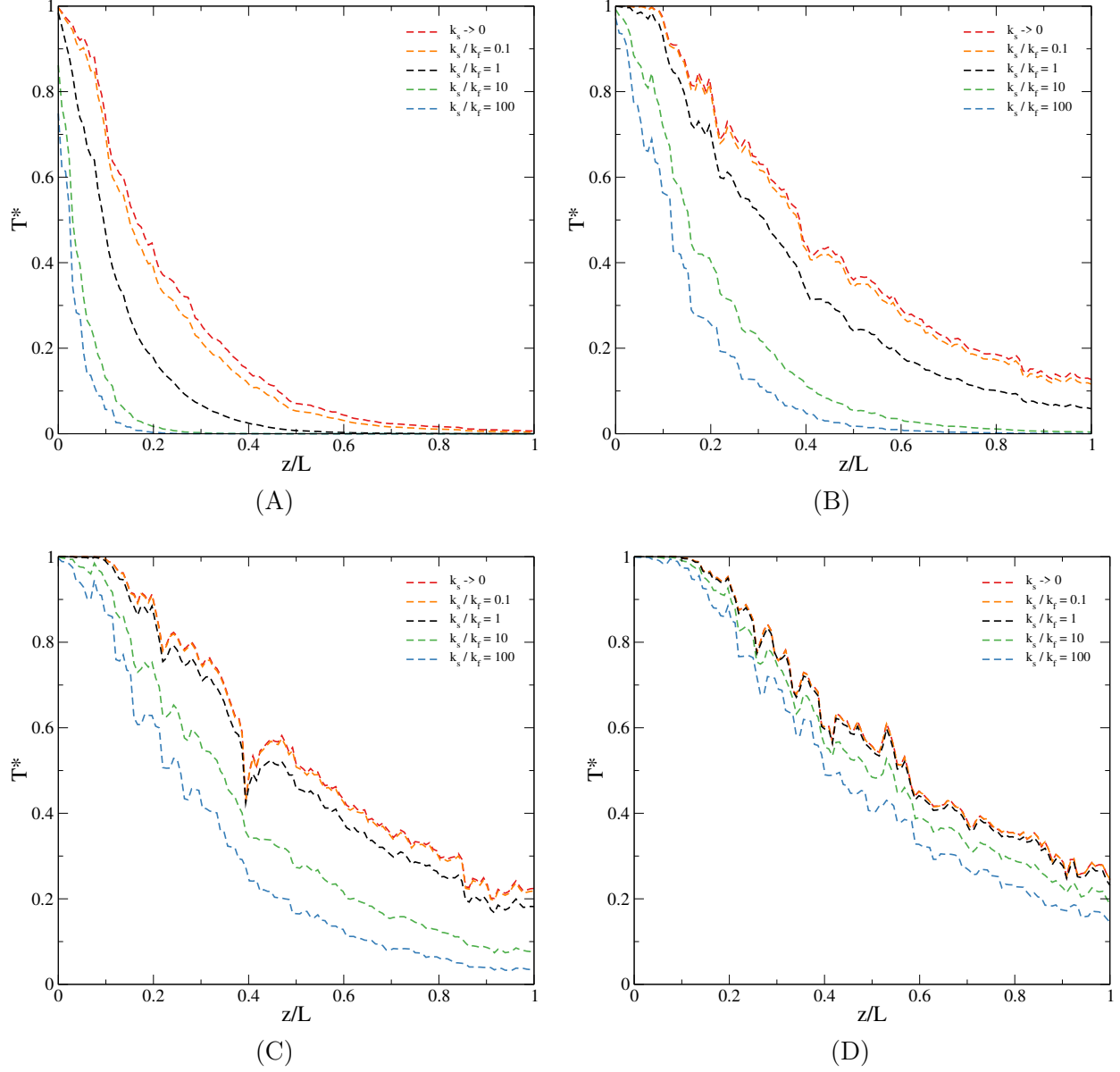


Figure 2.9: Non-dimensional centreline temperature along non-dimensional bed length for various Re_p : (A) $Re_p = 10$; (B) $Re_p = 50$; (C) $Re_p = 150$; (D) $Re_p = 500$.

Finally, we discuss the influence of natural convection on the heat transfer between gas flow and the side wall. Natural convection and buoyancy-driven flow could be expected within fixed beds for low Re_p flows. The Boussinesq approximation was applied in CFD calculations. Table 2.11 shows Nu_w calculated numerically for two different values of ΔT , taking into account the influence of gravity on heat transfer. The values for the relevant parameters, namely fluid density ρ_0 , operating temperature, T_0 , and the thermal expansion

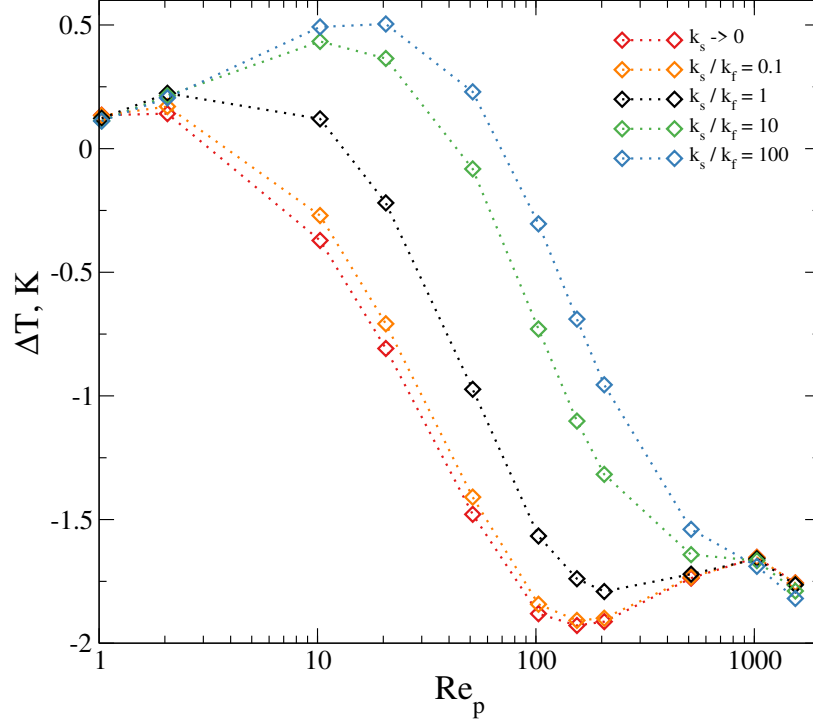


Figure 2.10: $\langle T_{gas} \rangle - \langle T_{solid} \rangle$ for various k_s/k_f ratios [Re_p flows as per Table 2.5].

coefficient β , are listed in Table 2.11. Note that here, T_0 is defined as the arithmetic mean of the T_{feed} and T_w . As the temperature differential between the feed and the wall increases, the effect of buoyancy on the gas–wall heat transfer is more pronounced, and the Nu_w obtained decreases as ΔT increases. We note that for the limiting case of our fluid flow corresponding to $Re_p = 1$, the deviation is not more than 20% off from when buoyancy effects are not considered. It is fairly evident that the deviation in the two sets of Nu_w is almost negligible by $Re_p = 10$. To illustrate the impact of the natural convection on the heat transfer inside the fixed bed, Figure 2.11 compares contour plots of the temperature and velocity streamlines at the inlet of the fixed bed with and without considering buoyancy-driven flows at $Re_p = 1$ for two k_s/k_f ratios and two feed temperatures T_{feed} . For lucid comparison of temperature profiles, the non-dimensional gas temperature, T^* given by Equation (2.23), is calculated and shown. It can be seen that the natural convection influences gas flow at the entrance to the fixed bed zone only.

Table 2.11: Feed temperature heat transfer sensitivity for buoyancy-driven flows.

$\frac{k_s}{k_f}$	Re_p	Nu_w without buoyancy	Nu_w Boussinesq buoyancy ($\Delta T = 50K$)	Rel. % deviation	Nu_w Boussinesq buoyancy ($\Delta T = 300K$)	Rel. % deviation
0	1	1.3076	1.1865	9.26%	1.0660	18.48%
0	10	1.3558	1.3472	0.64%	1.3200	2.64%
1	1	2.1108	1.9376	8.21%	1.7880	15.29%
1	10	2.2886	2.2757	0.56%	2.2340	2.39%
100	1	4.0396	3.7909	6.16%	3.5428	12.30%
100	10	5.2944	5.3116	0.33%	5.2604	0.64%

Parameter	Value	T_w 300 K	Value	Units
ρ_0	1.225		1.225	$\frac{kg}{m^3}$
T_{feed}	350 K		600 K	K
T_0	325 K		450 K	K
β	0.003077		0.002222	K^{-1}

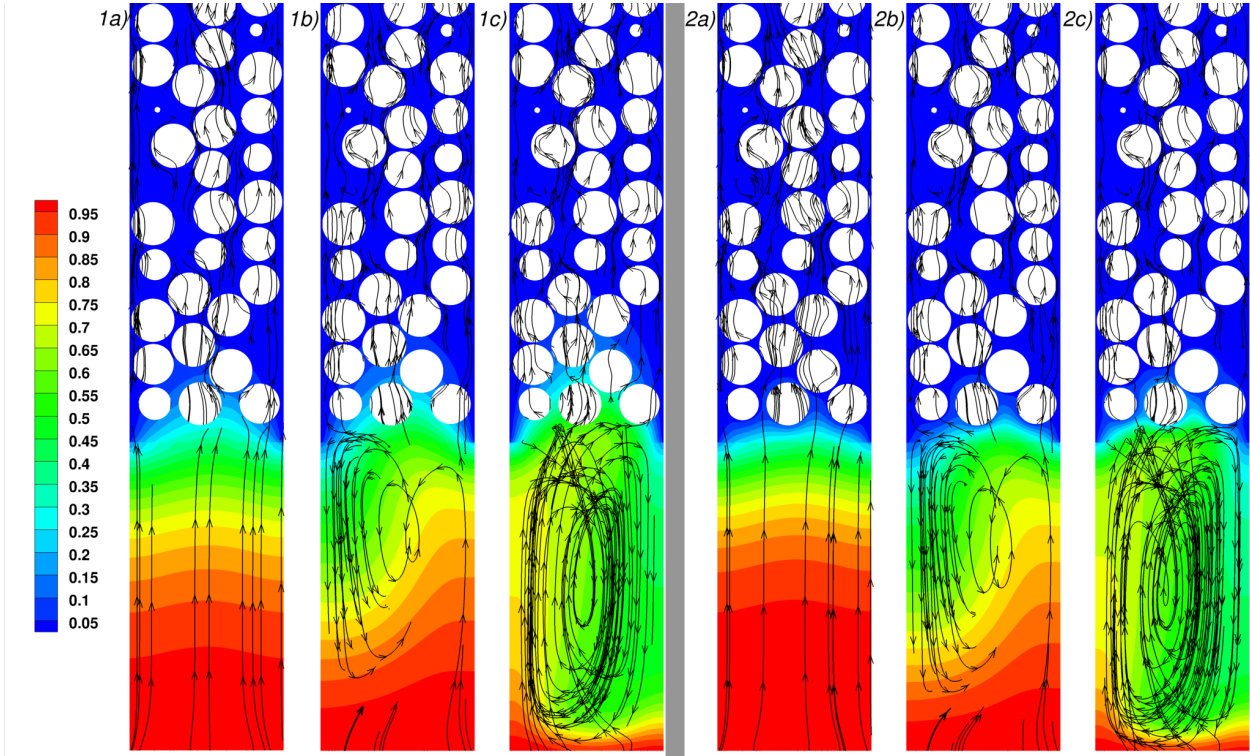


Figure 2.11: 2D slice depicting non-dimensional gas temperature (T^* , [-]) contours and velocity streamlines compared (a) without and (b), (c) with buoyancy-driven flow consideration at $Re_p = 1$ for two feed temperatures and two k_s/k_f ratios. Here, 1) $k_s/k_f = 1$; 2) $k_s/k_f = 100$, (b) $T_{feed} - T_w = 50K$; (c) $T_{feed} - T_w = 300K$.

2.5 Conclusion

In this work, the heat transfer at the wall in a fixed bed with the tube-to-particle diameter ratio $\frac{D_t}{D_p} = 3.3$ was calculated numerically. The commercial 3D CFD solver Ansys Fluent 19 was adopted to calculate the wall Nusselt number, Nu_w , for different values of the Reynolds numbers ($1 \leq Re_p < 1500$) based on the particle diameter and inlet gas velocity. Two basic cases were considered: one corresponds to the fixed bed with hollow particles and different boundary conditions on the particle surface (Dirichlet, Neumann, and Robin), and the second case includes the fixed bed with solid particles with different ratios between the thermal conductivity of particles and gas ($0 < k_s/k_f \leq 100$). Results of simulations revealed that for the range of the Reynolds numbers $Re_p < 110$, the boundary condition on the particle surface influences values of Nu_w . In particular, the Dirichlet boundary condition with particles maintained isothermally ($T_s = T_{feed}$) produces the highest Nu_w values compared to the system representing convective heat transfer between the particle and the fluid flow (Robin boundary condition) and fully insulated particles (Neumann boundary condition). The difference is about 300%-200% for $1 \leq Re_p \leq 20$. The results of simulations for the 2nd case with different k_s/k_f values showed that Nu_w predicted for isothermal particles is close to the case $k_s/k_f = 0$. At the same time, Nu_w values calculated for $k_s/k_f = 10$ are close to Nu_w defined for Robin boundary conditions on the particle surface. *Remarkably, the wall Nusselt number predicted for $Re_p > 120$ using all three boundary conditions and all ratios of k_s/k_f converge to one curve which closely follows experimental data by Demirel et al.^[101]*

Chapter 3

Implementation and validation of boundary conditions between a chemical reactor and ambient air^{*}

This work is dedicated to the development and validation of boundary conditions for a hot object cooled in a colder environment due to natural convection, radiation and evaporation. The main background of this research is to present boundary conditions for a hot reactor in cold ambient air, where the reactor walls are not thermally insulated. Water cooling in a standard small paper cup (coffee cup) was selected as a validation test. The experimental data comprise time histories of the cup's side wall temperature measured using three thermoelements. The initial water temperature was set to 94°C. The ambient air temperature was fixed at 25°C and the air humidity at 20%. The computational model is based on unsteady laminar flow Navier-Stokes equations coupled with the heat transfer equation. The water density and all water transport properties (i.e., thermal conductivity, molecular viscosity, and specific heat capacity) are temperature-dependent. Numerical simulations in two-dimensional (2D) axisymmetry aligned well with the results from experiments. Including evaporative cooling on the top water surface proved essential to accurately determine the temperature profile. The boundary conditions are implemented into the Ansys Fluent

^{*}This chapter is based on the manuscript submitted to the International Communications in Heat and Mass Transfer journal

2022R2 computational fluid dynamics (CFD) commercial solver using user-defined functions (UDFs). The validated UDFs may be ported as a boundary condition for fixed beds and adsorption columns to improve the prediction of thermal profiles in both lab-scale and industrial-scale units.

Keywords: CFD, User-defined functions, Heat transfer in columns, Natural convection, Evaporative cooling

3.1 Introduction

One of the challenges in modeling industrial-scale chemical reactors is the need to incorporate the ambient conditions surrounding such reactors. The conditions must be taken into account due to the heat transfer between the ambient air and reactor walls. There are two basic approaches to overcome this problem. The first method is the computational domain, which includes both the reactor and the ambient air. The computational domain is vast, and computations are costly. The best illustration of this method is calculating the heat transfer between a moving sphere or particle and an ambient fluid, e.g., see the works^[132,133], or between a hot cylinder at rest and an ambient fluid^[134]. In particular, computational domains must be significantly larger than the object under investigation to model free-stream conditions. This method is always used when necessary to calculate the heat transfer between fluids and walls directly. Such problems are classified as conjugate heat transfer problems, e.g., see the works^[135–138]. This type of method is widely used in heat transfer problems related to heating and cooling^[139,140]. The class of methods where the computational domain is extended to model the heat transfer directly may be used universally. However, it requires expensive computational resources due to the voluminous computational domain. So-called immersed boundary methods are used in this model type^[141].

The second way to model conjugate heat transfer problems involves computational domains that consist of the domain under investigation (e.g., the chemical reactor), while the ambient is excluded. Instead of the ambient air, appropriate boundary conditions are applied on the outer surface of the computational domain corresponding to the reactor walls or object boundary^[142], see Fig.(3.1b). Although this method is computationally more efficient,

it requires the correct choice and implementation of boundary conditions on the domain boundaries^[137].

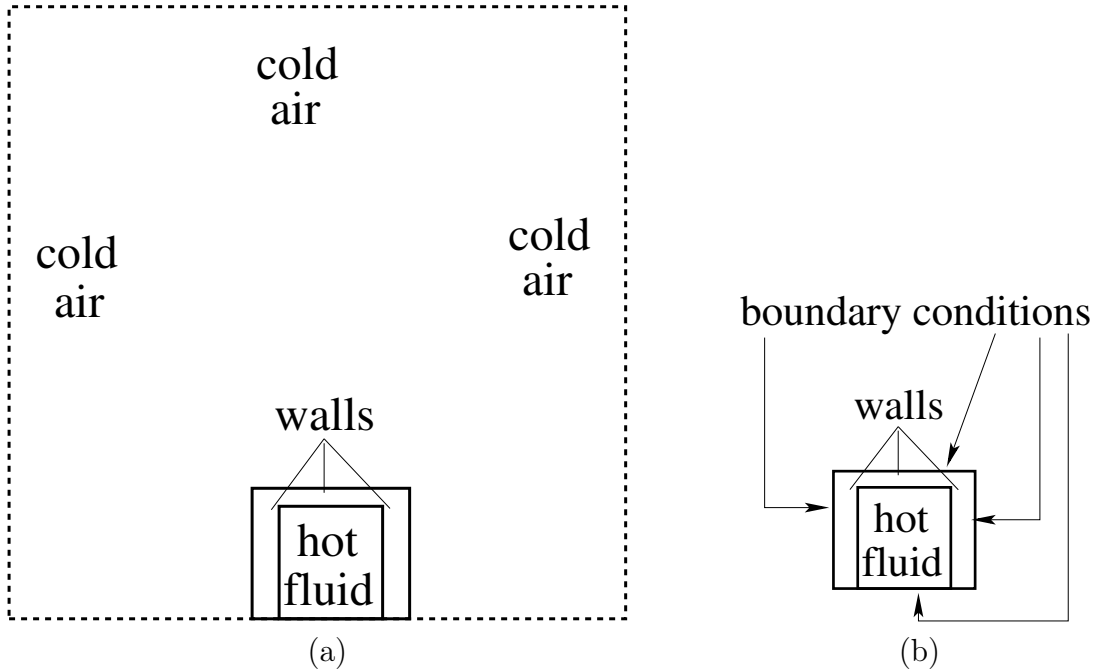


Figure 3.1: Schematic representation of computational domains for two ways of modeling: (a) conjugate domain (b) short domain

In the case of natural convection between the ‘hot’ surface and the ‘cold’ free stream, the wall–ambient Nusselt number, Nu_{conv} , is often expressed in terms of the free-stream Rayleigh number, Ra , to relate the properties of the system heat transfer to the buoyancy-driven flow characteristics of the system^[143]. Typically, Ra is based on the characteristic length of the surface, L_c , and the surface area-averaged temperature $\langle T_s \rangle$ as follows:

$$Ra = \frac{g\beta(\langle T_s \rangle - T_\infty)L_c^3}{\alpha_\infty\nu_\infty}; \quad Nu_{conv} = \frac{h_{conv}L_c}{k_\infty}; \quad L_c = \frac{A_s}{P}$$

where A_s and P are the surface area and perimeter, respectively.

Regarding natural convection-driven flows, CFD made significant progress in modeling the heat transfer for laminar and turbulent flows, e.g., see the works^[144–146]. Our work shall be dedicated to investigating the thermal boundary conditions between a small hot cavity and an extremely large enclosure, such that the geometry of the ambient does not contort the flow and heat transfer characteristics of our computational domain.

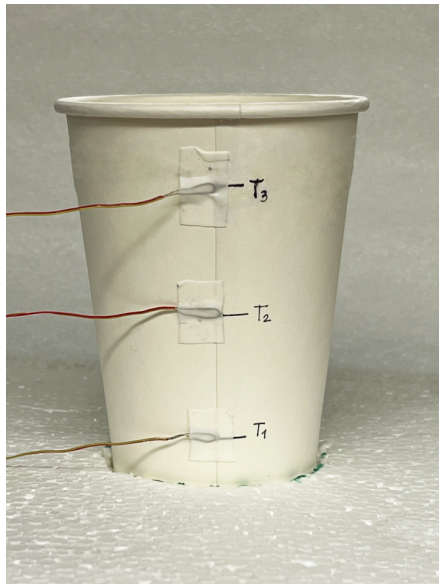
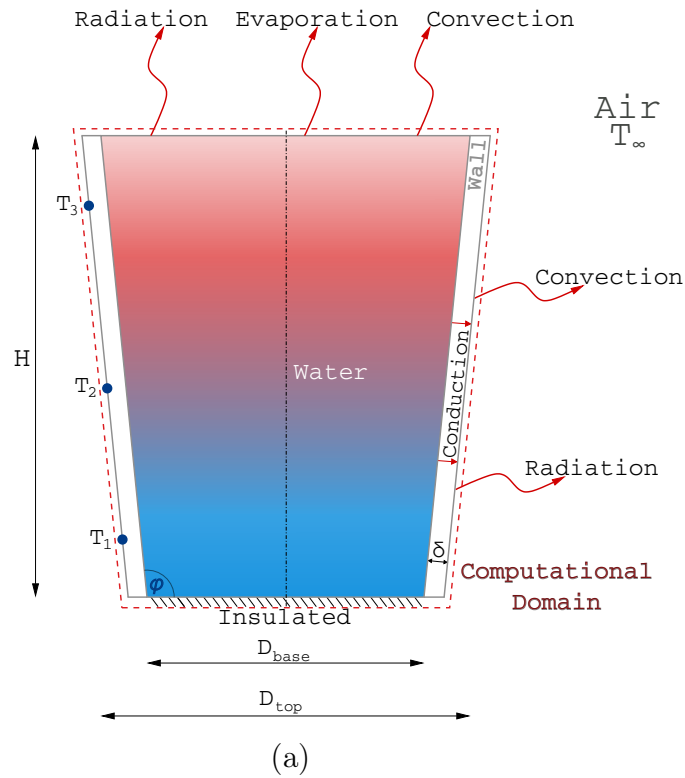
The present investigation additionally delves into the aspects of evaporative cooling as a relevant heat transfer mechanism when the surface of a chemical reactor is exposed to the ambient. Similarly to the case of natural convection heat transfer, the heat transfer boundary condition derived from evaporative cooling does not exist natively in commercial CFD solvers to date. Several evaporative cooling models have been proposed over the years and may be found in the review by [Elango et al.](#)^[147]. More recently, [Bansal et al.](#) developed a zero-dimensional scale-bridging model investigating an ice particle melting in the air^[142]. Based on the works reviewed, they emphasized the need to take into account natural convection and the two other pertinent heat transfer mechanisms involved: radiation and evaporative cooling. A physically based constitutive evaporative cooling mass flux equation for horizontal surfaces was derived through mass flux theory and experimentally validated.

However, the direct modeling of conjugate heat transfer problems driven by natural convection is not trivial. An analysis of published works suggests that few investigations have studied how thermal boundary conditions at the boundaries of chemical reactors affect the hydrodynamics and thermal characteristics of fluid within the reactor. Moreover, to the best of our knowledge, the combined effects of radiation, natural convection and evaporative cooling on a hot cavity placed in an extremely large ambient have yet to be reported. In this work, we develop and validate boundary conditions for a hot reactor in cold ambient air where the reactor walls are not thermally insulated. Physically grounded thermal boundary conditions are applied on the reactor's side walls and on the top surface, which is exposed to the environment. Numerical findings are then compared with experimental measurements.

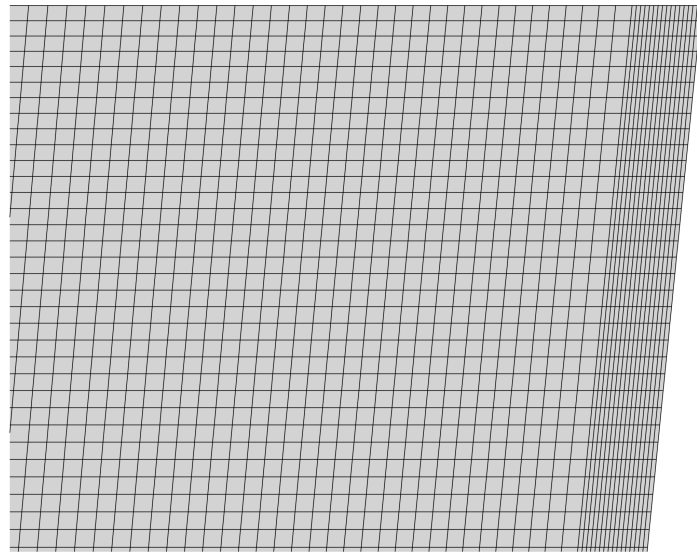
3.2 Problem and Model Formulation

In this work, the computational domain consists of a hot fluid (i.e., water) in a paper cup. Fig.(3.2a) illustrates the computational domain under consideration. The geometry of the cup is to scale. The heat transfer mechanisms pertinent to all cup surfaces are also depicted. The cup is assumed to be anchored on a fully insulated base. The side wall is subject to heat loss due to natural convection and radiation. The top, free surface of the water in the cup loses heat to the ambient through the combined effects of natural convection, radiation,

and evaporative cooling. It is imperative to state that the correlations for natural convection differ for horizontal and vertical surfaces and are sourced from [Incropera et al.](#)^[143].



(b)



(c)

Figure 3.2: Coffee cup setup. (a) Schematic indicating the computational domain, heat transfer mechanisms, and the locations of the thermoelements T_i (b) Experimental setup indicating the thermoelements (c) Non-uniform, structured grid of the 104 000 cell mesh

Heat loss through radiation depends only on the local temperature, while convective heat transfer depends on the reductive surface-averaged temperature. All heat transfer mechanisms from the fluid to the ambient must be carefully taken into consideration to measure the temperature profile over time accurately. Prior to presenting the laminar mathematical model, the following assumptions are put forth:

1. The ambient temperature, T_∞ , is constant
2. All fluid (water) transport properties in the cup are temperature dependent.
3. The thickness of the cup is constant
4. The base of the cup is fully insulated
5. Mass transfer of water from the cup to the ambient is negligible and neglected
6. The water at the start of the simulation is assumed to be still and at a uniform initial temperature throughout.

A two-dimensional (2D) axisymmetric, transient, laminar flow model for the in-situ fluid (water) is employed, and modeling the ambient is avoided. The governing partial differential equations for continuity, momentum, and energy are laid out in Table 3.1.

Table 3.1: Transient laminar flow model PDEs for water in the coffee cup

<i>Name</i>	<i>Equation</i>
Continuity equation	$\frac{\partial \rho}{\partial t} + \nabla \cdot (\rho \vec{v}) = 0$
Momentum equation	$\frac{\partial(\rho \vec{v})}{\partial t} + \nabla \cdot (\rho \vec{v} \vec{v}) = -\nabla p + \nabla \cdot [\mu (\nabla \vec{v} + \nabla \vec{v}^T)] + \rho \vec{g}$
Energy Equation	$\frac{\partial(\rho C_p T)}{\partial t} + \nabla \cdot (\rho C_p T \vec{v}) = \nabla \cdot (k \nabla T)$

where all transport properties of water, ρ , C_p , k , and μ are temperature dependent. Below, thermophysical polynomials have been generated via regression from discrete points from HeatAtlas^[148] and are depicted in Fig.(3.3).

1. Density: $\rho \text{ (kg/m}^3\text{)} = -0.00365471 \cdot T^2 + 1.93017 \cdot T + 746.025$ (T, K)
2. Specific heat capacity: $C_p \text{ (J/kg/K)} \equiv$ Piecewise-linear (FLUENT default)
3. Thermal conductivity: $k \text{ (W/m/K)} = -9.29827 \times 10^{-6} \cdot T^2 + 0.0071857 \cdot T - 0.7107$ (T, K)
4. Viscosity: $\mu \text{ (kg/m/s)} = -2.80572 \times 10^{-9} \cdot T^3 + 2.90283 \times 10^{-6} \cdot T^2 - 0.00100532 \cdot T + 0.116947$ (T, K)

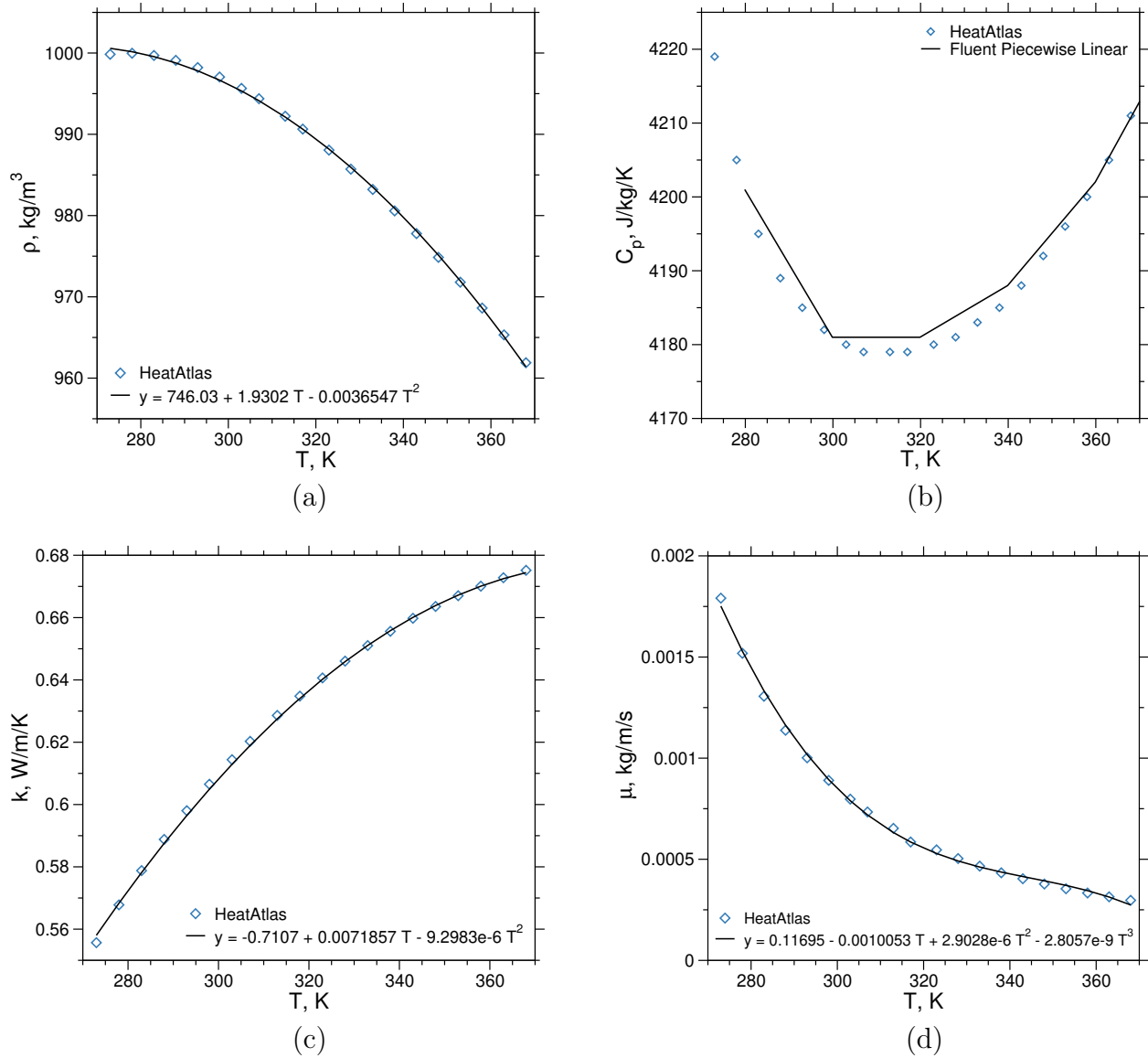


Figure 3.3: Thermophysical properties of water. (a) Density, ρ (b) Specific heat capacity, C_p (c) Thermal conductivity, k (d) Viscosity, μ

The density, ρ , and thermal conductivity, k , were described well with a quadratic fit with R^2 values of 0.999350 and 0.998631, respectively. A cubic polynomial is required to adequately represent the viscosity, μ , with an R^2 value of 0.998356. The Fluent material package default piecewise-linear expression is used for the specific heat capacity C_p . Note that all temperature values are in K.

3.2.1 Boundary conditions

The physical mechanisms involved in the water-cooling process require both momentum and energy boundary conditions. Note that each boundary is described with a corresponding set of equations due to the difference in geometry and position (e.g., side and bottom walls). Boundary conditions can be grouped into the bottom, side walls, and top surface.

3.2.1.1 Bottom

The bottom surface of the cup is in contact with the fluid and has the no-slip condition:

$$v \Big|_{z=0} = 0 \quad (3.1)$$

where v is the fluid velocity.

Since the cup is firmly attached to the insulator, the surface experiences zero flux in the normal direction. Thus, the Neumann boundary condition at the bottom can be written as follows:

$$-k_f \frac{\partial T}{\partial n} \Big|_{z=0} = 0 \quad (3.2)$$

3.2.1.2 Side walls

The domain contains two zones: solid and liquid. As a result, the outer side wall comes into contact with the ambient, while the inner side wall is in contact with water. For the inner wall, the momentum equation is subject to the no-slip condition with neglected wall roughness and is expressed as follows:

$$v \Big|_{r=r_{w,i}(z)} = 0 \quad (3.3)$$

The heat rate is conservative and can be represented at the wall through either conduction or the sum of convection and radiation. Hence, the energy boundary at the outer wall is enclosed by the balance of these terms as follows:

$$-k_w \frac{\partial T}{\partial n} \Big|_{r=r_{w,o}(z)} = q''_{\Sigma} \quad (3.4)$$

where $q''_{\Sigma} = h_{\Sigma}(T_{w,o} - T_{\infty})$ is the total heat flux and $h_{\Sigma} = h_{conv} + h_{rad}$ is the total heat transfer coefficient. Note that the linear summation of the convective, h_{conv} , and radiative, h_{rad} , components of the heat transfer is justified by their parallel nature.

The radiative heat transfer coefficient is found as follows:

$$h_{rad} = \sigma \varepsilon_{wall} (T_{w,o} + T_{\infty})(T_{w,o}^2 + T_{\infty}^2) \quad (3.5)$$

where $\sigma \approx 5.67 \cdot 10^{-8} \text{ W}/(\text{m}^2 \cdot \text{K}^4)$ is the Stefan-Boltzmann constant, $\varepsilon_{wall} = 0.96$ is the wall emissivity, $T_{w,o}$ is the local outer wall temperature, $T_{\infty} = 25.3 \text{ }^{\circ}\text{C}$ is the ambient air temperature.

The convective heat transfer coefficient is uniform along the entire side wall of height H and depends on the averaged Nusselt number, \overline{Nu}_{conv} , as follows:

$$h_{conv} = \frac{\overline{Nu}_{conv} \cdot k_{\infty}}{H} \quad (3.6)$$

where $k_{\infty} = 0.0242 \text{ W}/\text{m}\cdot\text{K}$ is the ambient air's thermal conductivity.

However, since there is no separate zone for ambient air, the convective heat transport of air, driven by buoyancy, is accounted for using an empirical correlation for the Nusselt number^[149], which is a function of the Rayleigh number, Ra , and the Prandtl number of air, here assumed to be constant, $Pr = 0.708$. The correlation considers the side to be a vertical cylinder due to the negligibly small wall inclination angle:

$$\overline{Nu}_{conv} = \left(0.825 + \frac{0.387 Ra^{1/6}}{\left[1 + \left(\frac{0.492}{Pr} \right)^{9/16} \right]^{8/27}} \right)^2 \quad (3.7a)$$

$$Ra = \frac{g\beta(\langle T_{side} \rangle - T_\infty)H^3}{\alpha_\infty\nu_\infty} \quad (3.7b)$$

where α_∞ is the thermal diffusivity of the air, β is its thermal expansion coefficient and ν_∞ is its kinematic viscosity. The outer surface area-averaged temperature, $\langle T_{side} \rangle$, is estimated based on the temperature of each face element's centroid, $T_{(w,o),i}$, as follows:

$$\langle T_{side} \rangle = \frac{\int_S T_{w,o} dS}{\int_S dS} = \frac{\sum_{N_w} T_{(w,o),i} \Delta S_i}{\sum_{N_w} \Delta S_i} \quad (3.8)$$

where ΔS_i is the area of i^{th} face and N_w is the total number of faces.

3.2.1.3 Top surface

The top is an open surface facing no shear stress. Thus, the momentum boundary condition takes the following form:

$$v_z \Big|_{z=H} = 0 ; \quad \frac{\partial v_r}{\partial z} \Big|_{z=H} = 0 \quad (3.9)$$

The top boundary condition for energy implies that the heat transfer rates from the bulk and to the atmosphere are equal. The expression can be written as follows:

$$-k_f \frac{\partial T}{\partial n} \Big|_{z=H} = q''_{\Sigma,top} \quad (3.10)$$

where, $q''_{\Sigma,top} = h_{\Sigma,top}(T_{top} - T_\infty)$ is the total heat flux from the top surface, $h_{\Sigma,top} = h_{conv,top} + h_{rad} + h_{evap}$ is the total heat transfer coefficient at the top surface, which depends on the convective, radiative and evaporative components, respectively. Correlations for the first two components are written similarly to those for the side wall:

$$h_{conv,top} = \frac{\overline{Nu}_{conv,top} \cdot k_\infty}{L_c} \quad (3.11a)$$

$$h_{rad} = \sigma \varepsilon_{top} (T_{top} + T_\infty) (T_{top}^2 + T_\infty^2) \quad (3.11b)$$

where $L_c = D_{top}/4$ is the characteristic length for the top surface, D_{top} is the top surface diameter and T_{top} is the local temperature at the top.

The correlation reported by [Lloyd and Moran](#)^[150] estimates an average Nusselt number for the top surface:

$$\overline{Nu}_{conv,top} = \begin{cases} 0.54Ra^{1/4}, & \text{for } 10^4 \leq Ra \leq 10^7 \\ 0.15Ra^{1/3}, & \text{for } 10^7 < Ra \leq 10^{11} \end{cases} \quad (3.12a)$$

$$Ra = \frac{g\beta(\langle T_{top} \rangle - T_\infty)L_c^3}{\alpha_\infty\nu_\infty} \quad (3.12b)$$

The area-averaged temperature at the top is calculated similarly to that at the side, as follows:

$$\langle T_{top} \rangle = \frac{\int_{S_{top}} T_{top} dS_{top}}{\int_{S_{top}} dS_{top}} = \frac{\sum_{N'_w} T_{top,i} \Delta S_{top,i}}{\sum_{N'_w} \Delta S_{top,i}} \quad (3.13)$$

The evaporative cooling heat transfer coefficient, h_{evap} , is calculated as follows^[142]:

$$h_{evap} \cdot (T_{top} - T_\infty) = q''_{top,evap} = \dot{m}''_{evap} \cdot \Delta H_v \quad (3.14a)$$

$$\dot{m}''_{evap} = \frac{1}{\delta_t} \rho_\infty D_g \ln \left(\frac{1 - Y_\infty}{1 - Y_s} \right) \quad (3.14b)$$

$$\delta_t = \frac{L_c}{\overline{Nu}_{conv,top}} \quad (3.14c)$$

where, ΔH_v is the latent heat of evaporation of water, D_g is the diffusion coefficient, approximated from the Lewis number equal to 1, $Le = 1$; ρ_∞ is the density of the ambient fluid (air), δ_t is the thermal boundary layer, Y_∞ is the mass fraction of water vapor in the ambient, Y_s is the mass fraction of water vapor on the surface. To calculate Y_∞ and Y_s , refer to the work by [Bansal et al.](#)^[142]. In our study, the ambient relative humidity, ϕ , is 0.2.

3.2.2 Experiment

The experimental setup consisted of a standard paper cup with dimensions as shown in Table 3.2. The cup was placed on a thermocol (polystyrene) layer to insulate the base. Three K-type thermocouples were adhered using high-temperature adhesive tape along the cup's outer wall so as not to perturb the flow within the cup. Considering the base of the cup to be the $z = 0$ plane, the z-coordinates of the thermoelements T_1 , T_2 , and T_3 are 1.3 cm, 4.74 cm, and 8.9 cm, respectively. However, this meant that the bulk fluid temperature could not be recorded with a standard thermoelement and would require a thermal camera

Table 3.2: Paper cup characteristics

<i>Parameter</i>	<i>Symbol</i>	<i>Value</i>
Base radius	R_{min}	3.15 cm
Top radius	R_{max}	4.20 cm
Cup height	H	10.5 cm
Angle of inclination	φ	95.7°
Paper wall thickness	δ	0.45 mm
Paper wall emissivity	ε_{wall}	0.96
Paper density	ρ_{wall}	500 kg/m ³
Paper specific heat capacity	$C_{p,wall}$	880 J/kg·K
Paper thermal conductivity	k_{wall}	0.07 W/m·K

and image processing to record the fluid bulk temperature. The data acquisition system comprised the Pico[®] TC-08 thermocouple data logger in conjunction with PicoLog v6.2.5 graphical software. The sampling interval for data capture was 1 second. The recorded data was finally exported to a .csv file. Fig.(3.2b) depicts the cup and the three thermoelements. Before water was poured into the cup, the ambient air temperature (thermoelement readings averaged over 20s) was recorded as 25.3°C. After water was poured into the cup, an additional thermocouple was quickly immersed in the bulk and recorded an instantaneous reading of 94.0°C before being withdrawn so as not to induce perturbations.

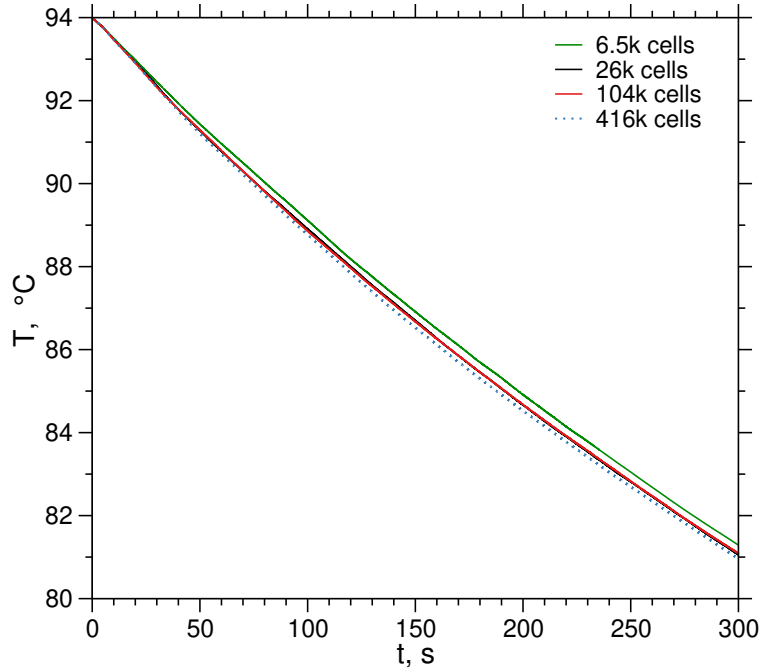
3.3 Numerics

The model is transiently resolved using the Bounded Second Order Implicit formulation for time-derivative discretization. The laminar model is employed to depict the progression of viscous flow. Given its swift and robust attenuation of continuity, momentum, and energy residuals, the SIMPLE scheme is chosen for pressure-velocity coupling. Gradients are evaluated by applying the Least Squares Cell-Based method. The Second Order technique is utilized for pressure interpolation to reduce the amount of numerical diffusion. The energy and convective elements of the momentum equation are discretized utilizing the Second Order Upwind scheme. A summary of the mentioned methods is given in Table 3.3.

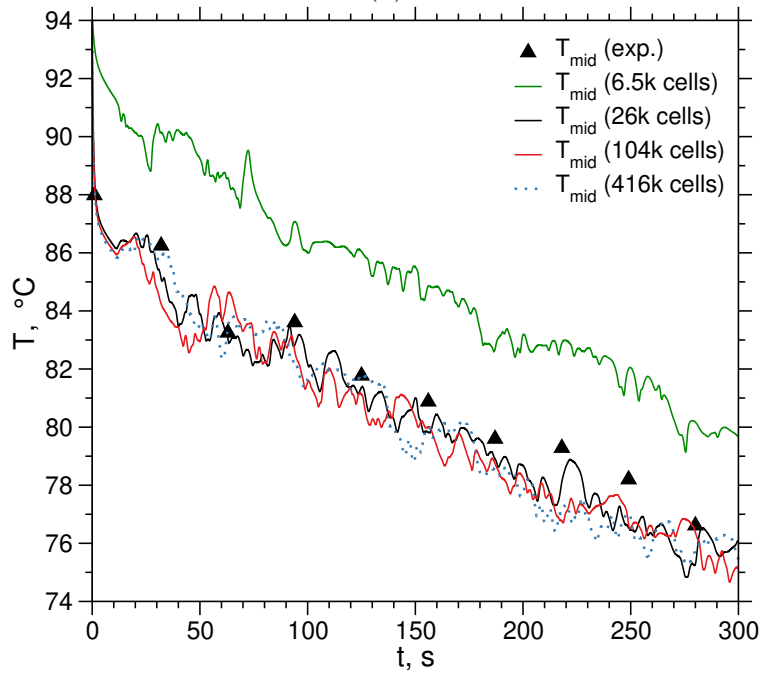
Table 3.3: List of models and schemes^[151] used in the 2D axisymmetric Laminar CFD model

<i>Name</i>	<i>Model/ Scheme Name</i>
Solver	Steady State, Pressure-Based
Flow Model	Laminar
Pressure–Velocity Coupling	SIMPLE ^[126]
Spatial Discretization – Gradient	Least Squares Cell-Based
Spatial Discretization – Pressure	Second Order
Spatial Discretization – All Equations	Second Order Upwind
Transient Formulation	Bounded Second Order Implicit

Assuming that hydrodynamic stability prevails in the cup makes it possible to use a 2D axisymmetric model. The meshes use for both the bulk and the wall are structured and non-uniform. Four meshes with 6 500, 26 000, 104 000, and 416 000 cells were tested to obtain a mesh-independent solution. The mesh refinement routine utilized here is a uniform and consistent doubling of the number of cells per edge. The volume-averaged bulk temperature evolution in Fig.(3.4a) clearly shows how the coarsest mesh overpredicts the temperature, while the other three produce comparable accuracy. A similar conclusion can be reached by collating the local temperature change over time for the meshes studied, as shown in Fig.(3.4b). Note that the temperature probe is the mid-point value for the experiment and the middle ring line-averaged value for the simulations. The experimental temperature, used as a reference value, demonstrates the all meshes are suitable except the coarsest. Therefore, the mesh with 104 000 cells was selected for further investigation to ensure accuracy. Fig.(3.2c) shows a close-up of the grid corresponding to the 104 000 cell mesh. The denser cells near the right edge correspond to the solid wall and are governed by the thermophysical properties of paper, as found in Table 3.2. The side-wall comprises 16 cells along its width and the cell’s aspect ratio is equal to four, which is acceptable for heat conduction occurring mainly in the radial direction. The average cell sizes in the bulk and at the wall are 0.2 mm and 0.03 mm, respectively.



(a)



(b)

Figure 3.4: Set of grid studies. (a) Volume-averaged temperature vs. time (b) Middle ring line-averaged temperature vis-à-vis middle thermoelement, T_2 , vs. time

When 80 iterations are run for each time step, all equations converge to residuals of an order of magnitude of 10^{-6} . The time step is fixed and equals $\Delta t = 0.025$ s.

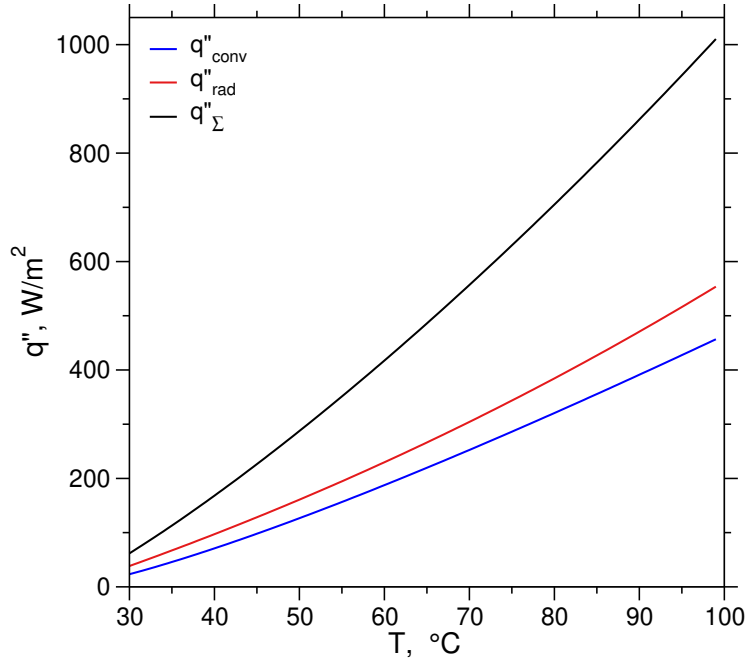
The water vapor pressure at the top surface must be determined to calculate the evaporative heat flux. According to the Dortmund Data Bank, the Antoine equation, which returns vapor pressure in mmHg to the logarithmic base 10 for a temperature input in K, has the following Antoine constants for water: ($A = 8.07131, B = 1730.63, C = -39.724$). The dependency of evaporative cooling on the convective heat transfer is evident in Eq.(3.14c), where the thermal boundary layer, δ_t , depends on the top surface characteristic length, L_c , and the convective Nusselt number, $\overline{Nu}_{conv,top}$.

For verification purposes, the temperature dependence of wall and top surface fluxes were calculated using an in-house MATLAB code and cross-checked with the corresponding UDF obtained values. Fig.(3.5a) and (3.5b) show the temperature dependence of the side wall and top surface heat fluxes, respectively.

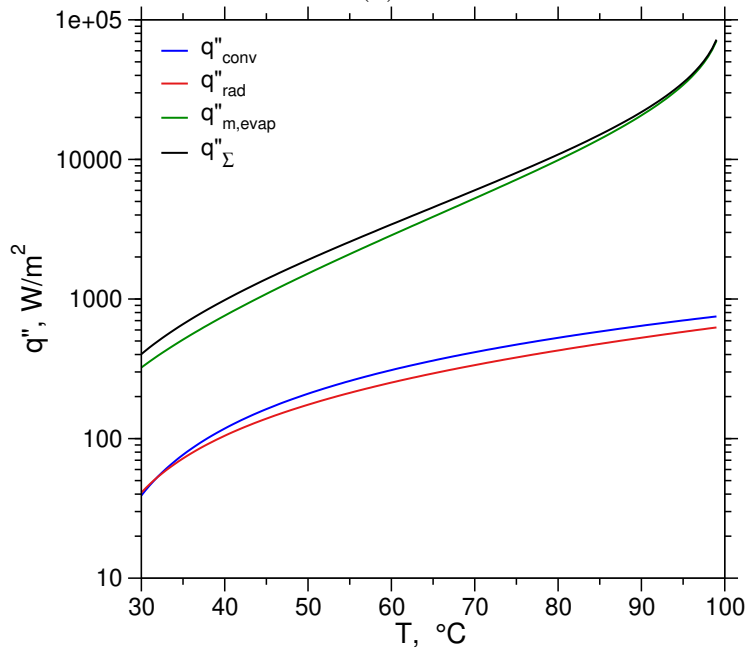
It is interesting to note the sensitivities of the fluxes to temperature. For the side wall, the radiative and convective heat fluxes are of the same order of magnitude, with the former dominating slightly. For the top surface, owing to the Ra-Nu correlation, the convective heat flux is higher than the radiative heat flux. Near boiling temperatures, the evaporative cooling heat flux is about two orders of magnitude higher than the radiative and convective heat fluxes and rapidly decreases to one order of magnitude higher as the temperature drops below 63°C. Over the entire temperature range evaluated, the evaporative heat flux contributes between 77% and 98% of the total heat flux across the top surface. One particular drawback of the MATLAB code is that it does not differentiate between the local and the surface-averaged temperatures.

Comparing the total heat fluxes at the side wall and across the top surface, it is evident that most heat lost from the cavity to the ambient is top-driven. Notwithstanding, the heat rate (\equiv current) q and not the heat flux (\equiv current density) q'' is conservative along the thermal resistance network. Note that the surface area of the side wall is about 4.5 times that of the top.

Finally, the thermal boundary conditions discussed in Sec.(3.2.1) were implemented within FLUENT employing the user-defined functions (UDFs, compiled in C) we developed in-house. This made it possible to expand the solver's capabilities to model natural convection and evaporative cooling, which are not natively present in the commercial pack-



(a)



(b)

Figure 3.5: Temperature dependence of heat fluxes at the (a) side wall and (b) top surface age. Table 3.4 lists the MACROS incorporated into the UDF to help calculate, store, and post-process results. Three co-axial rings were created as iso-surfaces with the z-coordinates noted for the experimental thermoelements to record the outer wall temperatures and thus validate the CFD model.

Table 3.4: Description of all user-defined functions (UDFs) in the hot cavity – cold ambient CFD model

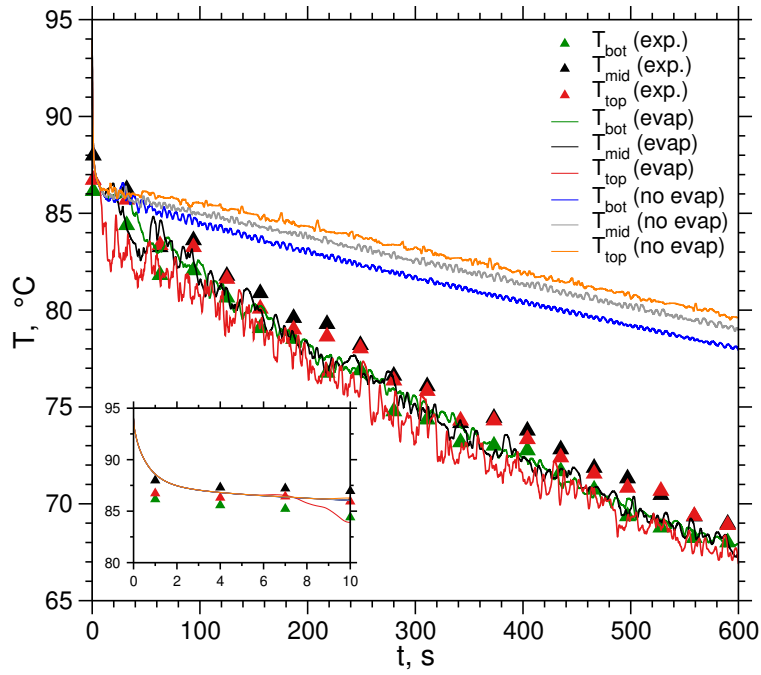
UDF Macro	Main purpose	Output
DEFINE_INIT	Initial values of the side wall heat flux and the top surface heat transfer coefficients are set according to initialized temperature	Reads named expression T_{amb} and sets the value of ambient temperature T_{∞} for calculations within the UDF. Writes initialized side inner wall temp ' T_s ' to file xyz.out. Writes initialized top surface temp ' $T_{s,top}$ ' to file xyzTop.out
DEFINE_ADJUST	Calculates and stores transient side wall surface area averaged T_s and top surface area averaged $T_{s,top}$ every iteration	Calculates transient surface area averaged T_s and overwrites file xyz.out every iteration. Calculates transient surface area averaged $T_{s,top}$ and overwrites file xyzTop.out every iteration
DEFINE_PROFILE (Side wall heat flux BC)	Implements a temperature dependent wall flux according to the physics-based natural convection correlation for vertically inclined surfaces via Newton's method	Reads ' T_s ' from file xyz.out, calculates Rayleigh and Nusselt numbers, and returns wall heat flux dependent on local and side wall surface-averaged temperatures to each face on the side wall. Wall heat flux and natural convection-driven heat transfer coefficient are determined simultaneously
DEFINE_PROFILE (Top surface convection BC)	Implements temperature dependent surface heat transfer coefficient according to the physics-based natural convection correlation for horizontal surfaces.	Reads ' $T_{s,top}$ ' from file xyzTop.out, calculates Rayleigh and Nusselt numbers, calculates evaporative cooling-driven heat flux, and returns top surface heat transfer coefficient dependent on local and top surface-averaged temperatures to each face on the top surface. Natural convection + evaporative cooling driven heat transfer coefficient is determined
DEFINE_EXECUTE_AT_END	At the end of each time step, records continuity residual and transfers face memory data to cell memory for graphical visualization.	The values of side-wall heat flux, side-wall heat transfer coefficient, top surface heat flux, and top surface heat transfer coefficient are transferred from face memory (F_UDMI) to cell memory (C_UDMI) for post-processing contours. Records continuity residual to file 'continuity_res.out'
DEFINE_ON_DEMAND	Collection of subroutines for UDF source code debugging, verification, and post-processing	Outputs cup dimensions. Displays surface averaged temperature values stored in memory. Prints interlaced wall heat flux and h_{Σ} profiles along the side wall and across the top surface

3.4 Results

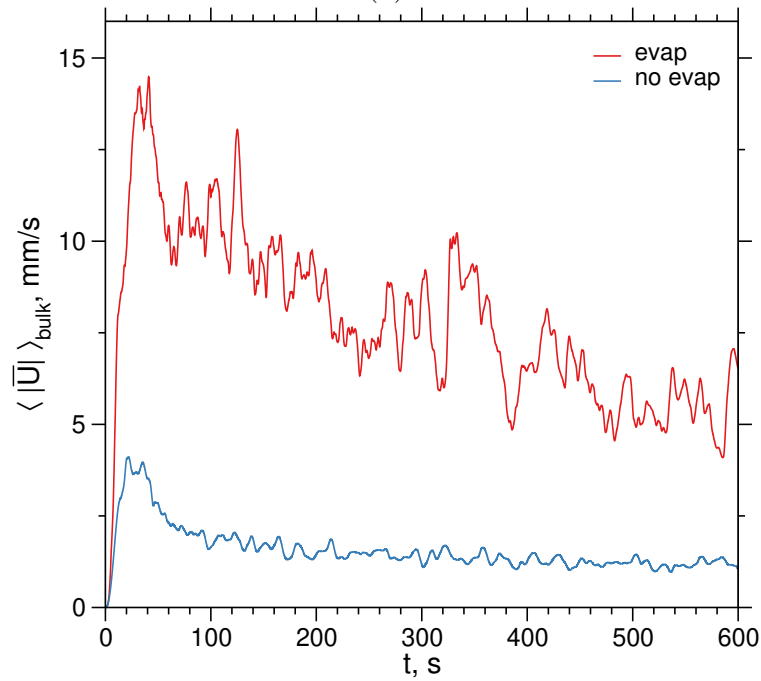
Based on the initial recorded bulk water temperature and the ambient air temperature during the experimental run, the corresponding qualities were input during the initialization of the CFD model. This enabled setting the precise initial flux at the side wall and initial heat transfer coefficient at the top surface. To first validate the experiment with the model, the local temperature data from thermocouples adhered to along the outer wall of the cup will be compared against the temperature probe readings of the three iso-surfaces. Although the experimental data was captured for an entire duration of 3600s (1 hour), our model was validated for the first 600s, when the temperature gradients were the highest. Additionally, the transient profile volume average velocity magnitude of the fluid bulk is scrutinized to study the influence of evaporative cooling on the hydrodynamics of the cup.

Fig.(3.6a) illustrates the temperature validation results. The experimental data is depicted as triangles, with symbols plotted in 15-second intervals for legibility. Comparing the profiles of the model-predicted point temperatures ($T_{i, \text{evap}}$) vs. the thermocouple recorded temperature symbols ($T_{i, \text{expt}}$), it is evident that the model agrees very well with the experiment. The temperature profiles of the three thermoelements considering evaporative-driven flows show a high degree of fluctuation. It may also be perceived that the temperature curves of the top, middle and bottom probes intersect at various times throughout the simulation time. This implies that the hottest layer in the cup dynamically oscillates due to the recirculation of water due to density gradients. The degree of fluctuation, irrespective of the probes, dwindles with time. On the other hand, when evaporative cooling is not considered, there is no intersection of the probe temperatures ($T_{i, \text{no evap}}$), resulting in the top layer predicted consistently warmer than the middle and bottom layers. The experimental data points show a higher degree of scatter which could be attributed to agitation due to the pouring of water into the cup. The model assumes the water to be motionless at $t = 0$.

A close-up of the first 10s of real-time simulation shows a rapid fall in the outer wall temperature readings from 94°C to about 86°C within the first 4 s. This is an artifact of initializing the entire computational domain at 94°C, which the solver quickly adjusts to satisfy the thermal resistance criterion of conduction through the paper wall. The tempera-



(a)



(b)

Figure 3.6: Time histories of the temperature and volume-averaged velocity. (a) T_1 , T_2 , and T_3 temperature profiles considering all pertinent heat transfer mechanisms and validation with experiment, evaluating the sensitivity of thermal profiles to the consideration of evaporation (b) Volume-averaged velocity, $\langle |\vec{U}| \rangle$, profile, cases considering and neglecting evaporative cooling

ture differential between the inner and outer walls of the paper may be calculated assuming constant wall thickness δ as follows:

$$T_{w,i} - T_{w,o} = \left(\frac{R_{w,i} \cdot q''_{\Sigma} \Big|_{(r=R_{w,o})}}{k_{wall}} \right) \ln \left(1 + \frac{\delta}{R_{w,i}} \right) \quad (3.15)$$

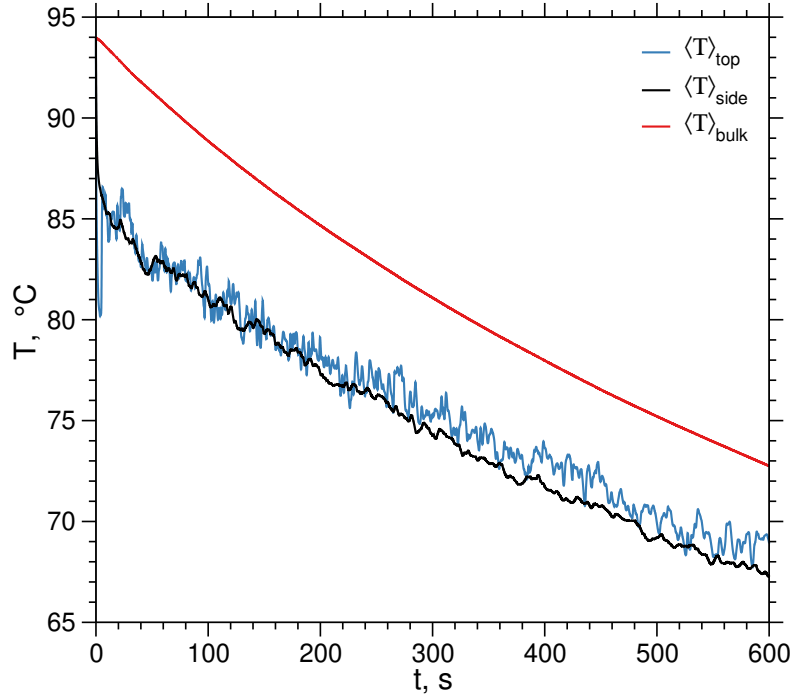
It is evident that this differential, $(T_{w,i} - T_{w,o}) \propto q''_{\Sigma} \Big|_{r=R_{w,o}}$. Note that this $q''_{\Sigma} \Big|_{r=R_{w,o}}$ may be referred to from Fig.(3.5a). As the cup cools down, the difference subsequently reduces.

Fig.(3.6b) illustrates the fluid bulk velocity magnitude profile ($\langle |\vec{U}| \rangle$ vs. t) for both instances when evaporative cooling is modeled (labeled ‘evap’) and neglected (labeled ‘no evap’). As the fluid in the cavity (cup) loses heat to the ambient and cools with time, the magnitude of the convective driving force and consequently $\langle |\vec{U}| \rangle$ reduces. Comparison of $\langle |\vec{U}| \rangle$ profiles with and without consideration of evaporation clearly depict the effect or the thermal boundary condition on the hydrodynamics of the bulk. The global maxima of the fluid bulk velocity magnitude for ‘evap’ and the ‘no evap’ cases is about $14.5 \frac{mm}{s}$ and $4.1 \frac{mm}{s}$, respectively. An interesting observation is that while the degree of fluctuation of $\langle |\vec{U}| \rangle$ for the ‘no evap’ case quickly diminishes and $\langle |\vec{U}| \rangle$ remains range bound around $1.5 \frac{mm}{s}$, in the ‘evap’ case, the fluctuations are far more acute and persistent. The first and second maxima and minima of the $\langle |\vec{U}| \rangle$ profile for the ‘evap’ case were identified and investigated further.

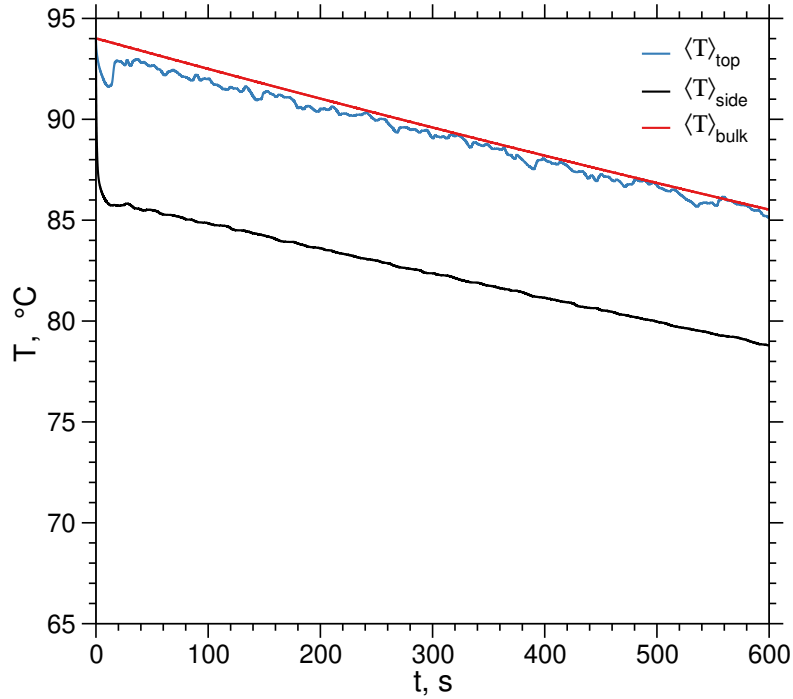
The mean ratio of the fluid bulk velocity magnitude of the case considering all pertinent heat transfer mechanisms to the case neglecting modeling evaporative cooling calculates to be roughly 5. This reduction parameter may directionally reinforce the significance of considering evaporative cooling on the flow characteristics and mesh quality. While the current study examines a 2D axisymmetric laminar flow, the mesh for potential future 3D LES simulations must be suitable fine such that global $y_{max}^+ \leq 1$. The selection of thermal boundary conditions on a cavity in an ambient fluid will establish a minimum threshold for the necessary control volume (CV) count.

Fig.(3.7) shows the time history of the integral quantities, $\langle T_{top} \rangle$, $\langle T_{side} \rangle$, and $\langle T_{bulk} \rangle$. Due to the 2D axisymmetry constraint imposed on the system, $\langle T_{side} \rangle$ and $\langle T_{top} \rangle$ reduce to line

integral averaged quantities calculated from Eq.(3.8) and Eq.(3.13), respectively.



(a)



(b)

Figure 3.7: Time history of the integral quantities, $\langle T \rangle_{top}$, $\langle T \rangle_{side}$, $\langle T \rangle_{bulk}$ for chosen mesh (104k cells). (a) Considering evaporation ('evap') (b) Neglecting evaporation ('no evap')

The volume average quantity $\langle T_{bulk} \rangle$ is reduced to a surface average and may be obtained from:

$$\langle T_{bulk} \rangle = \frac{\int_V T dV}{\int_V dV} = \frac{\sum_{N_f} T_i \Delta V_i}{\sum_{N_f} \Delta V_i} \quad (3.16)$$

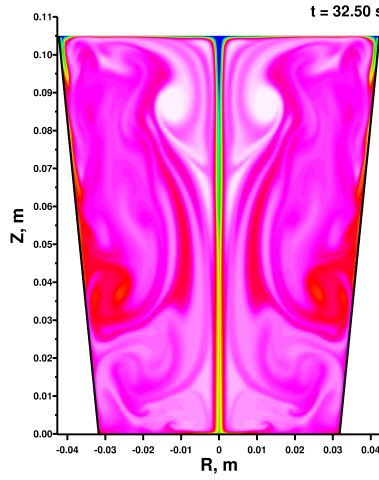
where T_i and ΔV_i are the temperature and volume of the i^{th} cell, and N_f is the total number of cells of the fluid (water) zone.

Fig.(3.7a) shows the results of considering all pertinent heat transfer mechanisms, including evaporation. In just 10 minutes of the real-time simulation, $\langle T_{bulk} \rangle$ drops steadily from 94°C to 72.7°C. Unlike the monotonic drop in bulk temperature, the top surface temperature, $\langle T_{top} \rangle$ shows a high degree of discontinuity due to the internal recirculation induced by rapid heat transfer with the colder air at the surface. As an artifact, $\langle T_{top} \rangle$ plummets to 80°C within 5 seconds of physical simulation time before an upward spike. The side outer temperature, $\langle T_{side} \rangle$, initially registers a sharp drop as the inner and outer wall temperatures reach dynamic equilibrium and then continues to cascade in an almost parallel fashion with $\langle T_{bulk} \rangle$.

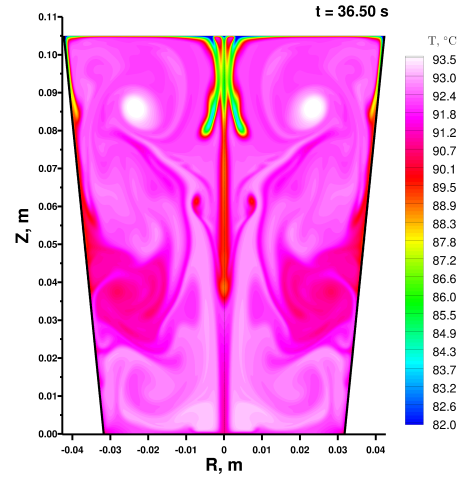
Fig.(3.7b) shows the results of the model solely neglecting evaporative cooling. During the 10 minutes of the real-time simulation, $\langle T_{bulk} \rangle$ drops much more gradually from 94°C to 85.5°C. $\langle T_{top} \rangle$ shows a much more gentle profile from before (‘evap’ case). A minor trough may be observed around 12s into the simulation. Throughout the simulation, $\langle T_{side} \rangle$ follows a similar slope profile as that of $\langle T_{bulk} \rangle$, separated by a consistent differential of 7-8°C.

An interesting observation comparing the above plots is that while for the ‘evap’ case, $\langle T_{top} \rangle$ fluctuates in the vicinity of $\langle T_{side} \rangle$, regarding the ‘noevap’ case, $\langle T_{top} \rangle$ lies in close proximity to the $\langle T_{bulk} \rangle$ profile.

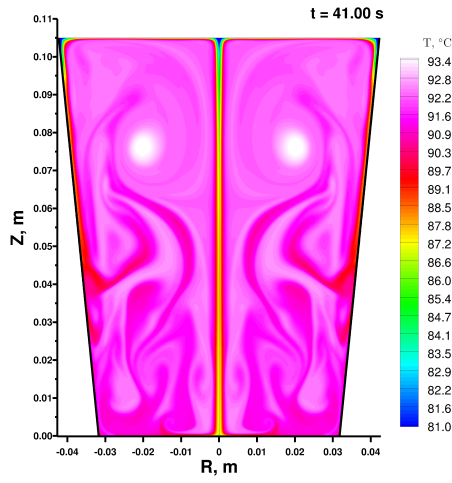
The two-dimensional field contours of temperature and velocity vectors will be analyzed next to showcase the insights possible by employing computational fluid dynamics. The aim is to visualize the spatiotemporal dynamics of the energy and momentum equations governing heat transfer from the hot cavity to the cool environment.



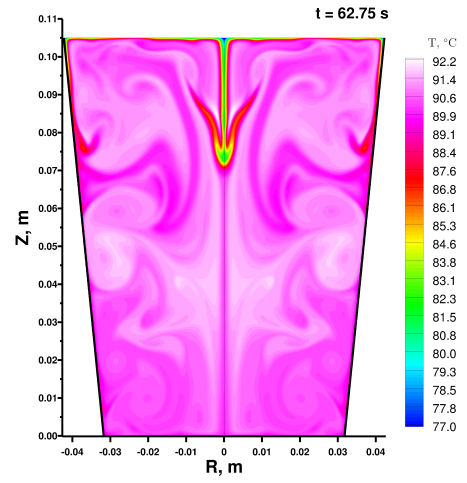
(a)



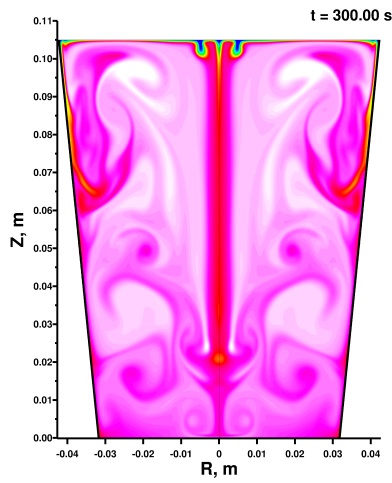
(b)



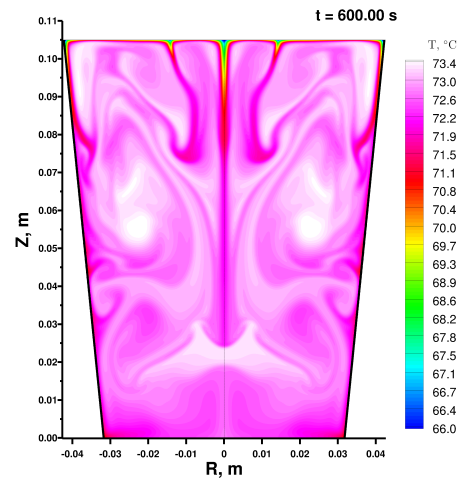
(c)



(d)



(e)



(f)

Figure 3.8: Temperature contours at different times

Contour plots in Fig.(3.8) clearly show how disturbed the temperature distribution becomes with time. Here, the cooling process starts from a uniform initial temperature of 94°C until the time of 600 seconds, with the corresponding profile illustrated in Fig.(3.8f). Fig.(3.8a) and (3.8b) capture the 2D temperature profile at 32.5 and 36.5 seconds, where the bulk fluid volume-averaged velocity magnitude reaches its first maximum and minimum points, respectively; similarly, Fig.(3.8c) and (3.8d) represent the contours at 41 and 62.75 seconds, which respectively show the second maximum and minimum points of the aforementioned velocity from Fig.(3.6). The temperature distribution at half of the experimental time is shown in Fig.(3.8e). Note that the heat transfer mechanisms in Fig.(3.8) involve evaporative cooling.

Initially, the water is at 94 °C. As time progresses, the temperature of the water decreases due to the accompanying heat transfer mechanisms. The rate of temperature decrease will be higher at the beginning when the temperature difference between the water and the surrounding environment is greater. Such behavior is mainly attributed to the evaporation process, as shown in Fig.(3.6) and Fig.(3.5b). As the temperature difference abates, the rate of cooling decreases as well.

Moreover, the temperature is always the lowest at the top surface, with the most significant temperature gradient there. Cooled water from the top surface either redistributes to the side wall or sinks to the bulk, caused by a higher density of colder water. It should be noted that the model used forces water to sink along the symmetry line.

At the side wall vicinity, the temperature towards it decreases rapidly due to the heat transfer to the ambient through the wall. Additionally, a sliding current of relatively cool water is delivered from the top surface. The current generally moves parallel to the walls, forming a major circulation at the initial stage. As time progresses, plummeting water's velocity decreases, and the circulation zone diminishes, inducing minor eddies' creation, as each time frame shows in Fig.(3.8).

Interestingly, due to the rotational motion of the eddy, the fluid can be isolated to some degree in the core of large eddies from the cooler surrounding fluid. As a result, a higher temperature maintains in the core of the eddy, especially if the eddy is formed in a region where the fluid was initially hotter, as can be seen in Fig.(3.8a), (3.8b), and (3.8c).

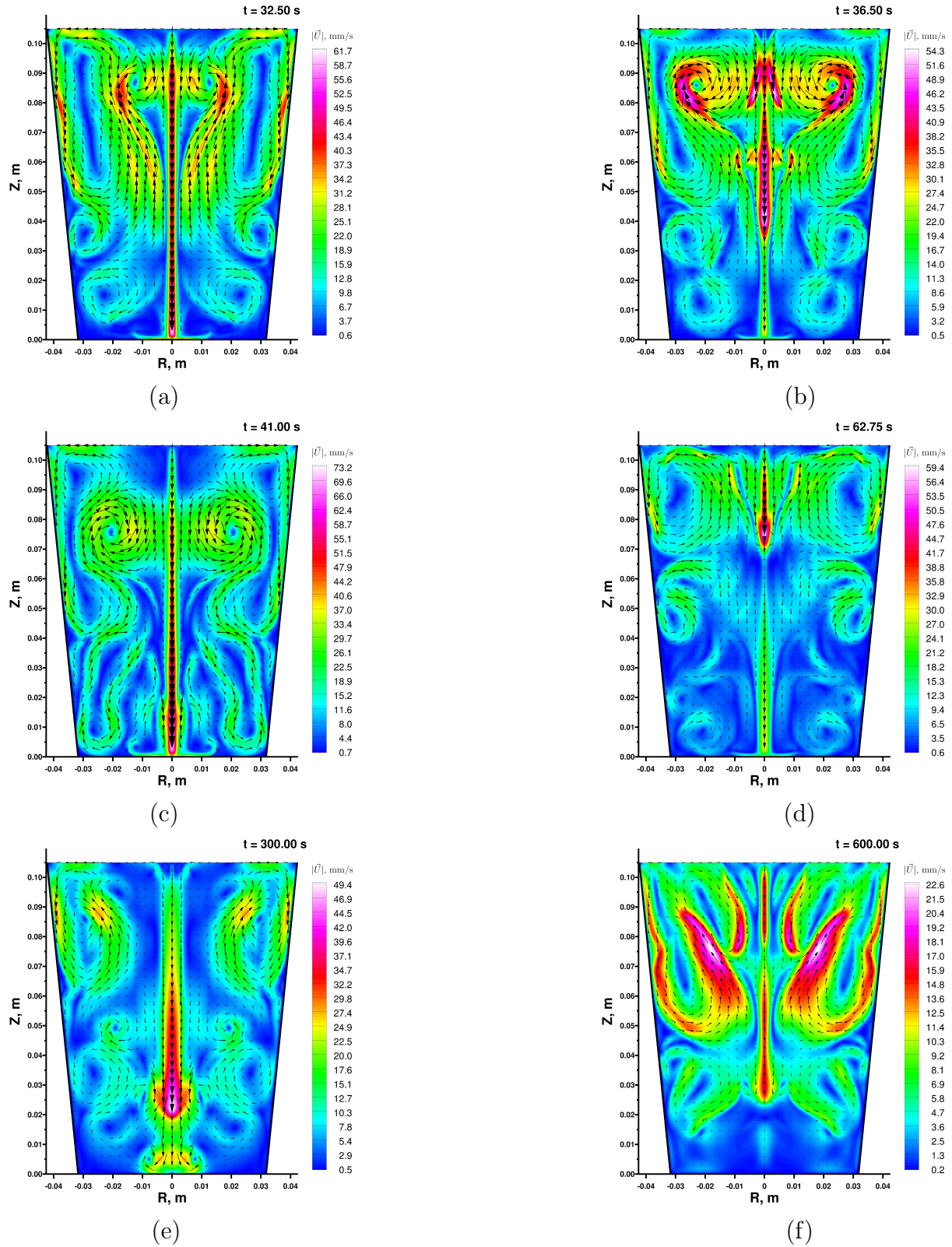


Figure 3.9: Velocity magnitude and vector contours at different times

For the same six time moments, the velocity magnitude and vector plot for the water cooling process is depicted in Fig.(3.9). The initial conditions of the simulation considered stagnant water.

The plot reveals a significant change in the velocity over the simulation period. Initially, the velocity magnitude is amplified, specifically near the top surface and side wall of the cup. Such a pattern is attributed to the more significant temperature gradients in these areas, which impel convection currents as the cooler water sinks and the warmer water rises, as already discussed for the temperature contours in Fig.(3.8). Velocity vectors clearly show the fluid’s rotational pattern. A common tendency for all time frames illustrated is larger eddies formations in the upper half of the cup. This is caused by conflicting cooler currents directed downwards from the top and rising warmer currents. The velocity magnitude decreases over time, consistent with the expectation and the pattern in Fig.(3.6). As the water temperature approaches the ambient air temperature, the driving force for the convection currents diminishes.

Finally, we want to emphasize some limitations of the proposed model. In particular, the 2D axisymmetric model places a constraint on flow within the cup. Flow in the azimuthal direction θ is disallowed, which is not the most accurate assumption. Although the cup geometry is symmetric (frustum), it does not guarantee hydrodynamic or thermal symmetry. Flow may be in the laminar regime, but eddies are to be expected in the azimuthal plane. This calls for a future study employing three-dimensional Large Eddy Simulations to capture flow patterns within the cup/cavity/chemical reactor more accurately. Care must be taken to generate a suitably fine grid in compliance with the $y^+ \leq 1$ criterion.

3.5 Conclusion

2D axisymmetric laminar flow modeling of a hot cavity surrounded by cold ambient was performed in the commercial CFD solver ANSYS Fluent v2022R2. Computational costs were not a constraint and permitted the use of a bounded second-order transient formulation discretization scheme. The application of thermal boundary conditions considering all pertinent heat transfer mechanisms was successfully implemented into the CFD solver through

an in-house developed UDF. In line with best practices in the CFD domain, both verification of the model with grid studies and alternate solvers (here, MATLAB) and validation of the model with experimental results were undertaken.

Insights from MATLAB code verification showed that throughout the temperature range of cooling of hot water in air, evaporative cooling could contribute upwards of 80% of the total heat loss from the free surface to the environment. For the side wall, it was determined that the radiative and convective heat fluxes were of the same order of magnitude and that both had to be considered in parallel for accurate heat transfer predictions. As heat fluxes were compared at the side wall and top surface, it is concluded that while cooling is predominantly top-driven and due to evaporative cooling, considering all pertinent heat transfer mechanisms was crucial for physical consistency. A comparison of our CFD model with experimental data demonstrated good agreement between the two. A sensitivity analysis of the evaporative cooling heat transfer mechanism substantiates that it is imperative to meticulously model evaporative cooling on the top water surface for accurate temperature profile determination.

Further, snapshots of the field contour plots of temperature and velocity shed visual insights into the thermal and hydrodynamic profiles. As the water cooled by heat loss to the cold ambient, it sunk at the centerline and along the wall to lower levels in the cup and rose elsewhere. Swirls were observed around the areas where the water is the hottest and flow stagnated, as may be confirmed by the velocity vectors around the points of simultaneous temperature at local maxima and velocity at local minima.

Thus, a UDF module capable of simulating the combined effects of natural convection, radiation, and evaporative cooling subject upon a hot cavity in an ambient fluid has been developed. The validated UDFs may be ported as a boundary condition for fixed beds, chemical reactors, and adsorption columns for improved prediction of thermal profiles in both lab-scale and industrial-scale units. The UDF opens up the possibility of simulating mixed convection, i.e., a combination of free and forced convection. Notably, there may exist other $Ra - Nu$ correlations in literature from the ones currently applied in this study that could yield slightly different results.

3.6 Addendum: LES modeling

In order to eliminate the axisymmetry constraint imposed in the prior 2D laminar flow model, three-dimensional (3D) Large Eddy Simulations (LES) were briefly investigated. The assumptions put forth in Sec.(3.2) and the thermophysical properties of water are retained. The boundary conditions in the LES are defined similarly to those used in the 2D laminar flow model.

LES Transport equations

The transport equations for mass, momentum, and energy transport are given in Eq.(3.17 – 3.19) respectively.

$$\frac{\partial \rho}{\partial t} + \frac{\partial}{\partial x_j} (\rho \bar{u}_i) = 0 \quad (3.17)$$

$$\frac{\partial \bar{u}_i}{\partial t} + \bar{u}_j \frac{\partial \bar{u}_i}{\partial x_j} = -\frac{1}{\rho} \frac{\partial \bar{p}}{\partial x_i} + \frac{\partial}{\partial x_j} \left(v \frac{\partial \bar{u}_i}{\partial x_j} + \frac{1}{\rho} \frac{\partial \tau_{ij}}{\partial x_j} \right) \quad (3.18)$$

$$\frac{\partial}{\partial t} (\rho E) + \frac{\partial}{\partial x_j} (u_i (\rho E + p)) = \frac{\partial}{\partial x_j} \left(k_{eff} \frac{\partial T}{\partial x_i} \right) \quad (3.19)$$

where,

$$E = \frac{u^2}{2} - \frac{p}{\rho} + \int_{T_{ref}}^T C_p dT$$

Eq. (3.19) accounts for the total energy, including the kinetic and potential energy and enthalpy. The term, τ_{ij} , in Eq. (3.18) results from the filtering operation and denotes the sub-grid scale (SGS) stress. τ_{ij} relates the resolved flow with the sub-grid-scale motion and is modeled considering the Boussinesq hypothesis as per Eq. (3.20).

$$\tau_{ij} = \frac{1}{3} \tau_{kk} \delta_{ij} - 2\mu_t \bar{S}_{ij} \quad (3.20)$$

where μ_t is the subgrid-scale turbulent viscosity. The isotropic part of the subgrid-scale stresses τ_{kk} is not modeled but clubbed in the filtered static pressure term. \bar{S}_{ij} is the rate-

of-strain tensor for the resolved scale defined by

$$\bar{S}_{ij} \equiv \frac{1}{2} \left(\frac{\partial \bar{u}_i}{\partial x_j} + \frac{\partial \bar{u}_j}{\partial x_i} \right)$$

In this work, we employ the Wall-Adapting Local Eddy-Viscosity (WALE) subgrid scale model^[152], wherein the eddy-viscosity, μ_t , is modeled by:

$$\mu_t = \rho L_s^2 \frac{(S_{ij}^d S_{ji}^d)^{3/2}}{(\bar{S}_{ij} \bar{S}_{ji})^{5/2} + (\bar{S}_{ij}^d \bar{S}_{ji}^d)^{5/4}} \quad (3.21)$$

wherein L_s , the mixing length for subgrid scales, and S_{ij}^d are computed as per

$$\begin{aligned} L_s &= \min(kd, C_w V^{1/3}) \\ S_{ij}^d &= \frac{1}{2} (\bar{g}_{ij}^2 + \bar{g}_{ji}^2) - \frac{1}{3} \delta_{ij} \bar{g}_{kk}^2 \\ \bar{g}_{ij} &= \frac{\partial \bar{u}_i}{\partial x_j} \end{aligned}$$

wherein $\kappa = 0.41$ is the von Kármán constant, d is the distance to the closest wall, C_w is the WALE constant, and V is the computational cell volume. The WALE model has been demonstrated to provide the correct wall asymptotic behavior for wall-bounded problems. It also returns zero turbulent viscosity for laminar flows, unlike the Smagorinsky-Lilly model^[153], resulting ideal for this study. Although [Nicoud and Ducros](#) proposed a value of 0.5 for C_w , the commercial package's default C_s value of 0.325, found to be the most widely applicable, is used here. Additional details regarding the model expressions and constants may be found in the ANSYS Fluent Theory Guide^[128] and in [Nicoud and Ducros](#)' work^[152].

LES Numerics

The details of the models and schemes applicable in LES modeling are laid out in Table 3.5.

A 1.2 million control volume 3D mesh with three levels of local refinement at the side inner wall, top surface, and base is generated [Refer to Fig.(3.10)].

Table 3.5: List of models and schemes^[151] used in the 3D LES CFD model

<i>Name</i>	<i>Model/ Scheme Name</i>
Solver	Steady State, Pressure-Based
Flow Model	Large Eddy Simulation
Sub-grid Scale Model	WALE
Pressure–Velocity Coupling	SIMPLE ^[126]
Spatial Discretization – Gradient	Least Squares Cell-Based
Spatial Discretization – Pressure	Second Order
Spatial Discretization – All Equations	Bounded Central Differencing
BCD Scheme Boundedness	1
Transient Formulation	Bounded Second Order Implicit

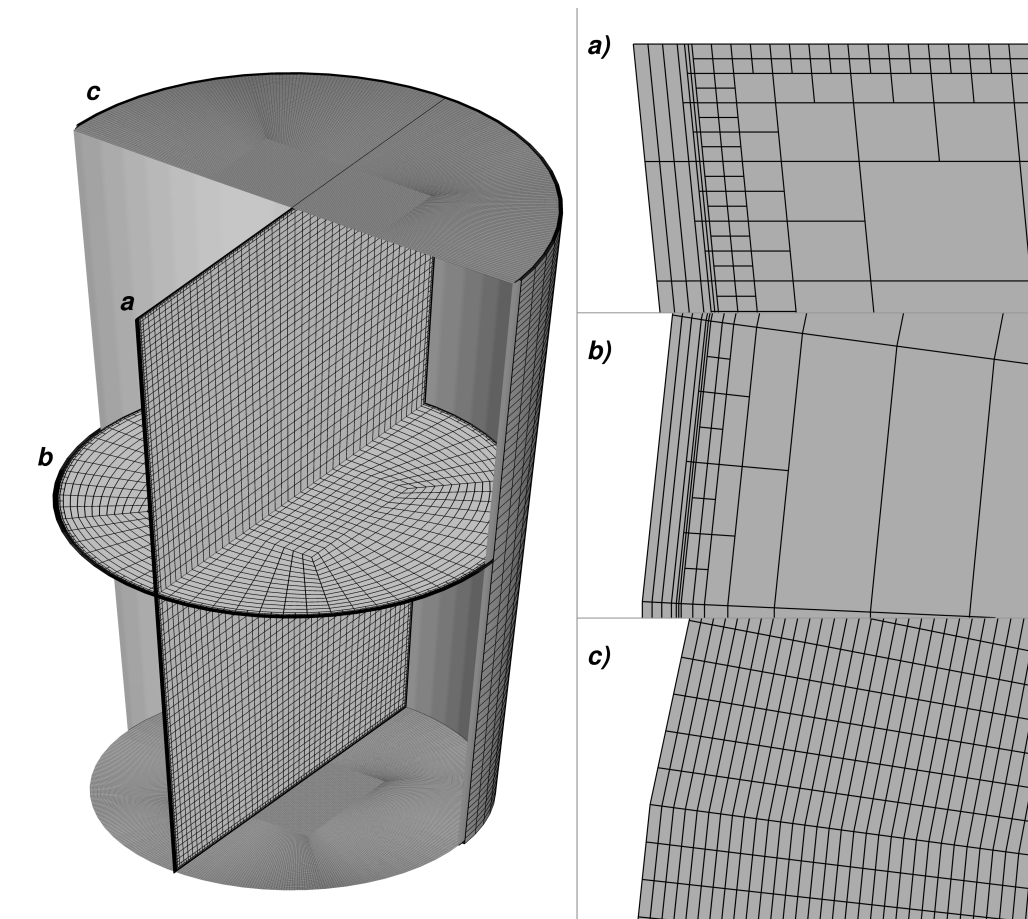


Figure 3.10: 3D mesh with three levels of local refinement

Further mesh refinement was avoided owing to 3D LES simulations requiring significant computational time (order of weeks) and data storage facility (order of terabytes of memory) for post-processing. The time step is fixed and equals $\Delta t = 0.025$ s. The maximum number of iterations per time step is set at 80, with the convergence criterion requiring all residuals falling to $< 10^{-6}$.

The UDF source code had to be slightly modified to correctly account for the difference in the calculation of thermal resistance and surface and volume averages in 2D and 3D.

LES Results

The procedure followed in the prior 2D laminar flow model was replicated during 3D LES simulations.

The transient temperature profiles of the T_1 , T_2 , and T_3 thermoelements were compared against the respective iso-surface line-averaged temperature probe readings for validation purposes. It is clearly evident that 3D LES results are superior to the 2D laminar flow results with excellent agreement and attenuated fluctuation in the model prediction, as evident in Fig.(3.11).

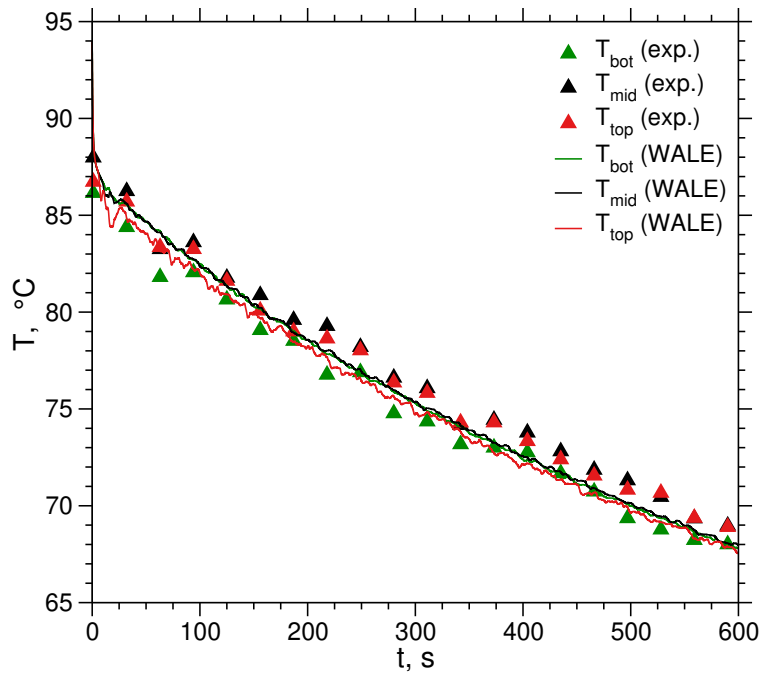


Figure 3.11: LES Validation: Time histories of T_1 , T_2 , and T_3 considering all pertinent heat transfer mechanisms and validation with experiment

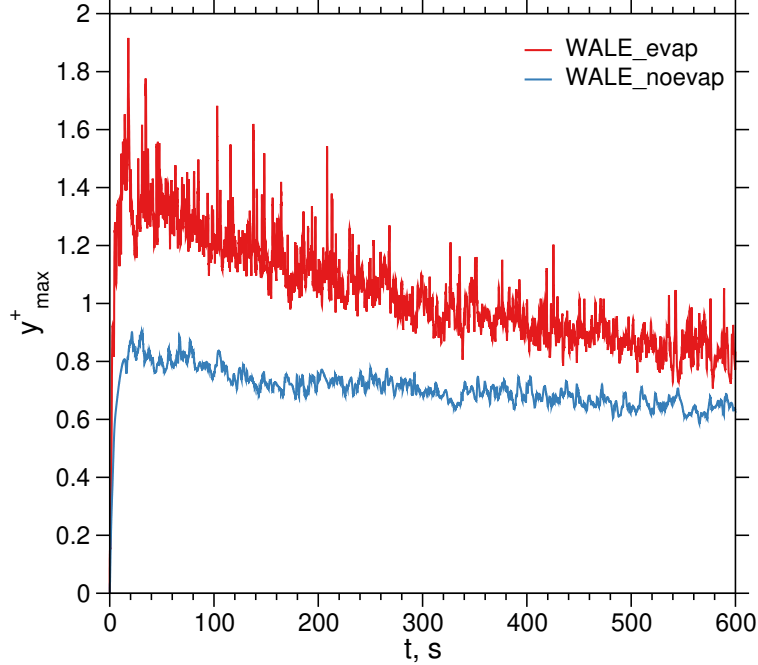


Figure 3.12: y^+ profile and sensitivity to thermal boundary conditions employed

The y^+ time history was also studied, and from Fig.(3.12), it is demonstrated that the choice of the implemented thermal boundary condition may affect the grid refinement requirements. Considering evaporative cooling induces a more pronounced unsteady flow character, with the maximum y^+ value recorded circa 1.9. The current grid would require further local refinement to meet the benchmark $y^+ \leq 1.0$ criterion. An inadequacy of computational resources is asserted as the reason for curtailing supplemental investigation and calls for future reappraisal.

Lastly, to demonstrate inherent thermal and hydrodynamic instability in a symmetrical geometry with a uniformly initialized, seemingly laminar flow system, a snapshot of the isometric view of temperature contours is shown in Fig.(3.13). The eddies and swirls on the top surface as well as the asymmetry within the core of the bulk fluid, reinforce the notion of the salience of the WALE LES flow model in chemical reactors and similar wall-bounded systems.

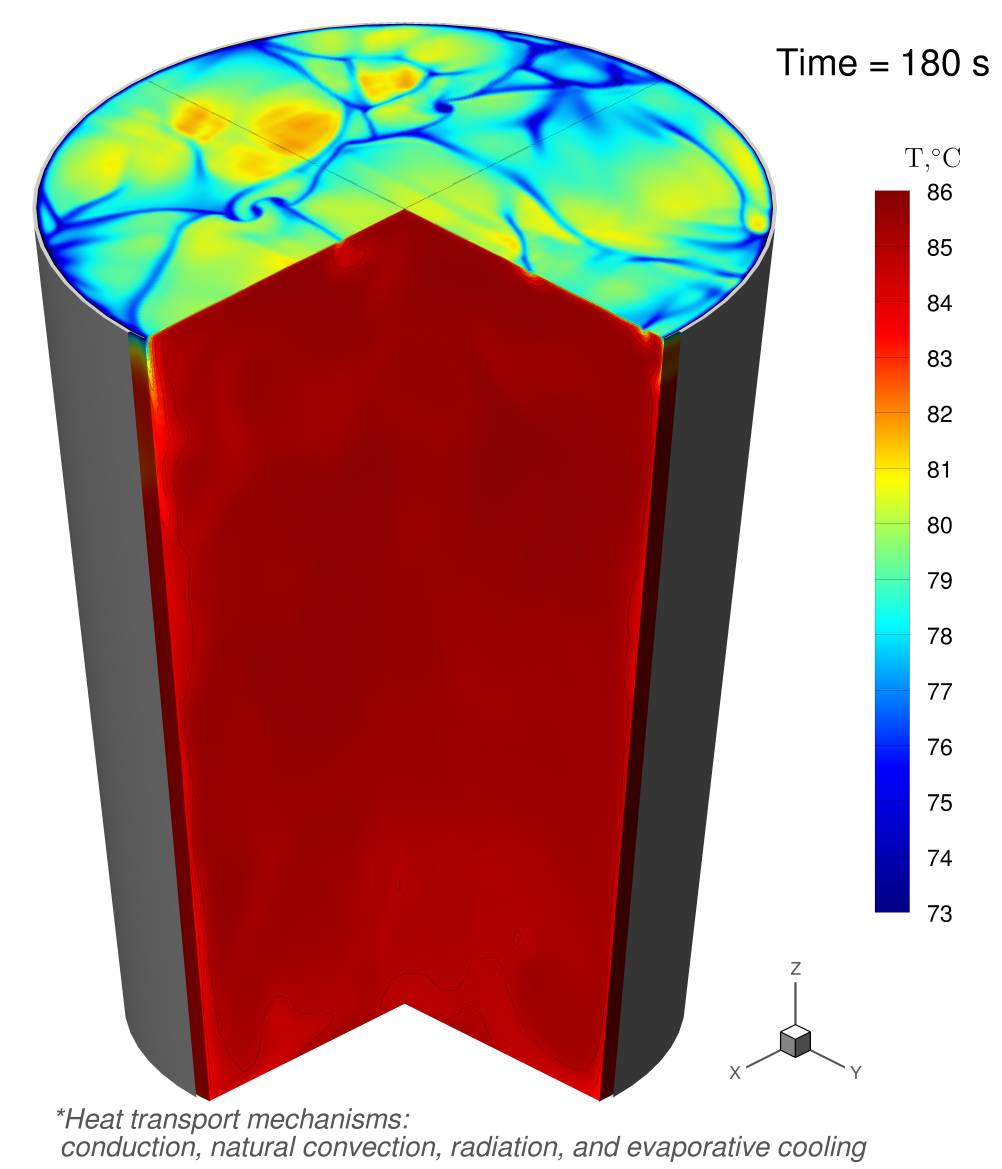


Figure 3.13: Snapshot of the isometric view of the temperature contours at $t = 180s$

Acknowledgements

The authors would like to thank Prof. Arvind Rajendran, the Principal Investigator of the Lab of Advanced Separation Processes (UAlberta), for providing the necessary laboratory equipment and Dr. James A. Sawada for his valuable support with the experimental setup and data logging.

Chapter 4

Implementation and validation of boundary conditions between adsorption columns and ambient air

4.1 Introduction

As seen in Chapter 3, applying the appropriate wall thermal boundary conditions (BCs) on the chemical reactor or adsorber is necessary to close the energy balance with the ambient. The nature and extent of heat dissipation influence the key performance indicators of an adsorption cycle, namely purity and recovery. Adsorption processes are almost always exothermic, and this released heat must be dissipated through the adsorbent to the wall and then the ambient. There are three categories that researchers have classified modeling of the wall energy balance in terms of the BCs, listed as follows:

1. Adiabatic: When there is no heat loss from the column to the surroundings. This may be achieved in laboratory setups by using insulation such as fiberglass or a non-convective refractory material around the column^[73]. [Wilkins et al.](#)^[38] postulate that industrial adsorption columns operate very close to adiabatic conditions. This BC is expressed as:

$$-k_w \left. \frac{\partial T_w}{\partial n} \right|_w = 0 \quad \text{OR} \quad h_{out} = 0 \quad (4.1)$$

2. Isothermal: This may be understood as near rapid equilibration of wall temperature to the ambient temperature. This boundary condition may be attained by immersing the column in a water bath, as illustrated by [Wilkins et al.](#)^[38]. Numerically, this BC is stated as follows:

$$T_w = T_\infty \quad \text{OR} \quad h_{out} \rightarrow \infty [O(\sim 10^3)] \quad (4.2)$$

Application of this BC is common in chemical reactors wherein the maximum selectivity may be achieved when there are negligible temperature gradients throughout the reactors. In shell and tube reactors, for example, boiling water may be used as the external heat transfer fluid (HTF) surrounding the tubes (packed beds). An example of this scenario is seen in the work by [Das et al.](#)^[64].

3. Non-isothermal: This case is the most physically-realistic consideration. The heat flux through the outer wall to the ambient is posited to depend on the wall and ambient temperatures. The radiative component depends purely on the local temperature, whereas the convective component depends on the particular $Nu - Ra$ correlation and the reductive surface area-averaged temperature. Mathematically, this BC may be represented as either the convective heat transfer between the wall surface and ambient (Robin BC) or using the wall heat flux BC:

$$-k_w \frac{\partial T_w}{\partial n} \Big|_w = q''_\Sigma = h_\Sigma (T_w - T_\infty) \quad (4.3)$$

$$h_\Sigma = h_{conv} + h_{rad} \quad (4.4)$$

$$h_{rad} \equiv \text{Eq. (3.5)} \quad (4.5)$$

$$h_{conv} \equiv \text{Eq. (3.6 - 3.8)} \quad (4.6)$$

The Pareto plots for Purity vs. Recovery discussed in most adsorption works indicate that the isothermal BC is the most optimistic while the adiabatic BC is the most conservative, with the non-isothermal BC bound within the extremes.

[Wilkins and Rajendran](#)^[57], in their 1D DCB study measuring competitive adsorption of

CO₂ and N₂ fit the value of the external heat transfer coefficient, h_{out} , to $10 \frac{W}{m^2.K}$. This was done by matching the thermal breakthrough profiles of pure CO₂ experiments. However, this value is not expected to remain constant over different feed compositions.

Ward and Pini^[82] attempted to perform an optimization to obtain the outer heat transfer coefficient h_{out} for single component DCB experiments. They integrated the technique of Bayesian inference for uncertainty quantification with the method of Sobol indices for sensitivity analysis. Ranging between ($\sim 0.1, \sim 16$) $\frac{W}{m^2.K}$ with a 95% credibility interval (CI), h_{out} showed high degree of uncertainty. Analysis of its Sobol sensitivity index indicated that h_{out} had negligible influence on the model output. Therefore, it was concluded that the 1D model was insensitive to h_{out} under the specified experimental conditions and could not accurately predict the value of h_{out} .

Gautier et al.^[75] performed 3D CFD simulations assessing the numerical sensitivity of parameters influencing the heat and mass transfer in porous media in a PSA cycle. They assumed three arbitrary invariant values of the external heat transfer coefficient, $h_{out} \in \{20, 55, 110\} \frac{W}{m^2.K}$. h_{out} was suggested to considerably influence exterior bed surface temperature prediction and, thereby, adsorption capacity in internal bed zones adjacent to the bed walls. This seemingly contradicts the findings by Ward and Pini^[82], and it may be surmised that multidimensional (2D and 3D) simulations are appreciably more sensitive to this parameter than uni-dimensional models.

Dantas et al.^[73], in their modeling study on PSA-based CO₂ / N₂ separation in a fixed bed packed with zeolite 13X used the following correlation for obtaining the wall-ambient heat transfer coefficient. They carried out finite element method simulations on the gPROMS commercial package.

$$\overline{Nu}_{conv} = 0.68 + \frac{0.67Ra^{1/4}}{\left[1 + \left(\frac{0.492}{Pr}\right)^{9/12}\right]^{4/9}} \quad (4.7)$$

However, they did not discriminate between the surface average and local temperature in the calculation of the Rayleigh number.

Qasem and Ben-Mansour^[72] employed a non-isothermal BC approach but they used the $Nu - Ra$ correlation for long horizontal cylinders proposed by Churchill and Chu^[154].

However, most adsorption cycles operate with vertical columns. Also, it has not been clarified how the local and surface-averaged temperatures were incorporated or whether UDFs were developed for the side-wall thermal boundary condition. Thus, our work demonstrates the implementation of a physically-sound coupled natural convection and radiation thermal BC to accurately resolve the side-wall energy balance in our CFD simulations.

First, we shall familiarize the reader with the thermal-electric analogy concerning flow potential. Then the heat transfer formulation and the thermal resistance network pertinent to fixed beds shall be delineated. Finally, we shall discuss the results of 2D dynamic column breakthrough simulations employing the in-house designed UDF code for natural convection in vertical adsorption columns.

4.2 Thermal – Electric Analogy

Heat transfer across a temperature gradient ΔT could be treated analogously to the flow of current across a voltage gradient ΔV .

Table 4.1: Thermal-Electric Analogy

Parameter	Current Flow	Heat Transfer
Potential	Voltage V	Temperature T
Extensive Flow	Charge Q	Heat Q_{th}
Intensive Flow	Current i	Heat rate q
Resistance	Ohmic resistance $R = \frac{\Delta V}{i}$	Thermal resistance $R_{th} = \frac{\Delta T}{q}$

Circuit theory in Ohmic resistances may be adapted to thermal resistance networks.

$$R_{eq,series} = \sum_{i=1} R_i \quad (4.8a)$$

$$R_{eq,parallel}^{-1} = \sum_{i=1} R_i^{-1} \quad (4.8b)$$

Thermal resistances in series are additive in the sense that the same heat rate, q , flows through resistances in series. Thermal resistances are inversely additive in parallel since the temperature gradient, ΔT , is the same across resistances in parallel.

4.3 Natural Convection in Adsorption Columns — Heat transfer formulation

Consider an adsorption column as shown in Fig.(4.1). Air, or any gas mixture, enters the porous bed of height H . The bed wall has a finite thickness, δ , given by the difference in the wall inner and outer radii, $R_{w,i}$ and $R_{w,o}$, respectively. Due to heat released during adsorption, \dot{Q}_{gen} , the column and wall temperature start increasing. Heat is emanated via the wall through conduction, after which the convective and radiative fluxes dissipate heat to the free stream.

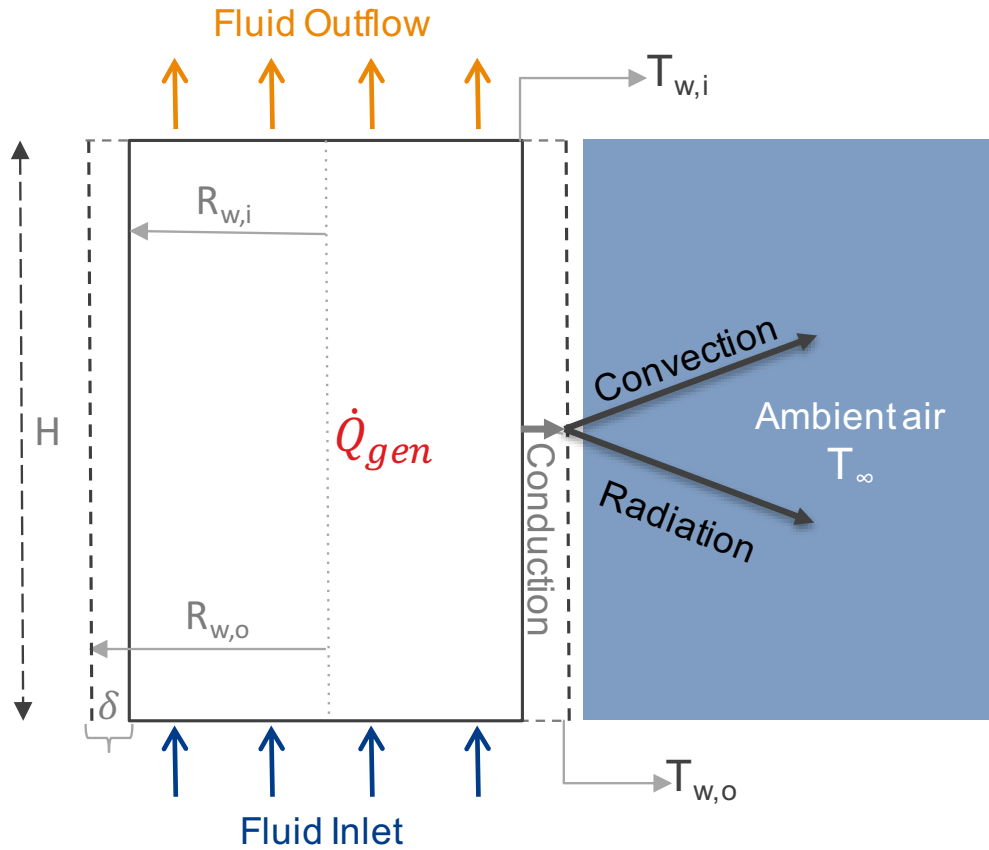


Figure 4.1: Schematic of heat transfer across the wall and free stream in an adsorption column
 $(\dot{Q}_{gen} \equiv \text{Heat of adsorption}; i - \text{inner}, o - \text{outer}, w - \text{wall})$

Fig.4.2 illustrates the thermal resistance network across the bed-wall-ambient. The heat rate across the inner wall and the ambient for a given control volume dz , $q_w = \frac{T_{w,i} - T_{\infty}}{R_{eq}}$.

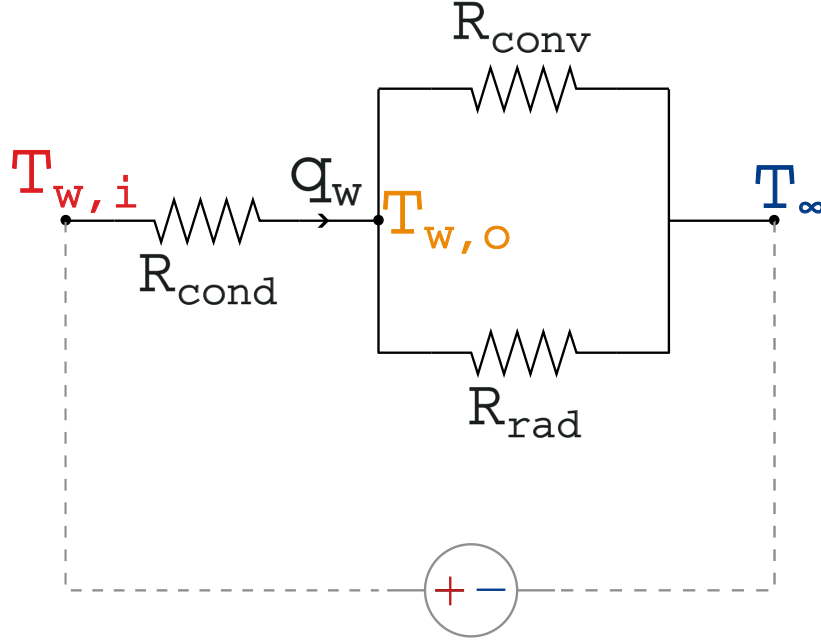


Figure 4.2: Thermal resistance network in a fixed bed

$$\text{Equivalent thermal resistance, } R_{eq} = R_{cond} + R_{conv||rad} \quad (4.9)$$

where,

$$R_{cond} = \frac{\ln(r_{w,o}/r_{w,i})}{2\pi \cdot dz \cdot k_{wall}} \quad (4.10a)$$

$$R_{conv||rad} = \frac{1}{2\pi \cdot r_{w,o} \cdot dz \cdot h_{\Sigma}} \quad (4.10b)$$

where,

$$h_{\Sigma} = h_{conv} + h_{rad} \quad (4.11a)$$

$$h_{rad} = \sigma \epsilon_{wall} (T_{w,o} + T_{\infty})(T_{w,o}^2 + T_{\infty}^2) \quad (4.11b)$$

$$h_{conv} = \frac{\overline{Nu}_{conv} \cdot k_{\infty}}{H} \quad (4.11c)$$

where,

$$\overline{Nu}_{conv} = \left(0.825 + \frac{0.387Ra^{1/6}}{\left[1 + \left(\frac{0.492}{Pr} \right)^{9/16} \right]^{8/27}} \right)^2 \quad (4.12a)$$

$$Ra = \frac{g\beta (\langle T_{side} \rangle - T_\infty) H^3}{\alpha_\infty \nu_\infty} \quad (4.12b)$$

$$\langle T_{side} \rangle = \frac{\int_S T_{w,o} dS}{\int_S dS} = \frac{\sum_{N_w} T_{(w,o),i} \Delta S_i}{\sum_{N_w} \Delta S_i} \quad (4.12c)$$

Iteratively solve $q_w = A_s h_{conv}(T_{w,o} - T_\infty) + A_s \epsilon_{wall} \sigma(T_{w,o}^4 - T_\infty^4) = \frac{T_{w,i} - T_\infty}{R_{cond} + R_{conv||rad}}$ to determine the outer wall temperature, $T_{w,o}$, for a given inner wall temperature, $T_{w,i}$, satisfying the above constraints. The total heat transfer coefficient, h_Σ , and the wall heat rate, q_w , are simultaneously obtained. From q_w , the wall heat flux q_w'' may be quickly returned. The dependence of the overall heat transfer from the wall to the ambient on both the local temperature, $T_{w,o}$, and side-wall area-averaged temperature, $\langle T_{side} \rangle$, is established.

In the 2D axisymmetric flow model considered in Fluent, the natural convection boundary condition was implemented at the wall of the fixed bed. A UDF was created that takes the inner wall temperature as input and returns the heat transfer coefficient profile ($h_\Sigma [\equiv h_o]$ vs z) along the bed. We employ Newton's method since the function F and its derivative F' are analytical functions. The calculations are looped until the relative estimated error in the variable $T_{w,i}$ and the absolute value of the function F is below a specified tolerance ϵ .

$$F = \frac{T_{w,i} - T_\infty}{R_{eq}} - A_s h_{conv}(T_{w,o} - T_\infty) - A_s \epsilon_{wall} \sigma(T_{w,o}^4 - T_\infty^4) = 0 \quad (4.13a)$$

$$F' = -A_s h_{conv} - A_s \epsilon_{wall} \sigma(4 \cdot T_{w,o}^3) \quad (4.13b)$$

A_s is the outer surface area of the wall control element with length dz , given by $A_s = 2\pi r_{w,o} dz$.

The code, developed in C, could be and has been migrated to MATLAB as a standalone function in 1D process models to allow for temperature-dependent wall-ambient heat transfer coefficient calculation during transient state analyses.

4.4 Results of 2D DCB simulations

The UDF framework developed by Fabian et al.^[155] was used to simulate the transport equations involved in binary gas dynamic column breakthrough (DCB) in a 2D axisymmetric fixed bed within the porous media model framework, as shown in Fig.(4.3). A schematic representation of the column domain in Fluent is shown in Fig.(4.4).

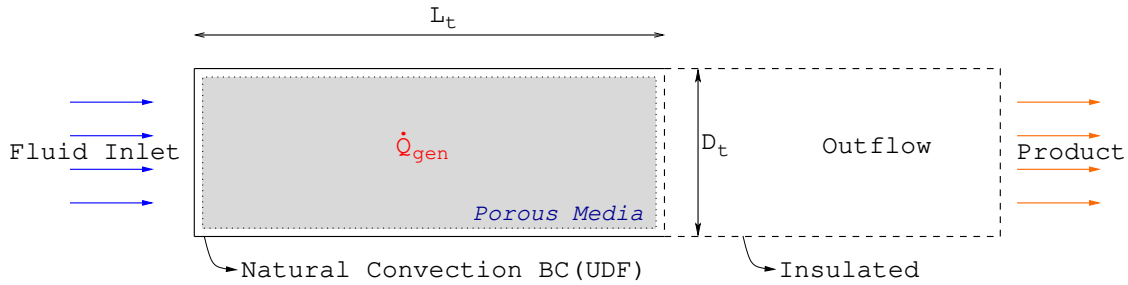


Figure 4.3: Simplified schematic of the adsorption column for DCB simulations wherein the natural convection boundary condition is applied

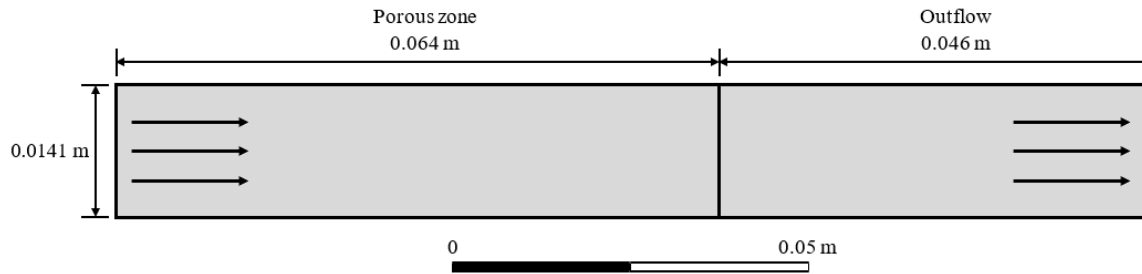


Figure 4.4: 2D axisymmetric computational domain of the adsorption column

The natural convection boundary condition is applied only on the porous zone wall, and the outflow zone wall is insulated. The ‘Outflow’ zone is incorporated such that the outflow boundary condition (symmetry in the flow direction) does not influence hydrodynamics and thermal transport phenomena at the actual exit of the column, ensuring accuracy and stability. A salient feature of the UDF was the relatively easy transferability to any **adsorbate/carrier combination** such as CO_2/N_2 , CO_2/He , N_2/He etc., **the same code is used, and the only changes correspond to isotherm parameters and experimental conditions**. Concurrently, the UDF source code developed for the natural convection-driven free stream heat transfer is modular and was patched atop the UDF developed by Fabian et al.^[155].

Multidimensional CFD simulations do not require the internal heat transfer coefficient, h_i , to be input a priori. The porous media model implicitly calculates h_i from the temperature gradient at the wall. Fig.(4.5) compares the numerically predicted wall-fluid convective heat transfer coefficient, h_i , obtained from both the porous media model (PMM) and the particle resolved CFD (PRCFD) approaches vis-à-vis the correlation posited by Yagi and Wakao^[92]. The above calculations were done for a system wherein $\frac{k_s}{k_f} = 1$. h_i determined from 2D and 3D PMM calculations almost overlap, as is to be expected. In the range of flow rates in laboratory experiment testing, ($Re_p \approx 1$), it is evident that the value of h_i from either the PRCFD or the PMM approaches is similar.

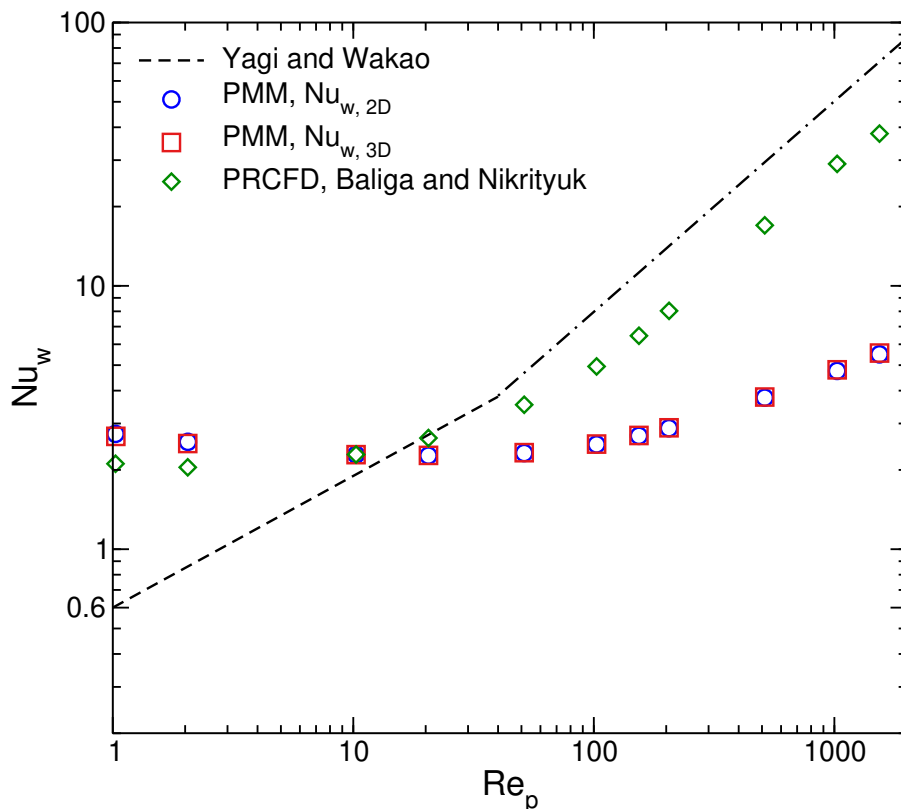


Figure 4.5: Wall-fluid heat transfer coefficient, h_i , determined from the porous media model (PMM) and the PRCFD analysis in Chapter 2, compared with Yagi and Wakao^[92]. All data points refer to the case $(\frac{k_s}{k_f}) = 1$

In this study, two pairs of adsorbate systems were considered. In both cases, the carrier gas is Helium. The in situ gas within the column at the start of the DCB runs is also Helium. The value of the effective gas thermal conductivity in the porous media was reported by

Table 4.2: Laboratory rig column characteristics

Parameter	Symbol	Value
Tube length	L_t	6.40 cm
Tube inner diameter	D_t	2.82 cm
Wall thickness	δ	0.18 cm
Mean particle diameter	D_p	0.1 cm
Bed porosity	ε_b	0.40
Column wall emissivity	ϵ_{wall}	0.96

Table 4.3: Parameters used for CFD-based adsorption framework developed by Fabian et al. [155]

Property	Value / Method	Unit
Column wall density, ρ_w	8030	kg/m ³
Column wall specific heat capacity, $C_{p,w}$	502.48	J/kg·K
Column wall conductivity, k_w	16.27	W/m·K
Adsorbent tortuosity, τ	3	Dimensionless
Adsorbent porosity, ε_p	0.35	Dimensionless
Adsorbent density, ρ_p	1050	kg/m ³
Adsorbent specific heat capacity, $C_{p,p}$	856	J/kg·K
Adsorbent conductivity, k_s	0.3	W/m·K
Fluid phase (gas mixture) density, ρ_g	incompressible ideal gas	kg/m ³
Fluid phase specific heat capacity, C_p	mass-weighted mixing law	J/kg·K
Fluid phase conductivity, k_f	mass-weighted mixing law	W/m·K
Fluid phase viscosity, μ_g	mass-weighted mixing law	Pa·s
Pure gas specific heat capacity	polynomial function of T	J/kg·K
Pure gas conductivity	polynomial function of T	W/m·K
Pure gas viscosity	kinetic theory	Pa·s
Molecular diffusivity, D_m	Fuller [Equation (1.20)]	m ² /s
Dispersion coefficient, D_L	Equation (1.22a)	m ² /s
Effective conductivity, k_{eff}	0.19, Equation (1.25)	W/m·K
Adsorbed phase specific heat capacity, $C_{p,a}$	As per Fabian et al. [155]	J/kg·K
Wall-ambient heat transfer coefficient, h_o	UDF – Patched	W/m ² ·K

Wilkins and Rajendran [57] as $k_{eff} = 0.19 \frac{W}{m \cdot K}$. From Eq.(1.25), the solid thermal conductivity is back-calculated to be $\sim 0.3 \frac{W}{m \cdot K}$. A thermocouple is wedged into the column at about 80% of the axial bed length. It is considered that the thermocouple logs the temperature at the centerline of the bed. Note that for either system, the thermal breakthrough requires a longer time than the composition breakthrough of the corresponding system.

Table 4.4: Free stream (ambient air) properties used in the natural convection driven heat transfer UDF

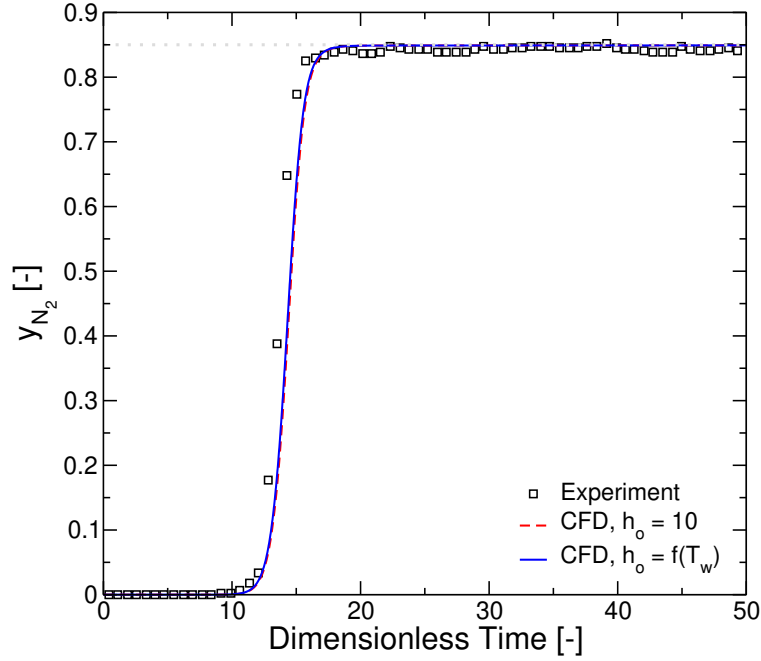
Free stream property	Value	Unit
Thermal conductivity, k_{inf}	0.0242	W/m·K
Thermal diffusivity, α_{air}	2.170×10^{-5}	m ² /s
Kinematic viscosity, μ_{air}	1.506×10^{-5}	m ² /s
Prantdl number, Pr	0.708	Dimensionless

Case 1: Nitrogen / Helium

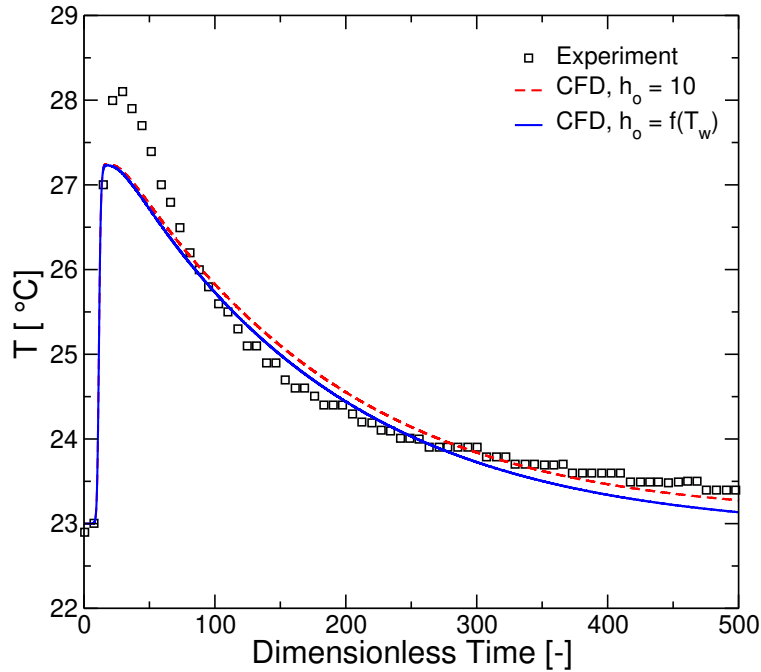
An 85 mol.% N₂ – 15 mol.% He system was considered. The ambient temperature, $T_\infty = 23^\circ\text{C}$. A flow rate, Q_{in} , of 350 standard cubic centimeters per minute (sccm) of the gas mixture was used. The superficial velocity, u_{in} , and the interstitial velocity, v_0 , may thus be calculated correspondingly. The dimensionless time, t_0 , is calculated as the ratio of the bed length to the interstitial velocity.

$$t_0 = L_t/v_0 = 2.741 \text{ s} \quad (4.14)$$

From Fig.4.6a and 4.6b, we observed an excellent agreement between experimental data and the results predicted with our adsorption framework CFD model patched with the natural convection heat transfer coefficient UDF. Regarding the constant and temperature-dependent external heat transfer coefficient BC scenarios for the 85 mol.% N₂ – 15 mol.% He system, the N₂ composition breakthrough curves majorly overlap. In the temperature breakthrough analysis, both CFD BC simulations result in a roughly 0.9°C underprediction vis-à-vis experiment. The difference in peak temperature in the bed due to exothermic adsorption by both BC is negligible. A modest variance in the results between the BCs is witnessed during the cooldown of the bed, where the current work predicts a steeper drop in temperature with time.



(a)



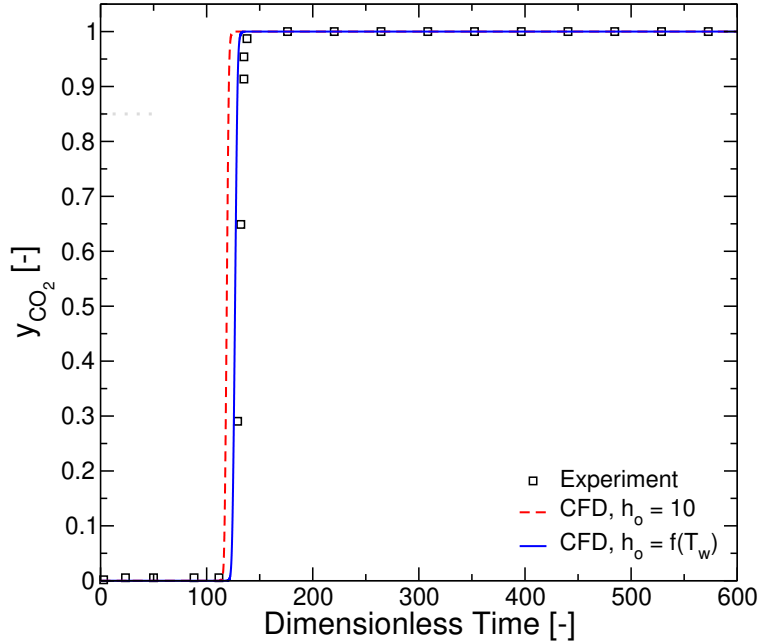
(b)

Figure 4.6: N_2 composition and temperature breakthrough curves predicted numerically for the 85 mol.% N_2 – 15 mol.% He system. Here, the symbols refer to experimental data by Wilkins and Rajendran^[57], dashed line corresponds to 2D axisymmetric CFD results for constant external heat transfer coefficient by Fabian et al.^[155], and the solid line corresponds to the current 2D axisymmetric CFD results with the natural convection boundary condition UDF. (a) Composition breakthrough. (b) Centerline temperature front at $z = 0.8L$ (h_o in $W/(m^2 \cdot K)$)

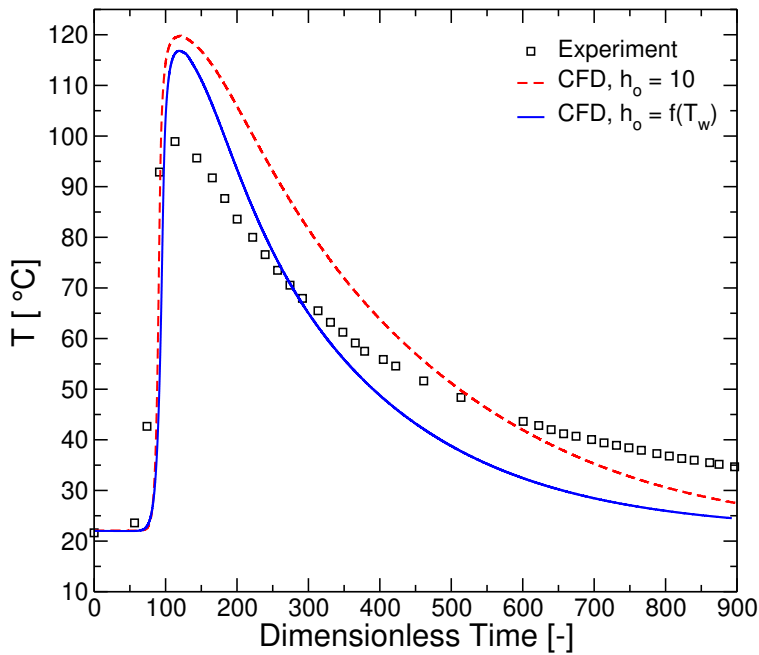
Case 2: Carbon dioxide / Helium

A 100% CO₂ – trace He system was considered. This case is the most exothermic of all lab-conducted mixture compositions due to the high heat of adsorption of CO₂ on Zeolite 13X. The resulting thermal gradients should predict the spectrum of the heat transfer coefficient for the lab rig. The ambient temperature, $T_\infty = 22^\circ\text{C}$. A flow rate, Q_{in} , of 350 standard cubic centimeters per minute (sccm) of the gas mixture was used, translating to the same interstitial velocity, v_0 as calculated in the prior case [Eq.(4.14)].

From Fig.4.7a and 4.7b, we observed a good agreement between experimental data and the model results. Comparing CFD results between constant external heat transfer coefficient $h_o = 10 \text{ (W/m}^2 \cdot \text{K)}$ vs. $h_o = f(T_w)$, the current work shows a significant improvement over the work by Fabian et al.^[155] in prediction of concentration breakthrough. While the CO₂ breakthrough curve is well predicted, the peak temperature is slightly over-predicted by about 18°C, but is still a slight improvement over the 21°C obtained by Fabian et al.^[155]. It must be stated that the peak of the temperature front is mainly influenced by the adsorbent density, ρ_p , and adsorbent specific heat capacity $C_{p,p}$, which are two of the assumed values in the CFD simulations. The overall temperature profile is found not to be very sensitive to the wall-ambient heat transfer coefficient at the lab scale. It may also be plausible that the thermocouple records temperature at a certain radial distance from the centerline.



(a)



(b)

Figure 4.7: CO₂ composition and temperature breakthrough curves predicted numerically for the 100% CO₂ – trace He system. Here, the symbols refer to experimental data by Wilkins and Rajendran^[57], dashed line corresponds to 2D axisymmetric CFD results for constant external heat transfer coefficient by Fabian et al.^[155], and the solid line corresponds to the current 2D axisymmetric CFD results with the natural convection boundary condition UDF. (a) Composition breakthrough. (b) Centerline temperature front at $z = 0.8L$ (h_o in $W/(m^2 \cdot K)$)

So far, the results shown above in Fig.(4.6) and (4.7) may also be obtained via uni-dimensional adsorption modeling. Nevertheless, conducting multidimensional simulations offers significant advantages in terms of gaining enhanced insights through spatial visualization and analyses. This is exemplified by visual representations like field contours and radial distribution plots, as illustrated in Fig.(4.8) to (4.11).

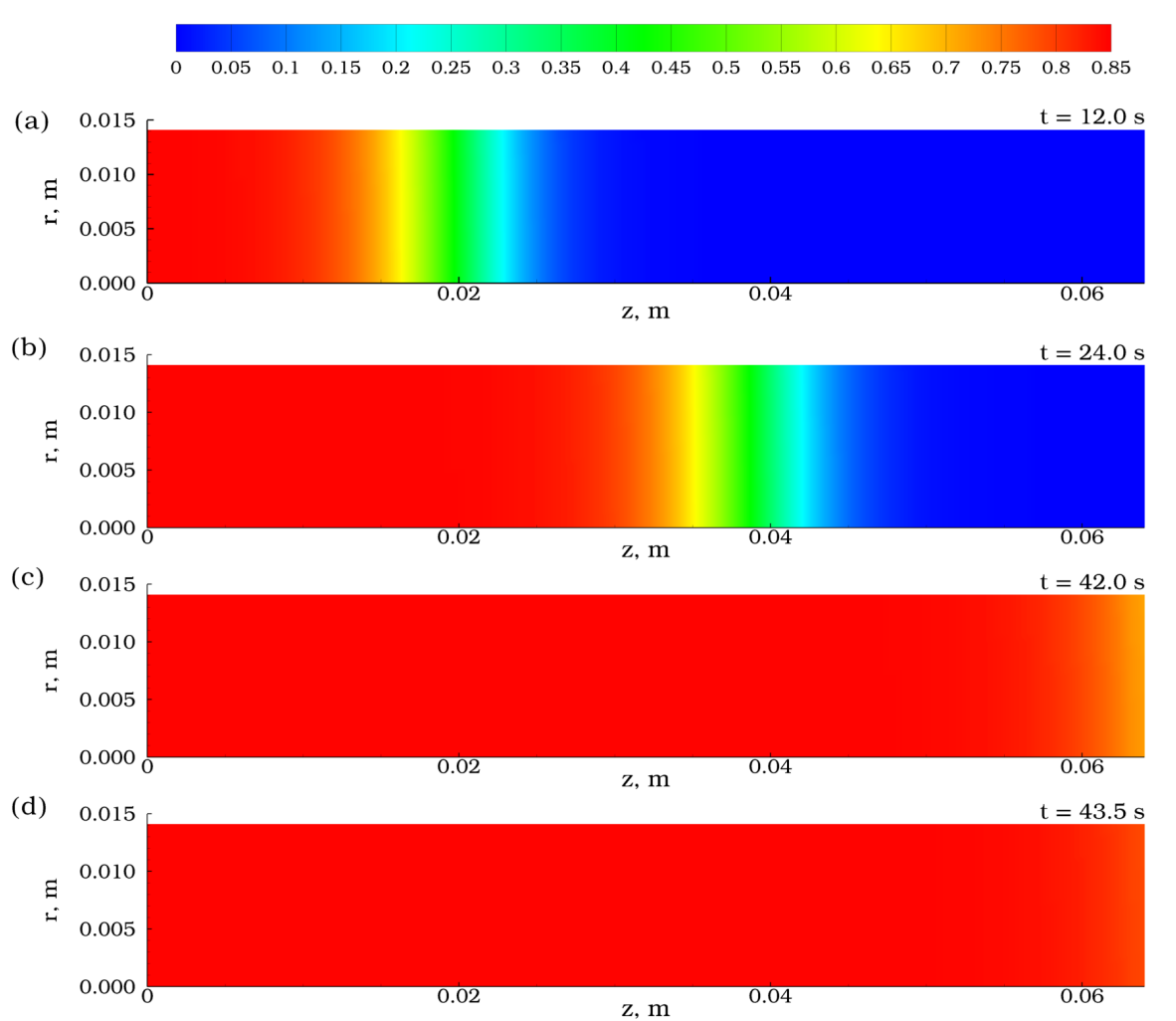


Figure 4.8: 2D contour snapshots of N_2 molar fraction (y_{N_2}) across the bed for the 85/15% N_2/He case

The first two sub-plots correspond to the fluid before composition breakthrough. At $t = 43.5s$, the bed is fully saturated with inlet gas composition. This also corresponds to the maximum value of the wall heat transfer coefficient numerically predicted and discussed further later in Fig.(4.13).

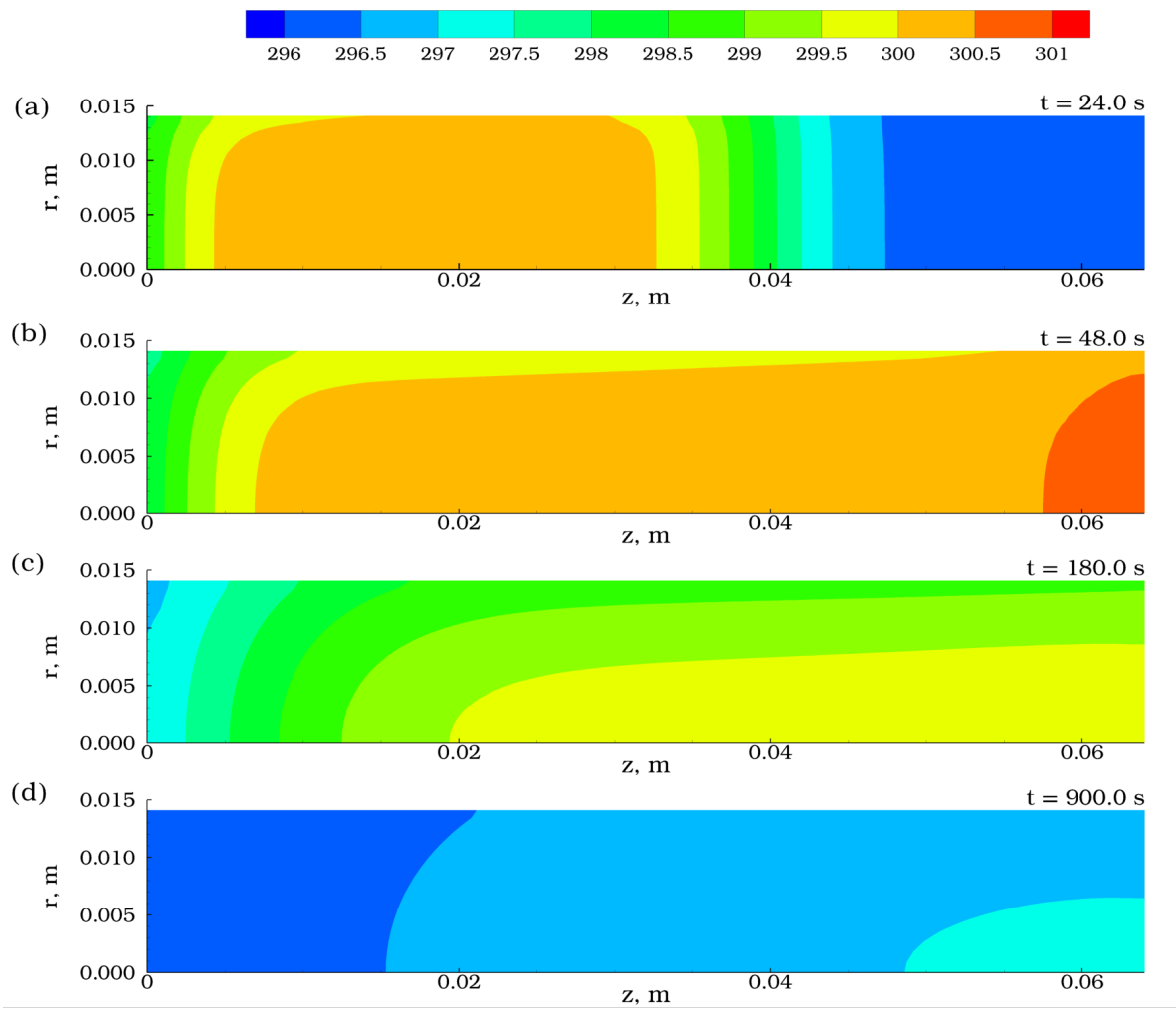


Figure 4.9: 2D contour snapshots of temperature (T , K) across the bed for the 85/15% N_2/He case

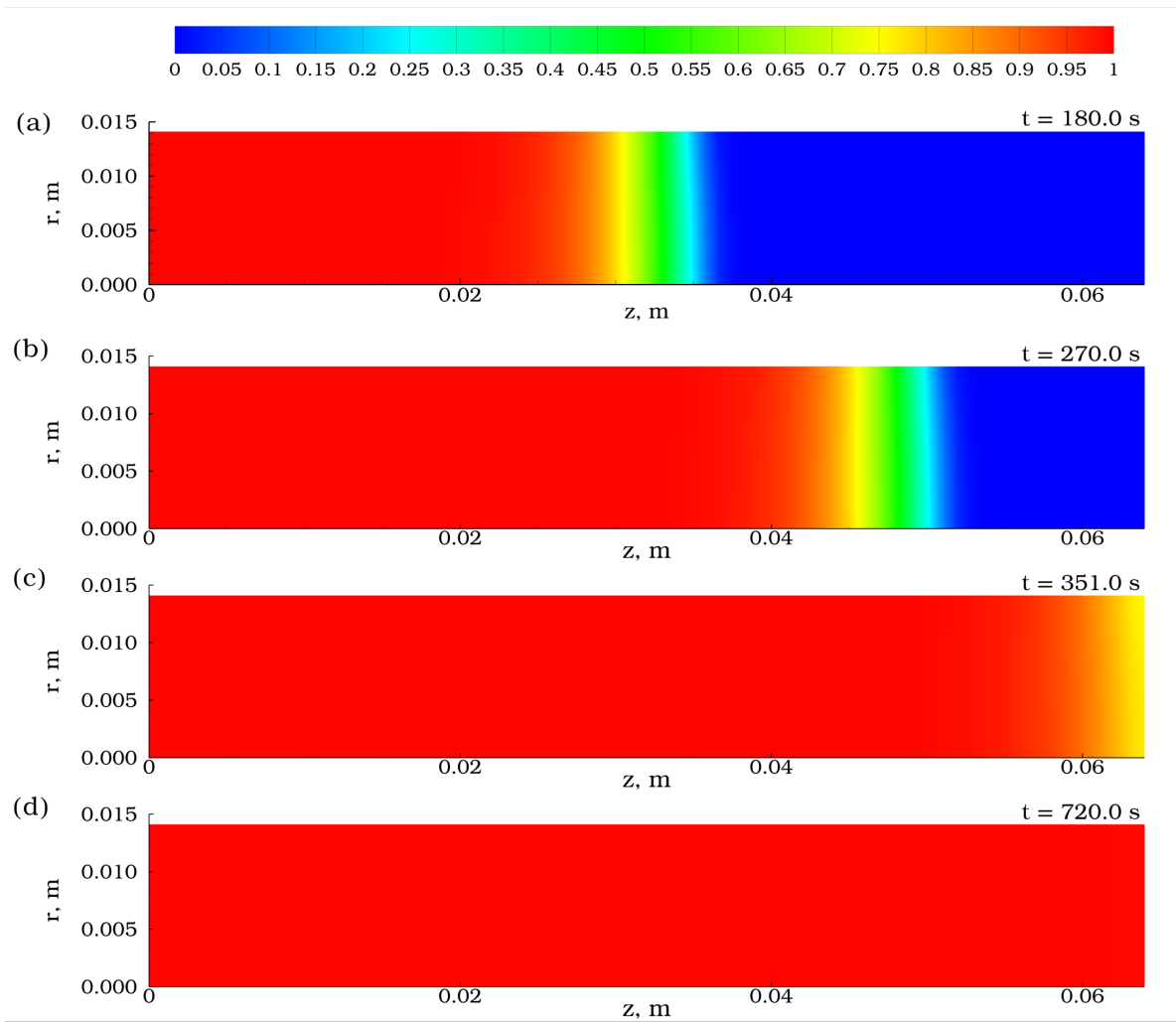


Figure 4.10: 2D contour snapshots of CO₂ molar fraction (y_{CO_2}) across the bed for the 100% CO₂/ trace He case

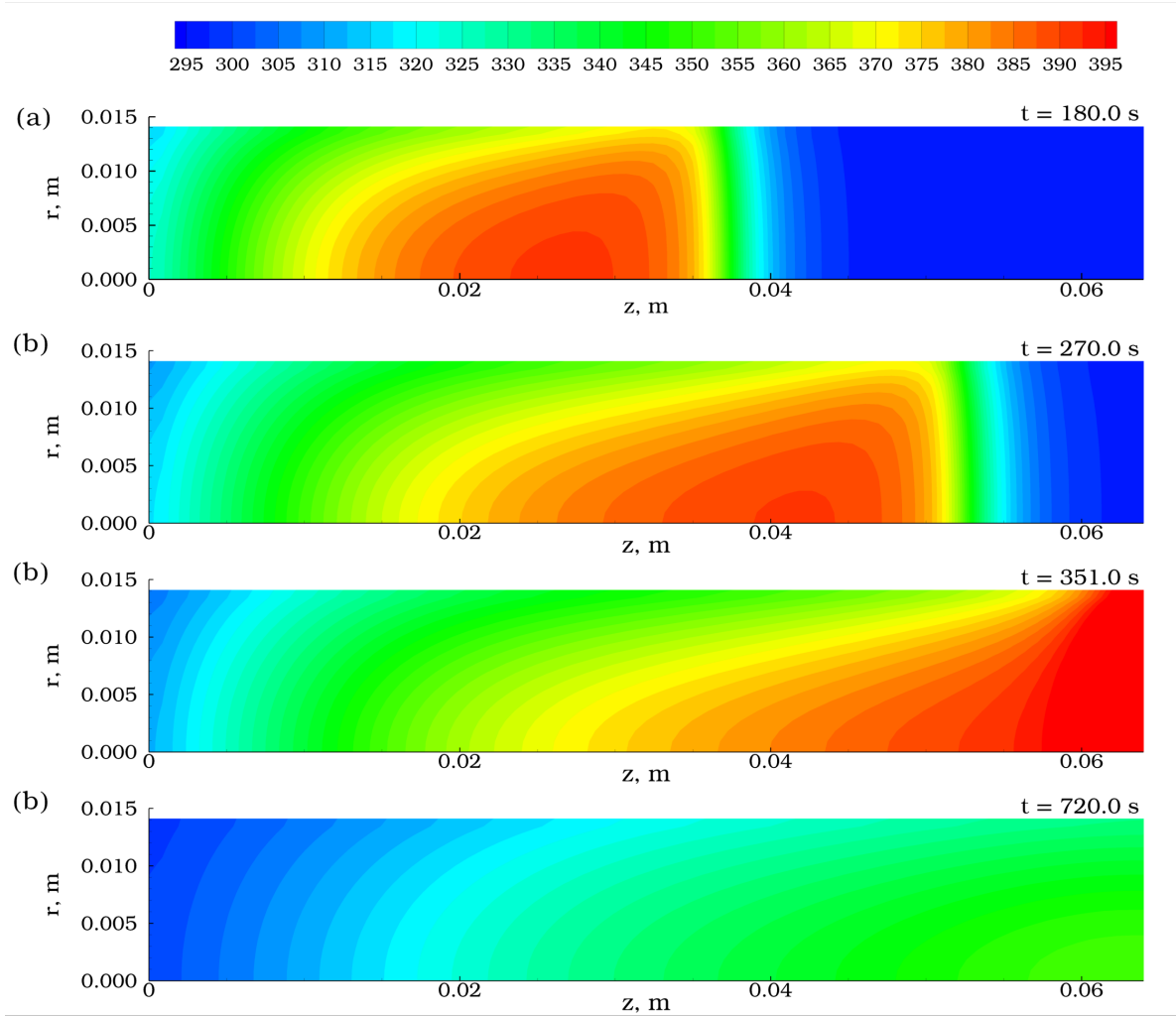


Figure 4.11: 2D contour snapshots of temperature (T , K) across the bed for the 100% CO_2 /trace He case

In 1D FVM simulations, the value of the solid thermal conductivity did not seem to affect the temperature breakthrough profiles significantly. However, in multidimensional CFD simulations, the significance of the solid thermal conductivity is quite pronounced. k_s , in essence, affects the radial distribution of heat towards the wall. Four discrete values of $k_s \in \{0.1, 0.2, 0.3, 0.4\}$ ($\text{W}/\text{m} \cdot \text{K}$) were evaluated. The spread between the centerline and the wall temperatures is shown in Fig.(4.12a) and (4.12b), respectively. Fig.(4.12c) denotes the radial average temperature at $z = 0.8L$. It is observed that as $k_s \uparrow$, $|T_{(r=0)} - T_{(r=R_w)}| \downarrow$. In other words, a higher solid thermal conductivity ensures more rapid heat transfer from the bed to the wall and, consequently, the ambient. The numerically most

extreme example would be a differential of 30°C between the centerline and wall temperatures for $k_s = 0.1$ (W/m·K). Thermal conductivity of the adsorbent/catalyst pellets has far-reaching consequences wherein although the reactor outer wall may feel ‘cool’ or ‘warm’ to the touch, opening up the bed could feel significantly hotter.

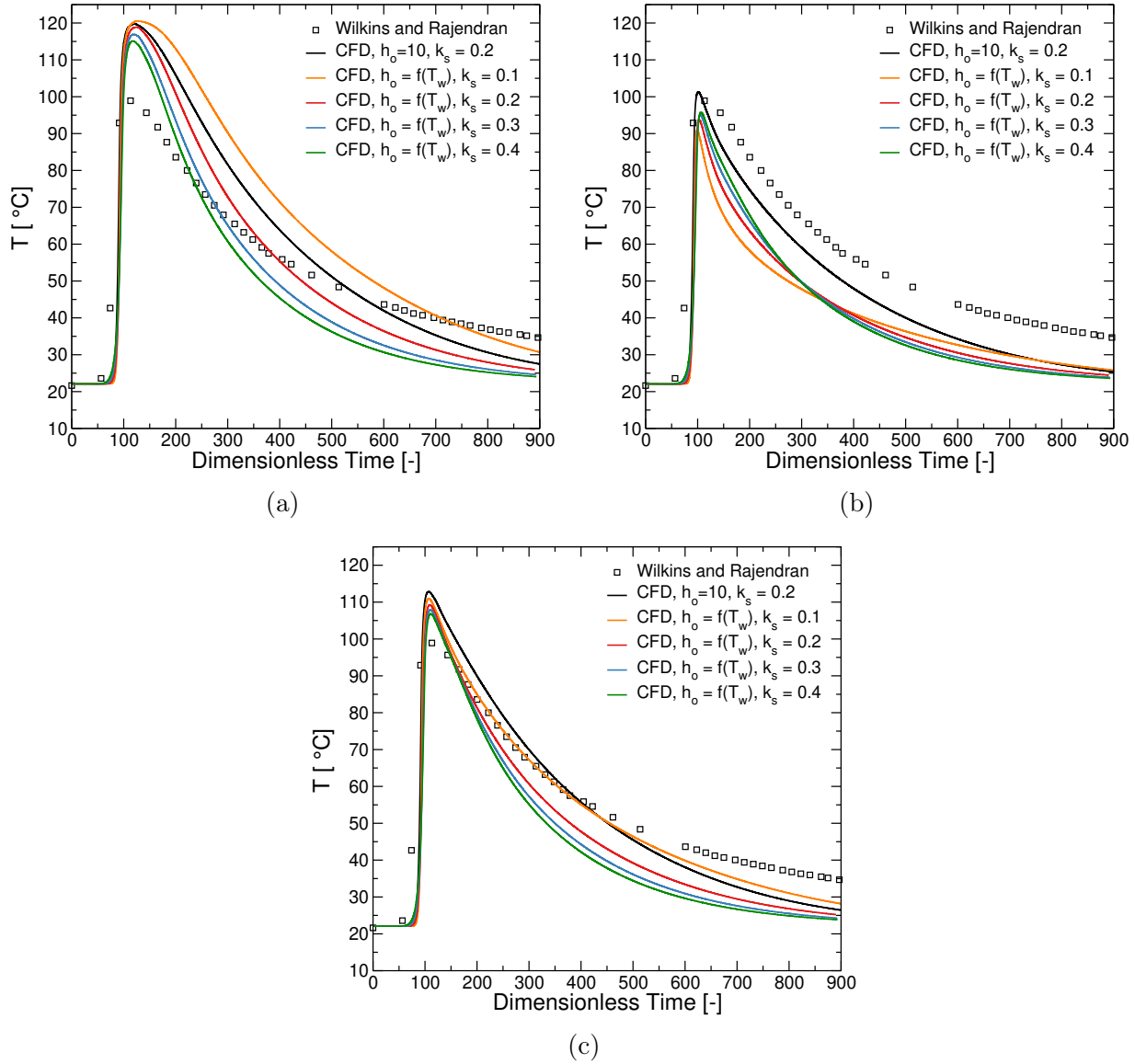


Figure 4.12: CO₂ temperature fronts predicted numerically for the 100% CO₂ – trace He system. Here, the symbols refer to experimental data by Wilkins and Rajendran^[57], and the lines correspond to the 2D axisymmetric CFD results with the natural convection boundary condition UDF for varying solid thermal conductivities, k_s . (a) Centerline, $T_{(r=0, z=0.8L)}$. (b)

Wall, $T_{(r=R_w, z=0.8L)}$. (c) Radial Area Average, $\langle T_{(z=0.8L)} \rangle = \frac{\int_0^{R_w} r \cdot T_{(r, z=0.8L)} dr}{\int r dr}$.

(h_o in $W/(m^2 \cdot K)$; k_s in $W/(m \cdot K)$)

Lastly, CFD simulations enable a transient analysis of the wall heat transfer along the bed. The heat transfer coefficient profile is applied at the face and not the cell through the DEFINE_PROFILE MACROS. Hence, the natural convection UDF must be extended to transfer face data to the adjacent cell data at the end of each time step for data visualization. Fig.4.13 and 4.14 illustrate the heat transfer coefficient contours predicted numerically for the 85 mol% N₂ - 15 mol% He case, and the 100% CO₂ case, respectively. Below in the same figure, we see the transient profiles of h_{Σ} and q_w'' for the terminal face element of the wall ($r = R_w, z = L$). Note that h_{Σ} and q_w'' are determined simultaneously in the UDF, and obviously, the wall heat transfer coefficient is numerically maximum corresponding to the time when the predicted heat rate through the wall is the highest.

For the 85 mol% N₂ - 15 mol% He case, it is evident that the natural convection driven $h_{\Sigma} \in (7, 9.5) \frac{W}{m^2.K}$. At the solution time corresponding to the highest numerically predicted h_{Σ} , (43.5 s), there does not seem to be any significant variance in h_{Σ} along the axial direction of the column [$h_{\Sigma} \sim 9.25 \frac{W}{m^2.K}$].

Throughout the transient analysis of the 100% CO₂ case, we observe that the natural convection driven h_{Σ} is range bound $\in (7, 16) \frac{W}{m^2.K}$. High temperature gradients during the breakthrough of CO₂ lead to a high numerically predicted value of h_{Σ} . Unlike the prior case, here at the particular solution time (351 s), a monotonic axial variance in $h_{\Sigma} \in (12 \text{ (inlet)}, 16 \text{ (outlet)}) \frac{W}{m^2.K}$ could be seen.

Nevertheless, the value of the wall-ambient heat transfer coefficient of $10 \frac{W}{m^2.K}$ assumed by Wilkins and Rajendran for each of the above cases is a decent initial consideration^[57]. The value of the solid thermal conductivity is another parameter that influences the radial temperature profile and must be investigated further, corroborated by Gautier et al.^[75].

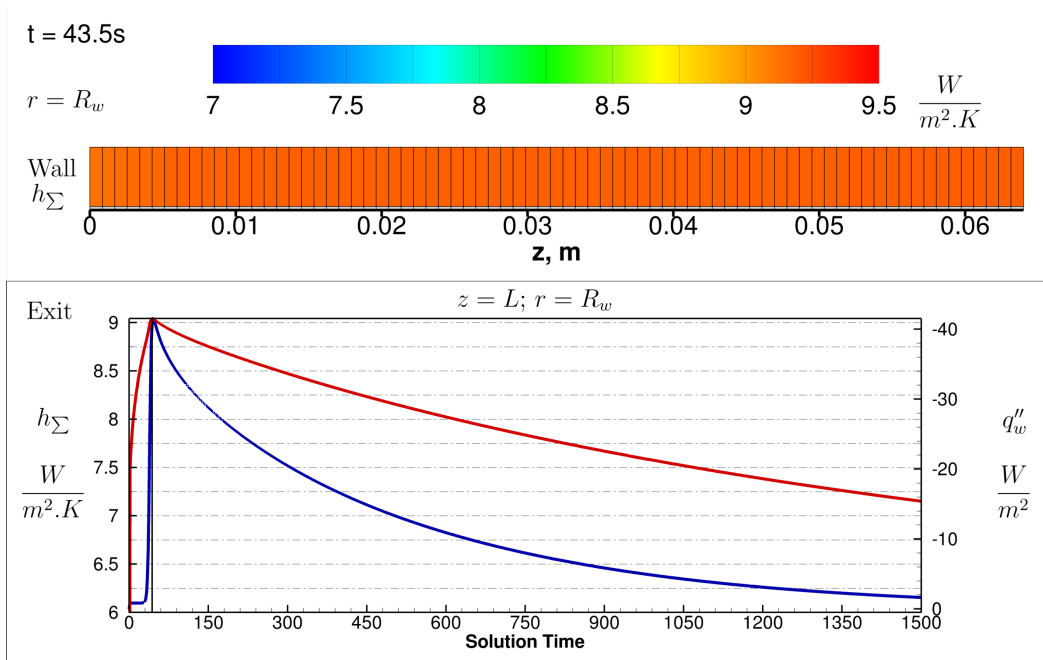


Figure 4.13: Case 1: Transient heat transfer coefficient and flux profiles corresponding to the exit wall face, ($r = R_w, z = L$). Solution time corresponds to the maximum value of the heat transfer coefficient, h_{Σ} , at the exit calculated numerically via the UDF, as depicted through the wall heat transfer coefficient contour

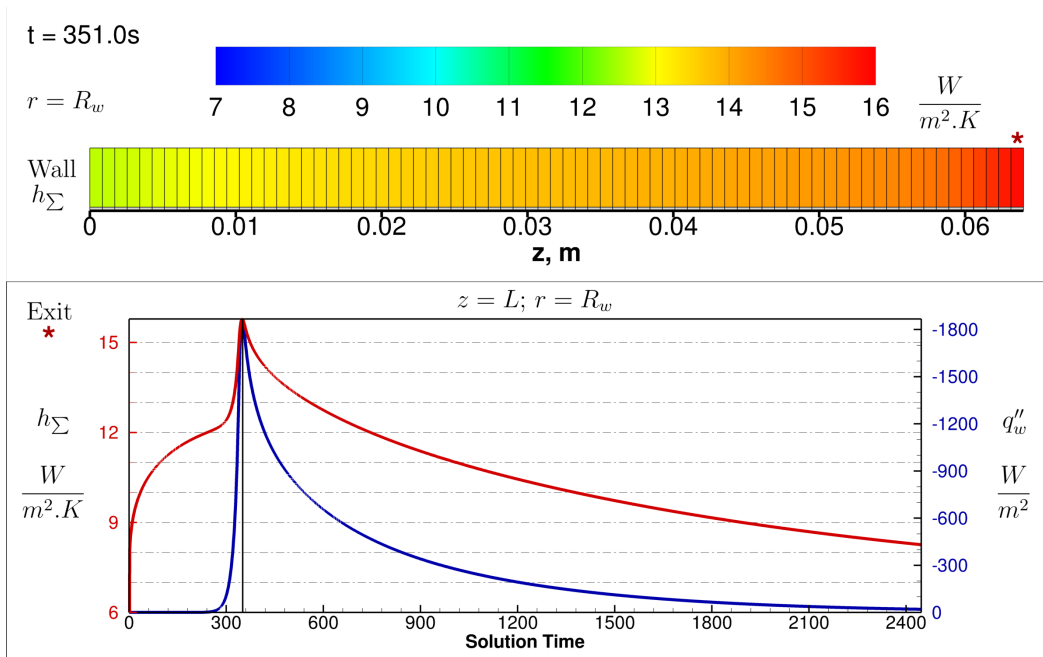


Figure 4.14: Case 2: Transient heat transfer coefficient and flux profiles corresponding to the exit wall face, ($r = R_w, z = L$). Solution time corresponds to the maximum value of the heat transfer coefficient, h_{Σ} , at the exit calculated numerically via the UDF, as depicted through the wall heat transfer coefficient contour

Chapter 5

Conclusion

5.1 Summary

In summary, this master's thesis has addressed the research question and objectives by examining the heat transfer aspects (both column and wall energy balances) involved in fixed bed modeling [Fig.(1.5)]. Through an in-depth CFD analysis, the study aimed to obtain physically sound internal and external heat transfer coefficients to improve the prediction of 1D FVM codes developed by [Haghpanah et al.](#)^[19] for a DCB run or PVSA cycle. Additionally, the natural convection boundary condition in multidimensional CFD adsorption or heat transfer studies was developed and implemented. An adsorption UDF module developed by [Fabian et al.](#)^[155] successfully replicated the experimental configuration and data presented by [Wilkins and Rajendran](#)^[57]. The experiments involved dynamic column breakthrough tests on a fixed bed adsorption system, specifically focusing on the adsorption of N_2 and CO_2 (as single components) on zeolite 13X with He as the carrier gas. In Chapter 4, insights from Chapters 2 and 3 were applied in conjunction to improve the overall prediction of the above UDF module.

Chapter 1 introduced the reader to the fundamentals of adsorption principles and provided a framework of the transport equations involved in adsorption, categorically the mass and energy source terms, equilibrium isotherms, and the linear driving force simplification for kinetics. Developments in numerical methods and computational modeling, including in the domain of CFD, were briefly discussed in addition to a case study of 1D process

modeling and optimization of a PVSA cycle for CO₂ capture. These insights should enable adaptation to other binary systems of mixtures, such as oxygen concentration from air or helium enrichment from depleted natural gas reserves.

The first phase of the study, [Chapter 2], aimed to develop a PRCFD-deduced gas-wall heat transfer correlation. Fifteen existing correlations [$Nu_w = f(Re_p, D_t/D_p, \dots)$] across literature were compiled, illustrating the lack of consensus on wall heat transfer in the laminar flow regime. A fixed bed comprising 374 particles was generated using gravity sedimentation-assisted discrete element modeling (DEM). Three-dimensional, coupled flow and heat CFD simulations were conducted to investigate fluid-wall heat transfer. Laminar and the $k-\omega$ SST RANS models were used according to the flow regime. A new semi-empirical correlation has been developed for a fixed bed packed with monodisperse spheres for $\frac{D_t}{D_p} = 3.3$ and results compared with data published in literature. The effect of buoyancy-driven flows on heat transfer within fixed beds was briefly discussed.

In the second phase of the study, [Chapter 3], the cooling down of hot water in a small cup of coffee was studied by incorporating all pertinent heat transfer mechanisms. 2D axisymmetric, laminar flow was considered for the single-phase, single-component (liquid water) system with temperature-dependent thermophysical properties. For verification, code evaluating heat fluxes vs. temperature was first developed in MATLAB and compared with the results from Fluent. For validation purposes, we performed an experiment on hot water in a standard small-size coffee cup, where the temperature of the outer side of the cup was measured using three thermo-elements. A comparison of CFD results showed excellent agreement with experiments. The validated in-house developed UDF for natural convection was, in turn, implemented towards the study of free-stream heat transfer in an adsorption column [Chapter 4]. Spatial insights unlocked by multidimensional simulations such as field temperature and composition contour visualization, radial temperature distribution analyses, and wall-ambient heat transfer coefficient prediction were discussed.

One of the significant contributions of this research was investigating the impact of different boundary conditions on the particle surface on the wall Nusselt number, Nu_w , explained by different applications from engineering. This could guide conjugate heat transfer research

in heat storage fixed beds (Dirichlet BC) or solid-liquid metal systems (Neumann BC).

Another significant contribution of this research is the development of a Newton's method solver within a UDF that iteratively calculates the heat transfer coefficient (or the wall-surrounding flux) as a function of the local and surface-average temperatures. File input/output operations were employed to store and retrieve the transient surface average temperature for Rayleigh number calculations. Thus, a UDF module capable of simulating the combined effects of natural convection, radiation, and evaporative cooling has been developed and validated. So far, CFD solvers do not yet possess natively the option to apply the natural convection or evaporative boundary conditions.

Improved confidence in the fluid-wall and wall-free stream heat transfer coefficients (h_i and h_o , respectively) enables transferring attention in the mismatch between the model and experiments to other uncertain parameters, namely, adsorbed phase thermal capacity, effective thermal conductivity, etc. Validation of the code on the laboratory scale enables its extension to industrial adsorption columns. In such cases, fitting the parameters proves to be challenging.

One of the challenges encountered throughout the research process was the limited availability of support in debugging the user-defined functions coded in C. Although Fluent UDF Macros were documented in the software user manuals^[156] and discussed in community fora, the dearth of real-world applications necessitated considerable devotion of amount of time towards implementation and future-proofing of the natural convection boundary condition UDF. 3D simulations containing geometries with control volumes in the order of millions would require parallel computing resources. Thus, our UDF source code was optimized with precise compiler commands to access the power of parallelization to implement Global Reduction Macros, such as surface and volume averaging.

Another challenge faced was in data acquisition for the hot water cooling experiment. The original adhesive came undone with time, undermined by near-boiling temperatures, requiring repeating the experiment. Eventually, as recommended by the Lab for Advanced Separation Process (LASP, University of Alberta), a heat-resistant adhesive designed for heat transfer purposes was procured for the sake of accuracy and repeatability of results.

However, it is vital to acknowledge the limitations of this study. 3D particle-resolved CFD (PRCFD) is quite computationally demanding. Mesh density and control volume count scale linearly with bed length and exponentially with tube-to-particle diameter ratio (D_t/D_p). Therefore, generating a robust mesh for fixed beds of profound interest to industrial packed bed reactors and adsorption columns ($D_t/D_p > 40$) is arduous and computationally unfeasible with current computational capacities.

A by-product of our steady state PRCFD work showed the limit of laminar flow within fixed beds corresponding to a particle Reynolds number Re_p of about ~ 105 , in line with literature. However, it is crucial to recognize that this is not a substitute for the much more meticulous laser Doppler velocimetry and flow visualization experiments. Instead, it serves as complementary evidence suggesting flow transition in fixed beds. In the range of fluid flow pertaining to the transition flow regime ($\sim 110 < Re_p < 300$), results of turbulence model simulations must be scrutinized due to the inability of RANS models to predict the transition from laminar to turbulent flow. Spectral frequency analyses would need to be performed to confirm the Kolmogorov length scale characterizing the onset of a turbulent flow regime. Time-averaged insights from transient simulations that are computationally unfeasible on contemporary workstations for particle-resolved CFD (PRCFD) simulations on meshes containing millions of polyhedral control volumes would be required. Large Eddy Simulation (LES) models may offer better insights but are inherently unsteady, computationally prohibitive, and restricted to small beds of particles. This might not reflect realistic reactors or industrial adsorption columns.

Lastly, the simulations are only as good as the parametric data used in the model. Having closed the gap with the heat transfer coefficients, some degree of mismatch between the experiment and the model is attributable to other uncertain parameters, namely effective thermal conductivity, adsorbent heat capacity, adsorbed phase heat capacity, etc. A particular issue is defining a thermodynamically-consistent specific heat capacity of the adsorbed phase. Characterizing and reporting the thermal conductivities and specific heat capacities of zeolites and MOFs in material data sheets would be appreciated. These limitations open up avenues for future research to further explore and address the gaps in knowledge.

5.2 Outlook

This study has implications for enabling a cross-verification of heat transfer parameters for improved prediction of the performance adsorption columns or the conversion in packed bed reactors. The CFD-DEM investigation [Chapter 2] may be touted as a "serial by simplification" multi-scale modeling approach, whereby the correlations developed on a 3D representative geometry may be employed in 1D reactor models. From the non-dimensional parameter Nu_w , we may obtain the gas-wall heat transfer coefficient, h_w or h_i , for adsorption and chemical reaction studies. The notorious gas-wall heat transfer resistance may be incorporated in thermal circuits to explain the steep temperature gradients near the wall. Finally, mathematical models to predict the adsorption system may thus be employed in a complementary fashion to experimental investigations as screening tools. The research also contributes to the existing literature by realizing the contribution of the solid (adsorbent or catalyst) thermal conductivity on the fluid-wall heat transfer and developing novel Nu_w vs. Re_p correlations that find validation in literature.

Chapter 3 validated not just the natural convection boundary condition for side walls but also stressed the importance of the mass transfer-driven evaporative cooling on the thermal profile of the in-situ fluid. This model is an exhibit of the broader theme of research on the implementation and validation of external boundary conditions for cavities in an ambient fluid. Our approach considered only the computational domain, i.e., the cup with water (single phase). Having excluded modeling the ambient, we eschewed delving into multi-phase volume of fluid or population balance models, thereby drastically reducing our computational costs while still capturing accurate thermal profiles. It thus becomes feasible to practically simulate 3D large eddy simulations (LES) to unlock enhanced insights into eddy formations within hot cavities in a cold ambient fluid.

Future work may extend to the following tasks:

- Implementing 3D simulations for a PVSA adsorption cycle with the natural convection BC. This is particularly applicable to industrial columns with asymmetric flow distribution due to the inlet diffuser. The 2D code used in Chapter 4 may straightforwardly be made suitable for 3D geometries by appropriately modifying the wall line averaging

to surface area averaging, as shown for the coffee cup simulations [Chapter 3].

- Investigate the influence of the ambient on the thermal profile and, thereby, the performance of the PSA cycle. A water bath or a heat transfer fluid jacket may be simulated by adjusting the ambient temperature and altering the free-stream thermophysical properties within the UDF.
- Study the influence of the orientation of the column on cycle performance. Difference correlations exist for natural convection-driven wall-ambient heat transfer depending on whether the column is buttressed vertically or horizontally.
- Simulating the influence of mixed convection (i.e., free and forced convection) on the benchmarking and key performance indicators of an adsorption process [Sec.(1.1)]. Various situations may be considered: transverse, assisting, or opposing flows. A potential improvement may include blowing air over an adsorption column solely during the adsorption step to increase the productivity of a PSA cycle.

In conclusion, this master's thesis has successfully investigated and provided valuable insights into heat transfer modeling in fixed beds. The study's findings have the potential to enhance the KPIs of adsorption processes or the conversion in chemical reactors. An increase in productivity or purity presents a stronger case for adsorption as a viable separation process for post-combustion carbon capture, oxygen concentration from air, or hydrogen purification from steam methane reforming. Future research endeavors should build upon these findings and further explore eliminating or at least mitigating the uncertainty in determining other unknowns, assumed values, or fitted parameters. Overall, this research contributes to the field of reactor and adsorber process modeling and lays a foundation for further advancement and understanding in this area.

Bibliography

- [1] JH De Boer. 50 endothermic chemisorption and catalysis. In *Advances in Catalysis*, volume 9, pages 472–480. Elsevier, 1957.
- [2] John M. Thomas. The existence of endothermic adsorption. *Journal of Chemical Education*, 38(3):138, 1961.
- [3] D M Ruthven and S Farooq. Air separation by pressure swing adsorption. *Gas Separation & Purification*, 4(3):141–148, 1990.
- [4] Jeong-Geun Jee, Min-Bae Kim, and Chang-Ha Lee. Pressure swing adsorption processes to purify oxygen using a carbon molecular sieve. *Chemical Engineering Science*, 60(3):869–882, 2005.
- [5] Jeong-Geun Jee, Sang-Jin Lee, Heung-Man Moon, and Chang-Ha Lee. Adsorption dynamics of air on zeolite 13X and CMS beds for separation and purification. *Adsorption*, 11(1):415–420, 2005.
- [6] S Sircar and TC Golden. Purification of hydrogen by pressure swing adsorption. *Separation Science and Technology*, 35(5):667–687, 2000.
- [7] Edy Herianto Majlan, Wan Ramli Wan Daud, Sunny E Iyuke, Abu Bakar Mohamad, A Amir H Kadhum, Abdul Wahab Mohammad, Mohd Sobri Takriff, and Nurhaswani Bahaman. Hydrogen purification using compact pressure swing adsorption system for fuel cell. *International journal of hydrogen energy*, 34(6):2771–2777, 2009.
- [8] José A Delgado, VI Águeda, MA Uguina, JL Sotelo, P Brea, and Carlos A Grande. Adsorption and diffusion of H₂, CO, CH₄, and CO₂ in BPL activated carbon and 13X

- zeolite: evaluation of performance in pressure swing adsorption hydrogen purification by simulation. *Industrial & Engineering Chemistry Research*, 53(40):15414–15426, 2014.
- [9] Parisa Eghbal Jahromi, Shohreh Fatemi, Ali Vatani, James A. Ritter, and Armin D. Ebner. Purification of helium from a cryogenic natural gas nitrogen rejection unit by pressure swing adsorption. *Separation and Purification Technology*, 193:91–102, 2018. ISSN 1383-5866.
- [10] Parisa Eghbal Jahromi, Shohreh Fatemi, and Ali Vatani. Effective design of a vacuum pressure swing adsorption process to recover dilute helium from a natural gas source in a methane-rich mixture with nitrogen. *Industrial & Engineering Chemistry Research*, 57(38):12895–12908, 2018.
- [11] L Gales, A Mendes, and C Costa. Recovery of acetone, ethyl acetate and ethanol by thermal pressure swing adsorption. *Chemical Engineering Science*, 58(23-24):5279–5289, 2003.
- [12] Anirudh Krishnamurthy, Harshul Thakkar, Ali A Rownaghi, and Fateme Rezaei. Adsorptive removal of formaldehyde from air using mixed-metal oxides. *Industrial & Engineering Chemistry Research*, 57(38):12916–12925, 2018.
- [13] Jelle Roegiers and Siegfried Denys. CFD-modelling of activated carbon fibers for indoor air purification. *Chemical Engineering Journal*, 365:80–87, 2019.
- [14] Sanjeev Ujjain, Abhishek Bagusetty, Yuki Matsuda, Hideki Tanaka, Preety Ahuja, Carla de Tomas, Motomu Sakai, Fernando Vallejos-Burgos, Ryusuke Futamura, Irene Suarez-Martinez, Masahiko Matsukata, Akio Kodama, Giovanni Garberoglio, Yury Gogotsi, Karl Johnson, and Katsumi Kaneko. Adsorption separation of heavier isotope gases in subnanometer carbon pores. *Nature communications*, 12(1):546, 2021.
- [15] Nicholas Stern. The economics of climate change. *American Economic Review*, 98(2): 1–37, 2008.

- [16] Jun Zhang and Paul A Webley. Cycle development and design for CO₂ capture from flue gas by vacuum swing adsorption. *Environmental science & technology*, 42(2): 563–569, 2008.
- [17] Jun Zhang, Paul A Webley, and Penny Xiao. Effect of process parameters on power requirements of vacuum swing adsorption technology for CO₂ capture from flue gas. *Energy Conversion and Management*, 49(2):346–356, 2008.
- [18] Carlos A Grande, Rui PL Ribeiro, Eduardo LG Oliveira, and Alirio E Rodrigues. Electric swing adsorption as emerging CO₂ capture technique. *Energy Procedia*, 1(1): 1219–1225, 2009.
- [19] Reza Haghpanah, Aniruddha Majumder, Ricky Nilam, Arvind Rajendran, Shamsuzaman Farooq, Iftekhar A. Karimi, and Mohammad Amanullah. Multiobjective Optimization of a Four-Step Adsorption Process for Postcombustion CO₂ Capture Via Finite Volume Simulation. *Industrial & Engineering Chemistry Research*, 52(11):4249–4265, 2013.
- [20] Yahui Lian, Shuai Deng, Shuangjun Li, Zhihao Guo, Li Zhao, and Xiangzhou Yuan. Numerical analysis on CO₂ capture process of temperature swing adsorption (TSA): Optimization of reactor geometry. *International Journal of Greenhouse Gas Control*, 85:187–198, 2019.
- [21] Vlad-Cristian Sandu, Ana-Maria Cormos, Ionela-Dorina Dumbrava, Arpad Imre-Lucaci, Calin-Cristian Cormos, Robert de Boer, Jurriaan Boon, and Soraya Sluijter. Assessment of CO₂ capture efficiency in packed bed versus 3D-printed monolith reactors for SEWGS using CFD modeling. *International Journal of Greenhouse Gas Control*, 111:103447, 2021.
- [22] Douglas M Ruthven. *Principles of adsorption and adsorption processes*. John Wiley & Sons, 1984.
- [23] Cheng-Hsiu Yu, Chih-Hung Huang, and Chung-Sung Tan. A review of CO₂ capture by absorption and adsorption. *Aerosol and Air Quality Research*, 12(5):745–769, 2012.

- [24] Mohammad Songolzadeh, Maryam Takht Ravanchi, and Mansooreh Soleimani. Carbon dioxide capture and storage: a general review on adsorbents. *International Journal of Chemical and Molecular Engineering*, 6(10):906–913, 2012.
- [25] M Clause, J Bonjour, and F Meunier. Adsorption of gas mixtures in TSA adsorbents under various heat removal conditions. *Chemical Engineering Science*, 59(17):3657–3670, 2004.
- [26] RPPL Ribeiro, CA Grande, and Alírio E Rodrigues. Electric swing adsorption for gas separation and purification: a review. *Separation Science and Technology*, 49(13):1985–2002, 2014.
- [27] Hui An, Bo Feng, and Shi Su. CO₂ capture by electrothermal swing adsorption with activated carbon fibre materials. *International Journal of Greenhouse Gas Control*, 5(1):16–25, 2011.
- [28] Douglas M Ruthven, Shamsuzzaman Farooq, and Kent S Knaebel. *Pressure swing adsorption*. John Wiley & Sons, 1996.
- [29] Irving Langmuir. The adsorption of gases on plane surfaces of glass, mica and platinum. *Journal of the American Chemical society*, 40(9):1361–1403, 1918.
- [30] Keith J Laidler. The development of the Arrhenius equation. *Journal of Chemical Education*, 61(6):494, 1984.
- [31] S.I. Sandler. *Chemical, Biochemical, and Engineering Thermodynamics*. John Wiley & Sons, 2017. ISBN 9780470504796.
- [32] J Toth. State equation of the solid-gas interface layers. *Acta chim. hung.*, 69:311–328, 1971.
- [33] Duong D Do. *Adsorption analysis: Equilibria and kinetics (with cd containing computer MATLAB programs)*, volume 2. World Scientific, 1998.
- [34] Jianlong Wang and Xuan Guo. Adsorption kinetic models: Physical meanings, applications, and solving methods. *Journal of Hazardous Materials*, 390:122156, 2020.

- [35] S Sircar and JR Hufton. Why does the linear driving force model for adsorption kinetics work? *Adsorption*, 6(2):137–147, 2000.
- [36] E Glueckauf and JI Coates. Theory of chromatography. Part IV. The influence of incomplete equilibrium on the front boundary of chromatograms and on the effectiveness of separation. *Journal of the Chemical Society (Resumed)*, pages 1315–1321, 1947.
- [37] Eugen Glueckauf. Theory of chromatography. part 10.—formulæ for diffusion into spheres and their application to chromatography. *Transactions of the Faraday Society*, 51:1540–1551, 1955.
- [38] Nicholas Stiles Wilkins, Arvind Rajendran, and Shamsuzzaman Farooq. Dynamic column breakthrough experiments for measurement of adsorption equilibrium and kinetics. *Adsorption*, 27(3):397–422, 2021.
- [39] Joseph Oakland Hirschfelder, Charles F Curtiss, and R Byron Bird. Molecular theory of gases and liquids. *Molecular theory of gases and liquids*, 1964.
- [40] R Byron Bird. Transport phenomena. *Appl. Mech. Rev.*, 55(1):R1–R4, 2002.
- [41] Bruce E Poling, John M Prausnitz, and John P O’connell. *Properties of gases and liquids*. McGraw-Hill Education, 2001.
- [42] N Wakao and T Funazkri. Effect of fluid dispersion coefficients on particle-to-fluid mass transfer coefficients in packed beds: correlation of Sherwood numbers. *Chemical Engineering Science*, 33(10):1375–1384, 1978.
- [43] R Ben-Mansour, MA Habib, OE Bamidele, M Basha, NAA Qasem, A Peedikakkal, T Laoui, and MJAE Ali. Carbon capture by physical adsorption: materials, experimental investigations and numerical modeling and simulations—a review. *Applied Energy*, 161:225–255, 2016.
- [44] Warren Lee McCabe, Julian Cleveland Smith, and Peter Harriott. *Unit Operations of Chemical Engineering*, volume 7. McGraw-Hill New York, 2005.
- [45] Sabri Ergun. Fluid flow through packed columns. *Chem. Eng. Prog.*, 48:89–94, 1952.

- [46] Bernhard Eisfeld and Klaus Schnitzlein. The influence of confining walls on the pressure drop in packed beds. *Chemical Engineering Science*, 56(14):4321–4329, 2001.
- [47] Bhanu Vardhan Reddy Kuncharam and Anthony G Dixon. Multi-scale two-dimensional packed bed reactor model for industrial steam methane reforming. *Fuel Processing Technology*, 200:106314, 2020.
- [48] Mohammad Saleh Shafeeyan, Wan Mohd Ashri Wan Daud, and Ahmad Shamiri. A review of mathematical modeling of fixed-bed columns for carbon dioxide adsorption. *Chemical engineering research and design*, 92(5):961–988, 2014.
- [49] Toluleke E Akinola, Phebe L Bonilla Prado, and Meihong Wang. Experimental studies, molecular simulation and process modelling\simulation of adsorption-based post-combustion carbon capture for power plants: A state-of-the-art review. *Applied Energy*, 317:119156, 2022.
- [50] Paul A Webley and Jianming He. Fast solution-adaptive finite volume method for PSA/VSA cycle simulation; 1 single step simulation. *Computers & Chemical Engineering*, 23(11-12):1701–1712, 2000.
- [51] Richard S Todd, Jianming He, Paul A Webley, Christopher Beh, Simon Wilson, and Matthew A Lloyd. Fast finite-volume method for PSA/VSA cycle simulation experimental validation. *Industrial & Engineering Chemistry Research*, 40(14):3217–3224, 2001.
- [52] P Cruz, MA Alves, FD Magalhaes, and A Mendes. Solution of hyperbolic PDEs using a stable adaptive multiresolution method. *Chemical Engineering Science*, 58(9):1777–1792, 2003.
- [53] P Cruz, JC Santos, FD Magalhaes, and Adélio Mendes. Simulation of separation processes using finite volume method. *Computers & chemical engineering*, 30(1):83–98, 2005.
- [54] Shumaila Javeed, Shamsul Qamar, Andreas Seidel-Morgenstern, and Gerald Warnecke.

- Efficient and accurate numerical simulation of nonlinear chromatographic processes. *Computers & chemical engineering*, 35(11):2294–2305, 2011.
- [55] Bijan Medi and Mohammad Amanullah. Application of a finite-volume method in the simulation of chromatographic systems: effects of flux limiters. *Industrial & engineering chemistry research*, 50(3):1739–1748, 2011.
- [56] Randall J LeVeque et al. *Finite volume methods for hyperbolic problems*, volume 31. Cambridge university press, 2002.
- [57] Nicholas Stiles Wilkins and Arvind Rajendran. Measurement of competitive CO₂ and N₂ adsorption on zeolite 13X for post-combustion CO₂ capture. *Adsorption*, 25(2): 115–133, 2019.
- [58] Mark Woods and Michael Matuszewski. Quality guideline for energy system studies: CO₂ impurity design parameters. Technical report, National Energy Technology Laboratory (NETL), Pittsburgh, PA, Morgantown, WV, 2012.
- [59] Arno De Klerk. Voidage variation in packed beds at small column to particle diameter ratio. *AIChE journal*, 49(8):2022–2029, 2003.
- [60] CY Wu, YM Ferng, CC Chieng, and CC Liu. Investigating the advantages and disadvantages of realistic approach and porous approach for closely packed pebbles in CFD simulation. *Nuclear Engineering and design*, 240(5):1151–1159, 2010.
- [61] Alfredo Guardo, Miguel Coussirat, M Angels Larrayoz, Francesc Recasens, and Eduard Egusquiza. CFD flow and heat transfer in nonregular packings for fixed bed equipment design. *Industrial & Engineering Chemistry Research*, 43(22):7049–7056, 2004.
- [62] A. Guardo, M. Coussirat, M.A. Larrayoz, F. Recasens, and E. Egusquiza. Influence of the turbulence model in CFD modeling of wall-to-fluid heat transfer in packed beds. *Chemical Engineering Science*, 60(6):1733–1742, 2005.
- [63] Mandar V Tabib, Stein T Johansen, and Shahriar Amini. A 3D CFD-DEM methodology for simulating industrial scale packed bed chemical looping combustion reactors. *Industrial & Engineering Chemistry Research*, 52(34):12041–12058, 2013.

- [64] Saurish Das, Niels G Deen, and JAM Kuipers. A DNS study of flow and heat transfer through slender fixed-bed reactors randomly packed with spherical particles. *Chemical Engineering Science*, 160:1–19, 2017.
- [65] Michiel Nijemeisland and Anthony G Dixon. CFD study of fluid flow and wall heat transfer in a fixed bed of spheres. *AIChE journal*, 50(5):906–921, 2004.
- [66] F Augier, C Laroche, and E Brehon. Application of computational fluid dynamics to fixed bed adsorption calculations: effect of hydrodynamics at laboratory and industrial scale. *Separation and Purification Technology*, 63(2):466–474, 2008.
- [67] Korinek Tomas and Frana Karel. An adsorption of carbon dioxide on activated carbon controlled by temperature swing adsorption. *AIP Conference Proceedings*, 1889(1): 020023, 2017.
- [68] Ronald W Breault, Lawrence J Shadle, James L Spenik, and E David Huckaby. CO₂ adsorption: experimental investigation and CFD reactor model validation. *Journal of Computational Environmental Sciences*, 2014, 2014.
- [69] Sai Gokul Subraveti, Petr Nikrityuk, and Arvind Rajendran. Computational fluid dynamics study of viscous fingering in supercritical fluid chromatography. *Journal of Chromatography A*, 1534:150–160, 2018.
- [70] Sammy W Verbruggen, Maarten Keulemans, Jeroen van Walsem, Tom Tytgat, Silvia Lenaerts, and Siegfried Denys. CFD modeling of transient adsorption/desorption behavior in a gas phase photocatalytic fiber reactor. *Chemical Engineering Journal*, 292: 42–50, 2016.
- [71] Flora Esposito, Cristian Cardenas, Abderrazak M Latifi, and Stéphanie Marsteau. CFD modeling and simulation of an ammonia adsorption process. In *Computer Aided Chemical Engineering*, volume 51, pages 463–468. Elsevier, 2022.
- [72] Naef AA Qasem and Rached Ben-Mansour. Energy and productivity efficient vacuum pressure swing adsorption process to separate CO₂ from CO₂/N₂ mixture using Mg-MOF-74: A CFD simulation. *Applied Energy*, 209:190–202, 2018.

- [73] Tirzhá LP Dantas, Francisco Murilo T Luna, Ivanildo J Silva Jr, Antonio Eurico B Torres, Diana CS de Azevedo, Alírio E Rodrigues, and Regina FPM Moreira. Carbon dioxide–nitrogen separation through pressure swing adsorption. *Chemical engineering journal*, 172(2-3):698–704, 2011.
- [74] R Gautier, T Dbouk, MA Campesi, Lomig Hamon, J-L Harion, and Pascaline Pré. Pressure-swing-adsorption of gaseous mixture in isotropic porous medium: Transient 3D modeling and validation. *Chemical Engineering Journal*, 348:1049–1062, 2018.
- [75] R Gautier, T Dbouk, J-L Harion, Lomig Hamon, and Pascaline Pré. Pressure-swing-adsorption of gaseous mixture in isotropic porous medium: Numerical sensitivity analysis in CFD. *Chemical Engineering Research and Design*, 129:314–326, 2018.
- [76] KR Jolls and TJ Hanratty. Transition to turbulence for flow through a dumped bed of spheres. *Chemical Engineering Science*, 21(12):1185–1190, 1966.
- [77] A Dybbs and RV Edwards. A new look at porous media fluid mechanics—Darcy to turbulent. *Fundamentals of transport phenomena in porous media*, pages 199–256, 1984.
- [78] MA Latifi, N Midoux, A Storck, and JN Gence. The use of micro-electrodes in the study of the flow regimes in a packed bed reactor with single phase liquid flow. *Chemical Engineering Science*, 44(11):2501–2508, 1989.
- [79] S Rode, Noel Midoux, Mohamed Abderrazak Latifi, Alain Storck, and Estéban Saatchian. Hydrodynamics of liquid flow in packed beds: an experimental study using electrochemical shear rate sensors. *Chemical Engineering Science*, 49(6):889–900, 1994.
- [80] Jacob Bear. *Dynamics of fluids in porous media*. Courier Corporation, 2013.
- [81] D Seguin, Agnès Montillet, J Comiti, and F Huet. Experimental characterization of flow regimes in various porous media—II: Transition to turbulent regime. *Chemical Engineering Science*, 53(22):3897–3909, 1998.

- [82] Adam Ward and Ronny Pini. Integrated uncertainty quantification and sensitivity analysis of single-component dynamic column breakthrough experiments. *Adsorption*, 28(3-4):161–183, 2022.
- [83] R. E. Hayes and J. P. Mmbaga. *Introduction to chemical reactor analysis*. CRC Press/Taylor & Francis Group, 2012. ISBN 9781466580534.
- [84] Olaf R. Derkx and Anthony G. Dixon. Effect of the wall nusselt number on the simulation of catalytic fixed bed reactors. *Catalysis Today*, 35:435–442, 4 1997.
- [85] Frédéric Delage, Pascaline Pré, and Pierre Le Cloirec. Mass transfer and warming during adsorption of high concentrations of VOCs on an activated carbon bed: experimental and theoretical analysis. *Environmental science & technology*, 34(22):4816–4821, 2000.
- [86] Pierre Le Cloirec, Pascaline Pré, Frédéric Delage, and Sylvain Giraudet. Visualization of the exothermal VOC adsorption in a fixed-bed activated carbon adsorber. *Environmental technology*, 33(3):285–290, 2012.
- [87] J Jo Barker. Heat transfer in packed beds. *Industrial & Engineering Chemistry*, 57(4):43–51, 1965.
- [88] E Tsotsas and E-U Schlünder. Heat transfer in packed beds with fluid flow: remarks on the meaning and the calculation of a heat transfer coefficient at the wall. *Chemical Engineering Science*, 45(4):819–837, 1990.
- [89] Max Leva. Heat transfer to gases through packed tubes. *Industrial & Engineering Chemistry*, 39(7):857–862, 1947.
- [90] Max Leva, Murray Weintraub, Milton Grummer, and EL Clark. Cooling of gases through packed tubes. *Industrial & Engineering Chemistry*, 40(4):747–752, 1948.
- [91] YC Chu and J Anderson Storrow. Heat transfer to air flowing through packed tubes. *Chemical Engineering Science*, 1(5):230–237, 1952.

- [92] Sakae Yagi and Noriaki Wakao. Heat and mass transfer from wall to fluid in packed beds. *AIChE Journal*, 5:79–85, 3 1959. ISSN 0001-1541.
- [93] Daizo Kunii, Motoyuki Suzuki, and Naoshi Ono. Heat transfer from wall surface to packed beds at high Reynolds number. *Journal of Chemical Engineering of Japan*, 1(1):21–26, 1968.
- [94] WE Olbrich and OE Potter. Heat transfer in small diameter packed beds. *Chemical Engineering Science*, 27(9):1723–1732, 1972.
- [95] Chi Hsiung Li and B. A. Finlayson. Heat transfer in packed beds—a reevaluation. *Chemical Engineering Science*, 32:1055–1066, 1977. ISSN 00092509.
- [96] V Specchia, G Baldi, and S Sicardi. Heat transfer in packed bed reactors with one phase flow. *Chemical Engineering Communications*, 4(1-3):361–380, 1980.
- [97] RA Colledge and WR Paterson. Heat transfer at the wall of a packed bed: A j-factor analogy established. *Collected Papers*, 1984.
- [98] Anthony G Dixon, Michael A DiCostanzo, and Brian A Soucy. Fluid-phase radial transport in packed beds of low tube-to-particle diameter ratio. *International Journal of Heat and Mass Transfer*, 27(10):1701–1713, 1984.
- [99] Patrick E Peters, Rinaldo S Schifano, and Peter Harriott. Heat transfer in packed-tube reactors. *Industrial & Engineering Chemistry Research*, 27(2):226–233, 1988.
- [100] Holger Martin and Michael Nilles. Radiale wärmeleitung in durchströmten schüttingsrohren. *Chemie Ingenieur Technik*, 65(12):1468–1477, 1993.
- [101] Y. Demirel, R. N. Sharma, and H. H. Al-Ali. On the effective heat transfer parameters in a packed bed. *International Journal of Heat and Mass Transfer*, 43:327–332, 2000.
- [102] O. Laguerre, S. Ben Amara, and D. Flick. Heat transfer between wall and packed bed crossed by low velocity airflow. *Applied Thermal Engineering*, 26:1951–1960, 11 2006.

- [103] Anthony G Dixon, Michiel Nijemeisland, and E Hugh Stitt. Packed tubular reactor modeling and catalyst design using computational fluid dynamics. *Advances in Chemical Engineering*, 31:307–389, 2006.
- [104] Allan P Colburn. Heat transfer and pressure drop in empty, baffled, and packed tubes. *Industrial & Engineering Chemistry*, 23(8):910–913, 1931.
- [105] GM Chrysler and RE Simons. An experimental investigation of the forced convection heat transfer characteristics of fluorocarbon liquid flowing through a packed-bed for immersion cooling of microelectronic heat sources. In *Parallel and Vector Computation in Heat Transfer—Presented at AIAA/ASME Thermophysics and Heat Transfer Conference, Seattle, WA, USA*, pages 21–27, 1990.
- [106] TH Hwang, Y Cai, and P Cheng. An experimental study of forced convection in a packed channel with asymmetric heating. *International journal of heat and mass transfer*, 35(11):3029–3039, 1992.
- [107] Yasar Demirel, BA Abu-Al-Saud, HH Al-Ali, and Y Makkawi. Packing size and shape effects on forced convection in large rectangular packed ducts with asymmetric heating. *International journal of heat and mass transfer*, 42(17):3267–3277, 1999.
- [108] Anthony G Dixon. Wall and particle-shape effects on heat transfer in packed beds. *Chemical engineering communications*, 71(1):217–237, 1988.
- [109] Anthony G Dixon. Heat transfer in fixed beds at very low (< 4) tube-to-particle diameter ratio. *Industrial & engineering chemistry research*, 36(8):3053–3064, 1997.
- [110] A Storck and F Coeuret. Mass transfer between a flowing liquid and a wall or an immersed surface in fixed and fluidized beds. *The Chemical Engineering Journal*, 20(2):149–156, 1980.
- [111] Friedrich-Wilhelm Hennecke and Ernst Ulrich Schlünder. Wärmeübergang in beheizten oder gekühlten rohren mit schüttungen aus kugeln, zylindern und raschig-ringen. *Chemie Ingenieur Technik*, 45(5):277–284, 1973.

- [112] D Vortmeyer and E Haidegger. Discrimination of three approaches to evaluate heat fluxes for wall-cooled fixed bed chemical reactors. *Chemical Engineering Science*, 46(10):2651–2660, 1991.
- [113] Thomas Daszkowski and Gerhart Eigenberger. A reevaluation of fluid flow, heat transfer and chemical reaction in catalyst filled tubes. *Chemical Engineering Science*, 47(9-11):2245–2250, 1992.
- [114] Michiel Nijemeisland and Anthony G Dixon. Comparison of CFD simulations to experiment for convective heat transfer in a gas–solid fixed bed. *Chemical Engineering Journal*, 82(1-3):231–246, 2001.
- [115] V. Chandra, E.A.J.F. Peters, and J.A.M. Kuipers. Direct numerical simulation of a non-isothermal non-adiabatic packed bed reactor. *Chem. Eng. Journal*, 385:123641, 2020.
- [116] C. Diaz-Goano, P.D. Minev, and K. Nandakumar. A fictitious domain/finite element method for particulate flows. *Journal of Computational Physics*, 192:105–123, 2003.
- [117] N.G. Deen, E.A.J.F. Peters, J.T. Padding, and J.A.M. Kuipers. Review of direct numerical simulation of fluid-particle mass, momentum and heat transfer in dense gas-solid flows. *Chem. Eng. Sci.*, 116:710–724, 2014.
- [118] S. Golshan, R. Sotudeh-Gharebagh, R. Zarghami, N. Mostoufi, B. Blais, and J.A.M. Kuipers. Review and implementation of CFD-DEM applied to chemical process systems. *Chemical Engineering Science*, 221:115646, 2020.
- [119] Anthony G. Dixon. Wall and particle-shape effects on heat transfer in packed beds. *Chemical Engineering Communications*, 71:217–237, 9 1988. ISSN 15635201.
- [120] G.R. George, M. Bockelmann, L. Schmalhorst, D. Beton, A. Gerstle, A. Lindermeir, and G.D. Wehinger. Radial heat transport in a fixed-bed reactor made of metallic foam pellets: Experiment and particle-resolved computational fluid dynamics. *International Journal of Heat and Mass Transfer*, 197:123376, 2022.

- [121] Y.R. Lu and P.A. Nikrityuk. DEM-based model for steam methane reforming. *Chemical Engineering Science*, 247:116903, 2022.
- [122] Jan Kozicki and Frederic V. Donze. YADE-OPEN DEM: An open-source software using a discrete element method to simulate granular material. *Engineering Computations*, 26(7):786 – 805, 2009.
- [123] Yi Ran Lu and Petr A. Nikrityuk. A fixed-bed reactor for energy storage in chemicals (E2C): Proof of concept. *Applied Energy*, 228:593–607, 2018.
- [124] A.G. Dixon, M. Nijemeisland, and E.H. Stitt. Systematic mesh development for 3D CFD simulation of fixed beds: contact points study. *Comput. Chem. Eng.*, 48:135–153, 2013.
- [125] M. Pichler, B. Haddadi, C. Jordan, H. Norouzi, and M. Harasek. Effect of particle contact point treatment on the CFD simulation of the heat transfer in packed beds. *Chem. Eng. Res. and Design*, 165:242–253, 2021.
- [126] Suhas V Patankar. *Numerical heat transfer and fluid flow*. Series on Computational Methods in Mechanics and Thermal Science. Hemisphere Publishing Corporation, Washington, D.C. (CRC Press, Taylor & Francis Group), 1980. ISBN 978-0891165224. URL <http://www.crcpress.com/product/isbn/9780891165224>.
- [127] ANSYS Fluent™, Release 19R3, - CFD Software | ANSYS, Inc., www.ansys.com/products/fluids/ansys-fluent. Accessed: 03/03/2023, 2019.
- [128] ANSYS Fluent™, Release 19R3, - Ansys Fluent Theory Guide | ANSYS, Inc., www.ansys.com/. Accessed: June 2023, 2019.
- [129] S. Bale, S. Tiwari, M. Sathe, A.S. Berrouk, K. Nandakumar, and J. Joshi. Direct numerical simulation study of end effects and D/d ratio on mass transfer in packed beds. *International Journal of Heat and Mass Transfer*, 127:234–244, 2018.
- [130] F.R. Menter. Two-equation eddy-viscosity turbulence models for engineering applications. *AIAA Journal*, 32(8):1598–1605, 1994.

- [131] DJ Gunn. Transfer of heat or mass to particles in fixed and fluidised beds. *International Journal of Heat and Mass Transfer*, 21(4):467–476, 1978.
- [132] K. Wittig, A. Golia, and P.A. Nikrityuk. Numerical study of the influence of particle porosity on the heat and fluid flow. *Progress in Computational Fluid Dynamics*, 12: 207–219, 2012.
- [133] A. Richter and P.A. Nikrityuk. Heat and fluid flow around a sphere with cylindrical bore. *ASME J. Heat Transfer*, 134:071704, 2012.
- [134] Haiteng Ma and Li He. Large eddy simulation of natural convection heat transfer and fluid flow around a horizontal cylinder. *International Journal of Thermal Sciences*, 162:106789, 2021.
- [135] D.A. Kaminski and C. Prakash. Conjugate natural convection in a square enclosure: effect of conduction in one of the vertical walls. *Int. J. Heat Mass Transfer*, 29:1979–1988, 1986.
- [136] Q.H. Deng and G.F Tang. Numerical visualization of mass and heat transport for conjugate natural convection/heat conduction by streamline and heatline. *International Journal of Heat and Mass Transfer*, 45:2373–2385, 2002.
- [137] H. Bansal and P.A. Nikrityuk. Arbitrary shaped ice particle melting under the influence of natural convection. *AIChE J.*, 63:3158–3176, 2017.
- [138] T.H. Ruvo, HM Toufik Ahmed Zisan, and S. Saha. Analysis of conjugate marangoni natural convection in a heating system with an open boundary flow. *International Communications in Heat and Mass Transfer*, 138:106402, 2022.
- [139] N.O. Moraga, L.A. Jauriat, and R.A. Lemus-Mondaca. Heat and mass transfer in conjugate food freezing/air natural convection. *International Journal of Refrigeration*, 35:880–889, 2012.
- [140] N.P. Gonzalez, D.R Rivera, and N.O. Moraga. Conjugate turbulent natural heat convection and solid food freezing modelling: Effects of position and number of pieces

- of salmon on the cooling rate. *Thermal Science and Engineering Progress*, 26:101101, 2021.
- [141] F. Dierich, S. Ananiev, and P.A. Nikrityuk. Simple immersed boundary matrix-cut-method for cartesian grids using fv and fd discretizations. *The Canadian Journal of Chemical Engineering*, 97:406–420, 2019.
- [142] Hemant Bansal, Sina Ghaemi, and Petr Nikrityuk. A scale-bridging model for ice particles melting in air. *Chemical Engineering Science*, 172:66–78, 2017.
- [143] Frank P Incropera, David P Dewitt, Theodore L Bergman, and Adrienne S Lavine. *Principles of Heat and Mass Transfer*. John Wiley & Sons, Inc., New York City, New York, 7th edition, 2013.
- [144] Wenxian Lin and S.W. Armfield. Natural convection cooling of rectangular and cylindrical containers. *International Journal of Heat and Fluid Flow*, 22:72–81, 2001.
- [145] Olga Shishkina. Momentum and heat transport scalings in laminar vertical convection. *Physical Review E*, 93(5):051102, 2016.
- [146] Olga Shishkina. Rayleigh-Bénard convection: The container shape matters. *Phys. Review Fluids*, page 090502, 2021.
- [147] C Elango, N Gunasekaran, and K Sampathkumar. Thermal models of solar still—A comprehensive review. *Renewable and Sustainable Energy Reviews*, 47:856–911, 2015.
- [148] Wolfgang Wagner and Hans-Joachim Kretzschmar. D2.1 Properties of Water and Steam. In *VDI Heat Atlas*, pages 153–300. Springer Science & Business Media, 2010.
- [149] Stuart W Churchill and Humbert HS Chu. Correlating equations for laminar and turbulent free convection from a vertical plate. *International journal of heat and mass transfer*, 18(11):1323–1329, 1975.
- [150] J. R. Lloyd and W. R. Moran. Natural Convection Adjacent to Horizontal Surface of Various Planforms. *Journal of Heat Transfer*, 96(4):443–447, 11 1974. ISSN 0022-1481.

- [151] ANSYS Fluent™, Release 22R2, - CFD Software | ANSYS, Inc., www.ansys.com/products/fluids/ansys-fluent. Accessed: 07/07/2023, 2022.
- [152] Franck Nicoud and Frédéric Ducros. Subgrid-scale stress modelling based on the square of the velocity gradient tensor. *Flow, turbulence and Combustion*, 62(3):183–200, 1999.
- [153] Joseph Smagorinsky. General circulation experiments with the primitive equations: I. the basic experiment. *Monthly weather review*, 91(3):99–164, 1963.
- [154] Stuart W Churchill and Humbert HS Chu. Correlating equations for laminar and turbulent free convection from a horizontal cylinder. *International journal of heat and mass transfer*, 18(9):1049–1053, 1975.
- [155] Henry Steven Fabian Ramos, Chinmay Baliga, Arvind Rajendran, and Petr A Nikri-tyuk. CFD-based model of adsorption columns: validation. *Chemical Engineering Science*, 2023.
- [156] ANSYS Fluent™, Release 22R2, - Ansys Fluent Customization Manual | ANSYS, Inc., www.ansys.com/. Accessed: June 2023, 2022.